Titre: Title:	Theoretical and Experimental Investigation of Thermo-Tunable MIS Coplanar Slow-Wave Structure Based on Vanadium Dioxide Phase Transition
Auteur: Author:	Jiudong Wu
Date:	2014
Type:	Mémoire ou thèse / Dissertation or Thesis
Référence: Citation:	Wu, J. (2014). Theoretical and Experimental Investigation of Thermo-Tunable MIS Coplanar Slow-Wave Structure Based on Vanadium Dioxide Phase Transition [Mémoire de maîtrise, École Polytechnique de Montréal]. PolyPublie. https://publications.polymtl.ca/1568/

URL de PolyPublie: PolyPublie URL:	https://publications.polymtl.ca/1568/
Directeurs de recherche: Advisors:	Ke Wu
Programme: Program:	génie électrique

UNIVERSITÉ DE MONTRÉAL

THEORETICAL AND EXPERIMENTAL INVESTIGATION OF THERMO-TUNABLE MIS COPLANAR SLOW-WAVE STRUCTURE BASED ON VANADIUM DIOXIDE PHASE TRANSITION

JIUDONG WU

DÉPARTEMENT DE GÉNIE ÉLECTRIQUE

ÉCOLE POLYTECHNIQUE DE MONTRÉAL

MÉMOIRE PRÉSENTÉ EN VUE DE L'OBTENTION

DU DIPLÔME DE MAÎTRISE ÈS SCIENCES APPLIQUÉES

(GÉNIE ÉLECTRIQUE)

OCTOBRE 2014

UNIVERSITÉ DE MONTRÉAL

ÉCOLE POLYTECHNIQUE DE MONTRÉAL

Ce mémoire intitulé:

THEORETICAL AND EXPERIMENTAL INVESTIGATION OF THERMO-TUNABLE MIS COPLANAR SLOW-WAVE STRUCTURE BASED ON VANADIUM DIOXIDE PHASE TRANSITION

Présenté par : WU Jiudong

en vue de l'obtention du diplôme de : Maîtrise ès sciences appliquées

a été dûment accepté par le jury d'examen constitué de :

M. Laurin Jean-Jacques, Ph. D., président

M. Wu Ke, Ph. D., membre et directeur de recherche

M. Tatu Serioja, Ph. D., membre

DEDICATION

To my family

ACKNOWLEDGEMENTS

First of all, I would like to give my sincere thanks to my supervisor, Professor Ke Wu, for his guidance, support and encouragement throughout my studies, which is indispensable for me to complete this thesis. I feel deeply grateful to my supervisor.

I would like to express my gratitude to the research members from INRS, Prof. Chaker, Nicolas Émond, Ali Dousset and Sébastien Delprat, for their continuous support, invaluable help throughout the work involved in this thesis.

I also appreciate all the personnels at the Poly-Grames Research Center, in particular M. Jules Gauthier, M. Traian Antonescu, M. Steve Dubé and M. David Dousset, for their skilled technical support in fabrication, measurement during my studies. My gratitude is extended to Mme. Ginette Desparois and Mme. Elena Pavlov for their administrative work and to M. Jean-Sébastien Décarie for his software support.

I am indebted to my friends for their help, in particular Wei Wang, Sulav Adhikari, Tao Jiang, Kuangda Wang, Pascal Burasa, Ladan Shabnam and Ya Deng, with whom I have had lots of helpful discussion. It is a great pleasure to study and work with them.

I would like to thank all the jury members for their time and efforts in reviewing my thesis and providing me valuable comments.

Finally, I would like to give my deep thanks to my parents and my sister. Thanks to my fiancée for her endless love and support in the last six years.

RÉSUMÉ

Actuellement, les circuits de taille réduite sont devenus de plus en plus importants dans les systèmes de communication en plus du faible coût potentiel et une grande portabilité. Afin de réduire la taille des composants passifs qui prennent généralement beaucoup d'espace dans les circuits, les structures MIS multicouches qui se composent de métal, de semi-conducteurs et des couches isolantes peuvent être utilisés.

Si la couche de semi-conducteurs dans les structures MIS est substituée par certains types de matériau intelligent dont la permittivité ou la conductivité peut être réglé par voie thermique, optique ou électrique, nous pouvons concevoir de nouveaux types de composants à micro-ondes variables, tels que la ligne de délai, les déphaseurs, ou les filtres accordables. Parmi tous les matériaux intelligents attrayants sont ceux qui montrent la transition de phase comme transition semiconducteur-métal (SMT). Dioxyde de vanadium (VO_2) a reçu une attention particulière en raison de sa faible dimension, faible température de transition et une haute résistance de changement de rapport. Basées sur les techniques et les discussions ci-dessus, les structures thermo-accordables coplanaires à ondes lentes à base de transition de phase sont présentées dans cette thèse.

Premièrement, un modèle de circuit équivalent unifié est proposé pour la structure coplanaire MIS à ondes lentes, y compris le MISCPW à couche mince, à couche mince de taille micrométrique et à couche épaisse de taille micrométrique. Le modèle proposé néglige certains phénomènes électromagnétiques sans importance basé sur la structure très simplifiée comme; ce modèle permet d'éviter la complexité de calcul ce qui concerne solutions à onde électromagnétique et de calculer le paramètre caractéristique de ces lignes de transmission avec une précision acceptable. En comparons avec les techniques de modélisation trouvée dans la littérature on remarque l'efficacité de la technique de modélisation que nous avons proposée.

Deuxièmes, la variation de la constante diélectrique de la couche mince VO2 déposée en fonction de la température a été extraite expérimentalement. Deux techniques de mesure différents sont utilisés pour la caractérisation de couche mince VO_2 à la phase semi-conducteur et la phase métallique, respectivement. La constante diélectrique mesurée est en accord avec les résultats

rapportés, qui vérifie la précision des résultats de mesure. La plage de fréquence mesurable des techniques utilisées de caractérisation et la théorie de milieu effectif sont également expliquées de manière explicite.

Finalement, les structures MIS coplanaires thermo-accordables à ondes lentes utilisant des transitions de phase à base de VO_2 sont présentées. Basé sur la technique de modélisation proposée, une analyse approfondie de l'influence des différents paramètres structurels et matériels sur les caractéristiques de la couche mince MISCPW est étudiée. Ceci est très utile pour la conception rapide et précise de MISCPW avec un facteur d'ondes lentes prédéfinie et atténuation réduite. Les structures MIS coplanaires thermo-accordables à ondes lentes montrent une augmentation spectaculaire du facteur d'ondes lentes lorsque la température augmente plus de la température de transition. Une augmentation continuée du facteur Q est également observée lorsque la température augmente.

ABSTRACT

Presently, miniaturized circuit has become more and more important in modern communication systems because of its potential low cost and high portability. In order to miniaturize the size of distributed passive components that usually take up much more circuit area than active circuits, multilayered MIS structures that consist of composite metal, insulator and semiconductor layers can be utilized.

If the semiconductor layer in the MIS structures is substituted by certain kinds of smart material whose permittivity and/or conductivity can be tuned thermally, optically or electrically, we can design new types of variable microwave components, such as delay line, phase shifter, or tunable filter. Among all the attractive smart materials are those showing phase transition like semiconductor-metal transition (SMT). Vanadium dioxide (VO_2) has recently received special attention because of its low dimension, low transition temperature and high resistance ratio change. Based on the techniques and discussions above, thermo-tunable MIS coplanar slow-wave structures based on vanadium dioxide phase transition are presented in this dissertation.

First of all, a unified equivalent circuit model is proposed for the MIS coplanar slow-wave structures including thin-film, micrometer-sized thin-film and micrometer-sized thick-film MISCPW. The proposed model neglects some unimportant electromagnetic phenomena and is based on a much simplified structure, thus avoiding the computational complexity of full-wave solutions. It is able to calculate the characteristic parameters of these transmission lines with quite acceptable accuracy. Comparisons with the state-of-the-art modeling techniques show the effectiveness of the proposed modeling technique.

Second, the broadband dielectric constant of the deposited VO_2 thin film versus temperature was experimentally extracted. Two different measurement techniques were used for the characterization of VO_2 thin film at semiconductor phase and metal phase, respectively. The measured dielectric constant is consistent with the reported results, which verifies the accuracy of the measurement results. The measurable frequency range of the characterization techniques used and the effective-medium theory are also explicitly explained.

Finally, the thermo-tunable MIS coplanar slow-wave structure based on VO_2 phase transition is presented. Based on the proposed modeling technique, an extensive analysis of the influence of various structural and material parameters on the characteristics of the thin-film MISCPW is investigated. This is very useful for the fast and accurate design of MISCPW with predefined slow-wave factor and minimized attenuation. The designed thermo-tunable MIS coplanar slow-wave structure shows a dramatic increase in slow-wave factor when the temperature increases over the transition temperature. A continuous increase in Q factor is also observed when the temperature increases.

TABLE OF CONTENTS

LIST OF TABLES

LIST OF FIGURES

LIST OF ACRONYMS AND ABBREVIATIONS

ADS	Advanced design system
CMM	Conformal mapping method
CPW	Coplanar waveguide
HFSS	High frequency structure simulator
MIS	Metal-insulator-semiconductor
MISCPW	Metal-insulator-semiconductor coplanar waveguide
MMIC	Monolithic microwave integrated circuit
RF	Radio frequency
S-CPW	Shielded-coplanar waveguide
SMT	Semiconductor-metal transition
SWF	Slow-wave factor
SWS	Slow-wave structures
PCT	Partial capacitance technique
P-U-L	Per-unit-length
Q-TEM	Quasi-transverse electromagnetic

INTRODUCTION

With the increasing demand for devices that have smaller physical size, miniaturized circuit has become more and more important in modern communication systems because of its potential low cost and high portability. The Moore's law predicts a significant miniaturization of electronic devices, which leads to the area occupied by active components that is considerably small compared to the area taken by passive monolithic components.

As the size of microwave passive components is inversely proportional to the effective dielectric constant, a substrate with sufficiently high dielectric constant can be used to miniaturize the circuit adequately at any operating frequency in order to reduce the size of distributed passive components. Unfortunately, most of relevant materials are not suitable because of their relatively low dielectric constant. The ferroelectric materials, however, are high in dielectric constant but they exhibit very high dielectric losses, which are very sensitive to temperature. Multilayered MIS (Metal-Insulator-Semiconductor) structures are shown to support slow-wave propagation by a proper selection of operating frequency, structural size and conductivity (doping level) of the semiconductor layer [1]. The support of slow-wave propagation can significantly increase the per-unit-length transverse capacitance, thus the effective permittivity of the circuit, which leads to a dramatic reduction in circuit size.

There were numerous works focusing on the analysis of MIS structures. An MIS slow-wave structure can be fabricated by depositing planar metallic patterns on the insulation layer formed or depleted on an appropriately doped semiconductor substrate. The MIS slow-wave structure can be in the form of an MIS microstrip line, MIS coplanar waveguide, MIS Schottky-contact microstrip and Schottky-contact coplanar waveguide [1]. The existence of a slow-wave mode was first predicted by Guckel [2] and verified by Hasegawa [3] in 1971. The slow-wave propagation is verified by a microstrip transmission line printed on Si-SiO_2 substrates. Compared with traditional microstrip line, this slow-wave transmission line shows a very high effective dielectric constant and also an extremely low characteristic impedance. In 1977, Hasegawa [4] proposed an MIS and Schottky coplanar slow-wave structure on GaAs substrates. The electric field is mostly confined inside the insulation layer or the depletion layer. In 1981, Seki [5] modeled a "cross-tie"

CPW line with a cascade of high/low characteristic impedance. The attenuation is reduced by one order of magnitude than that proposed in [4]. The attenuation is still higher than the corresponding CPW circuits because of its large width of strip and large gap between the strips. Recently, J. R. Long [6] has proposed a shielded passive coplanar interconnect S-CPW for silicon-based circuits. The mechanism of the proposed interconnects is the same as that in [5]. By increasing simultaneously the p-u-l inductance and the capacitance, the proposed S-CPW has a Q-factor around 22, which is over twice the Q-factor of a conventional 50 ohms coplanar waveguide from 15 to 40GHz.

The systems that exploit tunable devices potentially benefit from multi-functionality and performance enhancement. The tunability of such devices is normally realized by active electronic devices or RF-MEMS (micro-electro-mechanical systems). However, the performance of these active electronic devices are limited by non-linearity and high power consumption, while the MEMS devices have the problem of slow switching time and low reliability. Nowadays, lots of research work has been conducted on the basis of novel functional nano-materials which feature higher tunability, faster switching time and smaller size. The electrical property (resistivity, permittivity and permeability, e.g.) of those novel functional nano-materials can be controlled by external excitation (temperature variation, light illumination, applied voltage or field, etc.). Among all the attractive novel functional nano-materials are those showing phase transition like semiconductor-metal transition (SMT), vanadium dioxide (VO_2) [7] has received a special attention because of its low dimension, low transition temperature, high resistance ratio change and fast switching time [8].

It has been found that the SMT in VO_2 can be induced by applying a voltage larger than the threshold voltage across the VO_2 thin films even at room temperature [9-10]. When the carrier density is increased to a certain critical value, the SMT can be induced. This property makes the VO_2 material very promising for applications in electronic circuits. Up to now, lots of electrically-induced RF switches [9-10] are proposed, employing the ultra-fast SMT property of VO_2 thin films, but all the designs are based on a resistance change model without knowing the broadband dielectric property when designing the VO_2-based RF switches. Sharp changes of the electrical properties of VO_2 on the SMT are accompanied with abrupt changes in optical properties. The reflectivity change at the SMT can be as high as 92% (from 2 to 94%) at certain

wavelengths [11]. Remarkably in 2010, Minah Seo [12] proposed a terahertz nano-screen based on VO_2 phase transition. Hybridized with thin VO_2 films, the ultra-broadband terahertz nano-screen shows an extinction ratio of nearly 1×10^4 with 4 orders of magnitude change in resistivity associated with VO_2 phase transition. But the transmission at the VO_2 insulating state over the whole designed frequency range still needs to be improved. In 2008, Julien Givernaud et al [13] proposed a tunable band-stop filter design based on a fast, reversible SMT in VO_2 thin films. The operating frequency is from 11GHz to 13GHz. The filter consists of a transmission line coupled with four U-shaped resonators. The experimental results fit well with the simulation results while the insertion loss is also too high compared to the MEMS based tunable filter [14]. In 2009, Julien Givernaud et al [15] proposed a power limiting device based on the SMT in VO_2 thin films. First of all, a simple switch composed of a CPW loaded with the VO_2 patterns is presented. This power-induced switch works as a microwave "fuse" in the circuits over a broad band (from 100MHz to 40GHz), the threshold power can be tuned by external parameter like temperature or by DC voltage bias. A more complex passive power limiting device based on the former presented CPW line is proposed. The proposed power limiting device can limit the RF/MW incident power on a large band of frequency. In 2013, S. Vegesna [16] proposed a reconfigurable terahertz frequency selective structure based on VO_2 phase transition. A tunable FSS polarizer with extinction ratio of around 25 dB and a tunable bandpass FSS filter with 30 resonance frequency shifts are realized.

If the semiconductor layer in the MIS structures is substituted by the VO_2 thin film whose permittivity and conductivity can be tuned thermally, optically or electrically, we can design a new type of variable slow-wave structure. The objective of the dissertation is to design a thermally tunable MIS coplanar slow-wave structure based on the vanadium dioxide phase transition.

The thesis is organized in the following way:

Chapter 1 starts with the definition of slow-wave structure and the introduction of their different configurations. Special attentions are focused on the configurations of MIS slow-wave structures. The condition for the propagation of slow wave is explicitly given. In order to identify the three possible propagation modes inside the MIS structure, the resistivity-frequency domain chart is

used to clearly illustrate the three modes which come out from the three limiting cases of the substrate resistivity and frequency.

In chapter 2, typical configurations of the MIS coplanar slow-wave structures are first introduced, followed by the two different approaches used for the analysis of the MIS coplanar slow-wave structures. The loss mechanism is well documented and explicitly expressed in equations using the Q-TEM transmission line model. Possible ways of reducing the loss is also given. In the last section, the most important equations used for the extraction of characteristic parameters of the MIS coplanar lines from S parameters are provided.

In chapter 3, a unified equivalent circuit model is proposed for the MIS coplanar slow-wave structures. With the proposed equivalent circuit, an extensive analysis of the influence of various structural and material parameters on the characteristics of the thin-film MISCPW is investigated. This is very useful for a fast and accurate design of MISCPW with predefined slow-wave factor and minimized attenuation. This model avoids the computational complexity of the full electromagnetic solutions and calculates the characteristic parameter of these transmission lines with quite acceptable accuracy. With the proposed modeling techniques, the loss contribution from the three sources (conductor loss, transverse and longitudinal dielectric loss) can be easily calculated. Besides, we can gain much more insight into the mechanism and physics of the MIS slow-wave structures.

In chapter 4, the broadband dielectric constants of a deposited VO_2 thin film versus temperature are experimentally extracted. Based on the extracted dielectric constants, a thermally tunable MIS coplanar slow-wave structure is demonstrated based on the VO_2 phase transition. The characterization work is performed on the probe station. The measured dielectric constant is consistent with the reported results, which verifies the accuracy of the measurement results. Finally, the thermo-tunable MIS coplanar slow-wave structure based on VO_2 phase transition is presented. The designed thermo-tunable MIS coplanar slow-wave structure shows a dramatic increase in slow-wave factor when the temperature increases over transition temperature T_c. The attenuation is kept at a very low level, with the Q-factor is more than twice of that proposed in [4] over the whole frequency range. Obviously, the optimization of structural parameters can be performed to realize an optimum design.

The contributions of the research work presented in this dissertation are summarized in the last chapter. Even though only one design example of the thermally tunable MIS coplanar slow-wave structure is demonstrated, the modeling techniques can be extended for the rest of MIS coplanar slow-wave structures and the vanadium dioxide can be used for the design of a broad range of tunable microwave devices.

CHAPTER 1 METAL-INSULATOR-SEMICONDUCTOR (MIS) SLOW-WAVE STRUCTURES

The guided-wave properties of a waveguide are uniquely determined by the Maxwell Equations and the boundary conditions. Uniform rectangular and circular metallic waveguides exhibit phase velocity greater than the speed of light. These kinds of waveguides are usually categorized as fast-wave structures. The slow-wave structures are transmission lines in which the guide-waves travel with phase velocity less than the reference phase velocity. The reference phase velocity is usually determined by the maximum permittivity and permeability of all the composite medium layers.

1.1 Introduction to slow-wave structures

A slow-wave structure can be obtained with artificial guided-wave structures. The basic condition for the generation of slow-wave propagation inside a waveguide is that the guided-wave structure should provide separate storage of electric and magnetic energy in space either in axial or transverse directions [1].

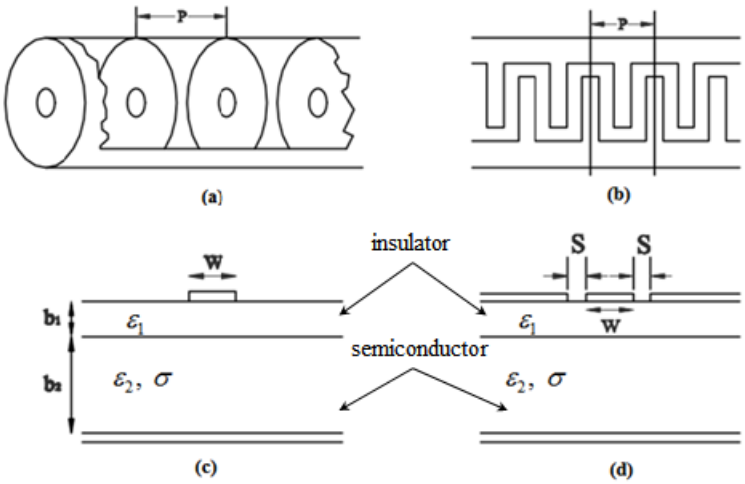

Figure 1.1: Two classes of slow-wave structure. (a) Periodic cavity-chain circular waveguide. (b) Periodic meander line. (c) MIS microstrip line. (d) MIS coplanar line.

Figure 1.1 illustrates two typical classes of slow-wave structures. In Figure 1.1(a) and Figure 1.1(b), two examples of classical periodic structures are shown. One is a cavity chain circular waveguide. The structure consists of a series of coupled resonant cavities. The smaller the center holes, the slower the phase velocity through the holes. This structure can be used to realize forward-wave travelling wave amplifiers or backward-wave oscillators. Figure 1.1(b) presents a periodic meander line. The meander line introduces a stopband in its transmission frequency response which can be regarded as low-pass behavior. Generally, the periodic slow-wave structure is formed by periodically loaded materials or periodic boundary conditions and can be analyzed by the Floquet's Theorem. The periodic slow-wave structure is very frequency-dispersive and relatively large in size, the periodic passband and stopband are a unique feature.

Table 1.1: Basic properties of slow-wave structures [1]

	Transmission loss	Slow-wave factor	Physical size	Maximum frequency	Frequency dispersion
Metallic periodic waveguide	Very low	Low to moderate	Very large	Extremely high	High
Planar periodic waveguide	Moderate to low	Low to moderate	Smaller to medium	High	Moderate to high
Thick-film MIS lines	Moderate to high	High	Very small	Low (several GHz)	Relatively high
Thin-film MIS lines	Relatively low	Moderate	Small	Medium (30GHz)	Low

In Figure 1.1(c) and Figure 1.1(d), two examples of uniform slow-wave structures are illustrated. The Metal-Insulator-Semiconductor (MIS) structure is a typical and best-known example of the uniform slow-wave structure. Uniform MIS slow-wave structure can be in the form of microstrip

in Figure 1.1(c) or coplanar waveguide in Figure 1-1(d). The uniform MIS slow-wave structure is fabricated by depositing the planar metallic patterns on the insulation layer formed or depleted on an appropriately doped semiconductor substrate. The doped semiconductor substrate, such as N^- doped silicon substrate ranges from a few micrometers (thin-film) to several hundred micrometers (thick-film). Compared to periodic structure, the frequency response is less dispersive and the size is much smaller. The reduction in phase velocity of MIS slow-wave structure is much greater than that of the periodic structure at the cost of a relatively higher transmission loss. The basic properties of the above slow-wave structures can be summarized in Table 1.1[1].

1.2 Metal-insulator-semiconductor slow-wave structures

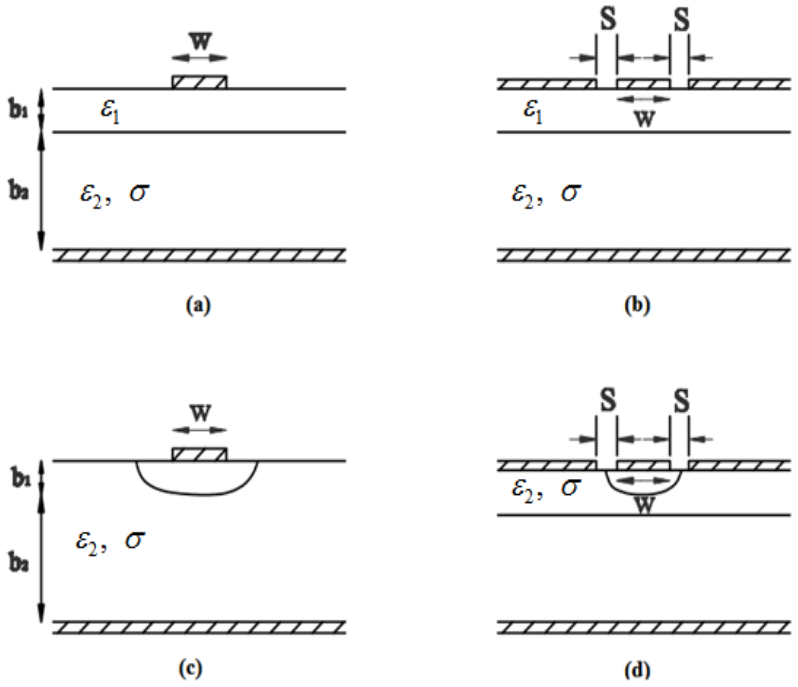

Figure 1.2: Typical configurations of MIS slow-wave structures. (a) MIS microstrip line. (b) MIS coplanar line. (c) Schottky-contact MIS microstrip line. (d) Schottky-contact MIS coplanar line.

The MIS slow-wave structure can be in the form of an MIS microstrip line (Figure 1.2(a)), MIS coplanar waveguide (Figure 1.2(b)), MIS Schottky-contact microstrip (Figure 1.2(c)) and Schottky-contact coplanar waveguide (Figure 1.2(d)).

Figure 1-2(a) presents an MIS microstrip deposited on semiconductor substrate separated by an insulator layer. The extremely thin insulation layer, silicon dioxide (SiO_2) for example, ranges from sub-micrometer to around two micrometers in thickness. The line width and the gap of the MIS coplanar strip and MIS CPW, as are shown in Figure 1-3(b), range from several hundred micrometers to several micrometers. The latter is usually named micrometer-sized MIS CPW which exhibits greatly improved Q factors. The Schottky-contact microstrip and Schottky-contact coplanar waveguide, as are shown in Figure 1-3(c) and Figure 1-3(d) respectively, are special cases of MIS slow-wave structures, where the insulation layer is formed by applying the negative biasing voltage across the metallic signal line to form a depletion layer. In this way, the thickness of insulation layer can be controlled and electrically tunable SWS can be formed.

The design objective of using the MIS structure is to maximize the slow-wave factor (SWF) while minimize the attenuation when a specific characteristic impedance requirement is satisfied. For MIS slow-wave structures, attenuation constant α, propagation constant β and characteristic impedance Z_c are usually calculated to fully describe the performance. The characteristic impedance Z_c is designed for impedance matching purposes. The attenuation is often given in dB/mm or Np/mm. Sometimes, a figure of merit Q, which is defined as a comprehensive quantity to evaluate the performance of both SWF and α. The slow wave factor and the quality factor can be defined as

$$SWF = \frac{\lambda_0}{\lambda_g} = \frac{v_0}{v_p} = \frac{\beta}{\beta_0} = \sqrt{\varepsilon_{eff}} \tag{1.1}$$

$$Q = \frac{\beta}{2\alpha} = \frac{\pi}{\alpha\lambda_g} \propto \left(\alpha\lambda_g\right)^{-1} \tag{1.2}$$

where λ_0 and λ_g are free-space wavelength and guided-wave wavelength, respectively. v_0 and v_p are the wave velocity in free-space and phase velocity in the waveguide. β_0 and β are free-space propagation constant and propagation constant in the waveguide. ε_{eff} is the effective permittivity

of the waveguide of a specifically designed geometry, thickness ratio of the insulation over semiconducting layer and conductivity of the semiconductor layer.

1.3 Conditions for the propagation of slow-wave in MIS structures

As mentioned in [1], the requirement for the propagation of slow-wave is the effective separation of electric and magnetic energy in space either in longitudinal or in transverse direction. The generation of slow-wave in periodic structure is normally in the longitudinal direction, whereas the generation of slow-wave in uniform structure (like MIS structure) is in the transverse direction.

The mechanism of supporting slow-wave propagation in MIS structure is that the magnetic field freely penetrates into the semiconductor layers since they are non-magnetic. The distribution of the magnetic field is almost the same as the case when no semiconductor layer exists, while the electric field is highly confined between the metallic patterns and the semiconductor layer inside the insulation layer. The effective spatial separation of electric and magnetic energy in transverse direction depends on geometry, thickness ratio and conductivity of the loaded semiconducting layer of the MIS transmission lines.

1.4 Three fundamental operating modes and resistivity-frequency chart

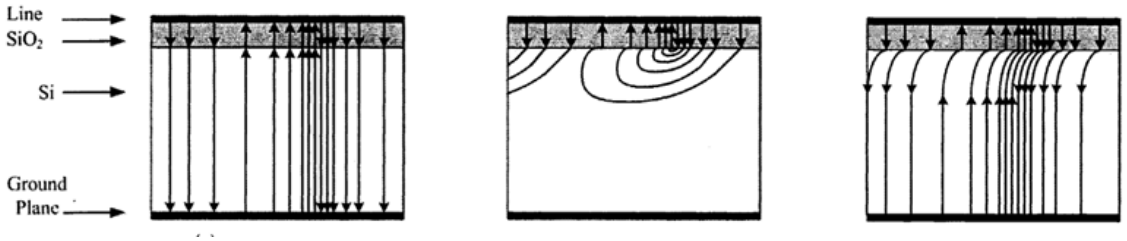

Figure 1.3: Electric field distribution of the three modes. (a) Dielectric Quasi-TEM mode. (b) Skin-effect mode. (c) Slow-wave mode [17].

It is well-known that the MIS structure can support the propagation of three modes. They are “dielectric quasi-TEM mode”, “skin-effect mode” and “slow-wave mode”. These three modes come out of three limiting cases of the substrate resistivity and frequency [3].

First of all, when the product of substrate resistivity and frequency is very large, or in its equivalent form $\omega\varepsilon_0\varepsilon_s \geq \sigma$ the electric and magnetic field lines can both freely penetrate the semiconductor substrate. The fundamental propagation mode is quasi-TEM mode as shown in Figure 1-3(a). In this case, the circuit can be regarded as a two-layered dielectric consisting of the insulation layer and the semiconductor layer. The quasi-TEM analysis is valid as long as the transverse dimensions of the structure are much smaller than a half wavelength of the highest frequency. The dielectric relaxation frequency f_d defines the boundary between the slow-wave mode and the dielectric quasi-TEM mode. This is the case when $\omega\varepsilon_0\varepsilon_s \geq \sigma$. The dielectric relaxation frequency f_d is defined as follows

$$f_d = \frac{\sigma_s}{2\pi\varepsilon_0\varepsilon_s} \tag{1.3}$$

Secondly, when the product of substrate conductivity and frequency is very large, or in its equivalent form $\omega\varepsilon_0\varepsilon_s \leq \sigma$, the electric and magnetic field can only penetrate a small amount of thickness named skin-depth. This corresponds to the skin-effect mode as shown in Figure 1-3(b). The semiconductor layer can be regarded as a good conductor and the MIS transmission line can be analyzed as interconnects on an imperfect ground plane. In this case, the line behaves very dispersive because of the skin-effect. If we define the characteristic frequency for skin-effect as the frequency when the penetration depth is equal to the semiconductor layer thickness, we have

$$f_s = \frac{1}{\pi\mu_0\sigma b_2^{\,2}} \tag{1.4}$$

Where $\sigma$is the conductivity of the semiconductor layer. $b_2$is the thickness of the semiconductor layer.

Between the above two limits there exists another form of propagation mode named “slow-wave mode” as is shown in Figure 1-3(c). In this case, the substrate conductivity is moderate and the frequency is not so high. The magnetic field can freely penetrate the semiconductor layer but the electric field is mainly concentrated inside the insulation layer just below the central signal line. Existence of the slow-wave mode was first predicted by Guckel [2] and verified by Hasegawa [3]. The characteristic frequency f_0 is used to define the region for the slow-wave propagation.

Table 1.2: Properties of fundamental modes of the MIS microstrip line

	Dielectric Quasi-TEM mode	Slow-wave mode	Skin-effect mode
frequency range	$f \geq 1.5 f_e$	$f \leq 0.3 f_0$	$f \geq 4 f_\delta, f \leq 10^{-2} f_{s\delta}$
ε_{eff}	$\varepsilon_0[(1/b)(b_1/\varepsilon_1 + b_2/\varepsilon_2)]^{-1}$	$\varepsilon_0\varepsilon_1(b_1+b_2)/b_1$	$\varepsilon_0\varepsilon_1(b_1+b_2)/b_1$
μ_{eff}	μ_0	μ_0	$\mu_0(b_1+0.5\cdot\delta)/(b_1+b_2)$
$f_e = \frac{1}{2\pi}\frac{\sigma_s}{\varepsilon_0\varepsilon_2}, \quad f_s = \frac{1}{2\pi}\frac{\sigma_s}{\varepsilon_0\varepsilon_1}\frac{b_1}{b_2}, \quad f_\delta = \frac{1}{2\pi}\frac{2}{\mu_0\sigma_s b_2^2}$			
$f_0 = \left[f_s^{-1} + \frac{2}{3} f_\delta^{-1} \right]^{-1}, \quad f_{s\delta} = f_s^2 / f_\delta$			

To specify the resistivity-frequency domain in which each mode propagates. The characteristic frequencies which are responsible for each of the three modes are summarized in Table 1.2 [3]. As is shown in Figure 1-2(a), if we assume an MIS microstrip structure with $\varepsilon_1 = 4, \varepsilon_2 = 12$, $b_1 = 1\mu m, b_2 = 200\mu m$, with the characteristic frequencies summarized above, we can plot the above resistivity-frequency domain chart as shown in Figure 1.4, from which we can clearly identify the region for each mode.

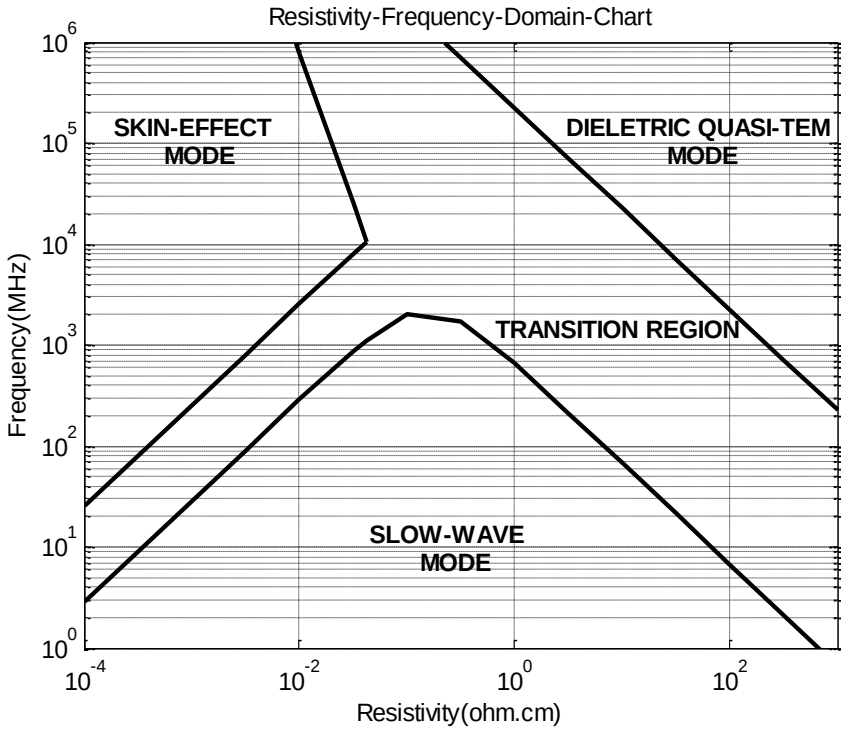

Figure 1.4: Resistivity-frequency domain chart of an MIS microstrip line.

CHAPTER 2 FUNDAMENTALS OF MIS COPLANAR SLOW-WAVE STRUCTURES

The coplanar waveguide (CPW) fabricated on a dielectric substrate was reported by C. P. Wen [18] in 1969. The CPW offers several advantages over the conventional microstrip line and stripline in the design of monolithic microwave integrated circuits (MMICs): First of all, the CPW is very easy to fabricate. All the signal line and the ground electrode are on the same plane, avoiding wraparound and via holes. Radiation loss and crosstalk can be greatly suppressed, but the conductor loss is high. Second, series and shunt passive and active components can be easily mounted on the circuits. Finally, the frequency dispersion in this circuit is very low and the CPW is wideband because it supports quasi-TEM modes.

2.1 Typical configuration of the MIS coplanar structure

As the coplanar MIS structures may support low-loss slow-wave propagation, they can be used to reduce the occupied circuit area and improve the quality factor. Lots of research work was focused on this topic in the last three decades [4-6].

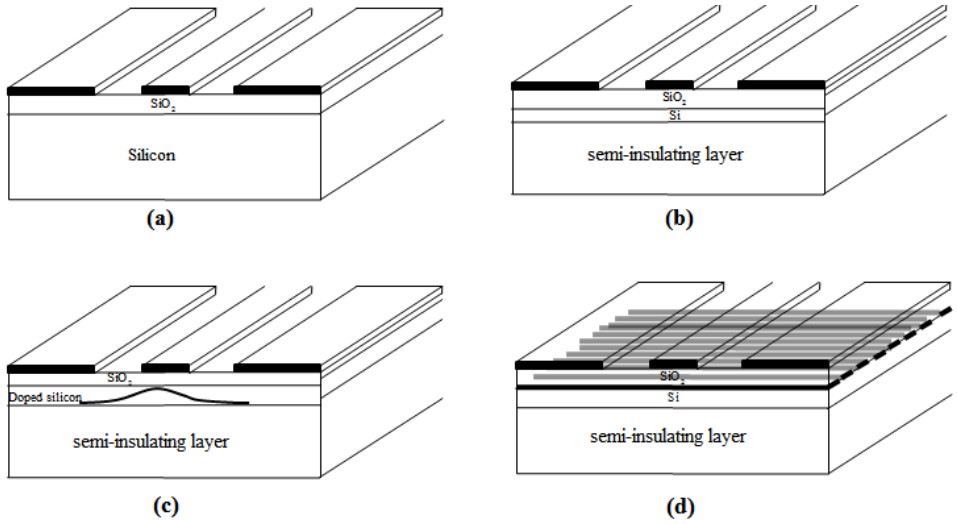

Figure 2.1: Four typical MIS coplanar structures. (a) Thick-film MISCPW. (b) Thin-film MISCPW. (c) Inhomogeneous doped MISCPW. (d) Shielded MISCPW.

The very basic configuration of coplanar MIS structure is shown in Figure 2.1(a). The thick-film coplanar MIS slow-wave structure, which can be fabricated by depositing planar metallic patterns on the insulation layer formed or depleted on an appropriately doped semiconductor substrate. The doped semiconductor substrate, such as GaAs ranges from a few micrometers (thin-film) to several hundred micrometers (thick-film). In order to reduce the loss, Kwon [19] proposed a micro-sized coplanar MIS slow-wave structure. The frequency of slow-wave operation successfully extends to 12.4GHz and the maximum attenuation at 12.4GHz is as low as 1.5dB/mm. An equivalent circuit model was also developed which is used to predict the performance of the proposed micro-sized slow-wave structure which agrees very well with the experimental results. Of course, the thick-film slow-wave structure in Figure 2.1(a) can be also realized in Schottcky-contact form, which is a special case of coplanar MIS structure. The insulation layer is formed by applying the negative biasing voltage across the metallic signal line relative to the metal ground. In this way, an electrically tunable coplanar slow-wave structure can be formed.

Shown in Figure 2.1(b) is the thin-film coplanar slow-wave structure, in which the semiconductor layer can be realized by a thin-layer of doped silicon in the order of sub-micrometer to a few micrometers. Typical attenuation of this structure is that α =0.2dB/mm and a slow-wave factor *SWF*=40 at 0.1GHz, but the attenuation increases to α =10dB/mm and a slow-wave factor decreases to *SWF*=10 at 4GHz [20]. This configuration will be employed in the following chapters to design the variable slow-wave structures. The loss mechanism is largely due to the tangential electric field component along the insulator and semiconductor interface. Most of the energy is stored near the edge of the slot area, so the micro-sized coplanar slow-wave structure which minimizes the line width and the slot space can greatly reduce the loss but at the cost of reduced slow wave factor because of the reduction in the area of the transverse p-u-l capacitance calculation.

Based on the same concept, K. Wu [21] studied the in-homogeneously doped low-loss coplanar slow-wave structure as shown in Figure 2.1(c). This structure is realized by Gaussian-like inhomogeneous doped semiconductor layer which reaches the maximum just below the central signal line. Without reducing the slot distance, this structure provides a reduced effective lossy

interface by reducing the lateral doped semiconductor. The analysis is carried out using the full-wave method-of-lines numerical method and the conductor loss is included and regarded as medium in the analysis. This approach has relaxed the dimensions of a micro-sized structure by a factor of 5 and reduces the loss even further.

In Figure 2.1(d), a "cross-tie" coplanar slow-wave structure is shown. The presented cross-tie CPW includes a "cross-tie" periodic metallic ground under the conventional CPW pattern. This structure is proposed by Seki in 1981[5] and is analyzed by using the Floquet's Theorem. The model is composed of a series of periodically alternating high impedance $Z_{c,h}$ and low impedance $Z_{c,l}$, so the electric energy and magnetic energy are longitudinally and periodically stored in the high impedance region A and low impedance region B, respectively. A simultaneously increase in inductance and capacitance give rise to the propagation of slow-wave. Besides, the alternating metallic ground breaks the longitudinal current inside the semiconductor substrate, so the loss is also reduced because of a partial isolation of electric field from the lossy semiconductor layer.

2.2 Analysis of coplanar slow-wave structures

Two approaches are usually used to characterize the MIS slow-wave structure. One is an approximate and quasi-static analytical model approach. This approach avoids a great computational complexity of the full electromagnetic field solutions and calculates the characteristic parameter of these transmission lines with a quite acceptable accuracy. The approximate model neglects some unimportant electromagnetic phenomena and is based on a much simplified structure. The quasi-static model supports quasi-TEM mode propagation and the transverse dimensions are much smaller than a half wavelength. It is also assumed that the analysis frequency $\omega \to 0$. It is well-known that the MIS structure can support three modes of propagation. They are "dielectric quasi-TEM mode", "slow-wave mode" and "skin-effect mode". Take the MIS coplanar structure which is shown in Figure 1-2(b) as an example, one approximate quasi-TEM model is shown in Figure 2.2.

2.2.1 Approximate and quasi-static model

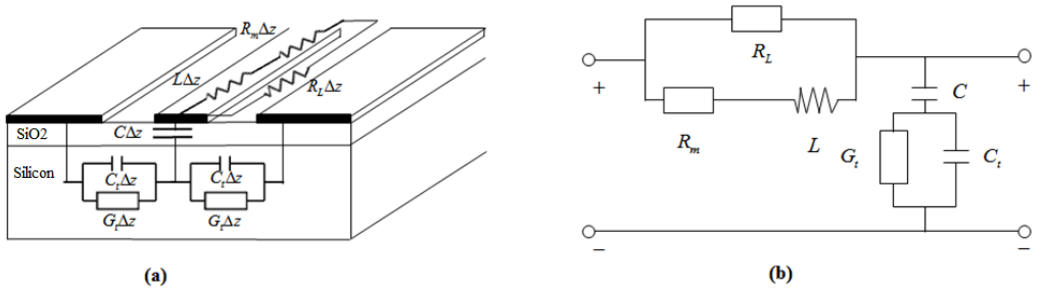

Figure 2.2: Approximate quasi-TEM model of the MIS coplanar structure. (a) physical configuration. (b) Equivalent circuit model.

Different approaches can be used to obtain series impedance Z(ω) and shunt admittance Y(ω). Both of them can be material, geometry and frequency dependent. The key point in obtaining series impedance Z(ω) is to model accurately the skin-effect related conductor loss and the fringing effect. The modeling of shunt admittance Y(ω) involves accurate modeling of the capacitance and the conductance of the multilayer.

As indicated by Kwon [19], the quasi-TEM analysis is based on the assumption that the penetration depth of the field is much less than the skin-depth of the semiconductor. If we conservatively suppose that the penetration depth $d = s + w/2$, then we have

$$f_s = \frac{1}{\pi\mu_0\sigma(s+0.5w)^2} \tag{2.1}$$

This frequency f_s defines the boundary between the skin-effect mode and the slow-wave mode.

The dielectric relaxation frequency f_d defines the boundary between the slow-wave mode and the dielectric quasi-TEM mode, we have

$$f_d = \frac{\sigma_s}{2\pi\varepsilon_0\varepsilon_s} \tag{2.2}$$

So we can conclude the frequency range for the propagation of those distinct three modes as follows:

1) Quasi-TEM mode: when the frequency range satisfies the condition of $f_s < f < f_d$, that is $\omega\varepsilon_0\varepsilon_s \geq \sigma$ in this case, the energy is mainly confined inside the semiconductor structure and the structure is very lossy.

2) Slow-wave mode: when the frequency range satisfies the condition of $f \leq f_d$, $f \leq f_s$. In this case, the electric energy is mainly confined inside insulation layer but the magnetic energy freely penetrate inside the semiconductor region as in the case of the conventional CPW structure with moderate substrate conductivity and frequency.

3) Skin-effect mode: when the frequency range satisfies the condition of $f_d < f < f_s$, that is $\omega\varepsilon_0\varepsilon_s \leq \sigma_s$ In this case, the line is usually very dispersive and the semiconductor layer behaves like a lossy imperfect conductor.

The characteristic frequency and the lumped component values of this MIS coplanar structure can be summarized in Table 2.1.

Table 2.1: Characteristic frequency and lumped component equations [19]

	f_d	f_s	R	G	L	C	R_L
MIS CPW	$\frac{\sigma_s}{2\pi\varepsilon_0\varepsilon_s}$	$\frac{1}{\pi\mu_0\sigma_s(s+\frac{1}{2}w)^2}$	$\frac{1}{\sigma\delta w}$	$2\sigma_s F$	$\frac{\mu_0}{4F}$	$\frac{\varepsilon_0\varepsilon_1 w}{b_1}K$	$\frac{1}{\sigma_s\delta w}$

Where in Table 2.1, F is the geometrical filling factor and the parameter K is the coefficient used to account for the fringing capacitance. If we assume an MIS coplanar structure as shown in Figure 2.1(a), with $\varepsilon_1 = 4, \varepsilon_2 = 12, b_1 = 0.53\mu m, b_2 = 530\mu m$, $w = 4.2\mu m$, space $s = 14\mu m$, with

the characteristic frequencies summarized above, we can have the following resistivity-frequency domain chart as shown in Figure 2.3.

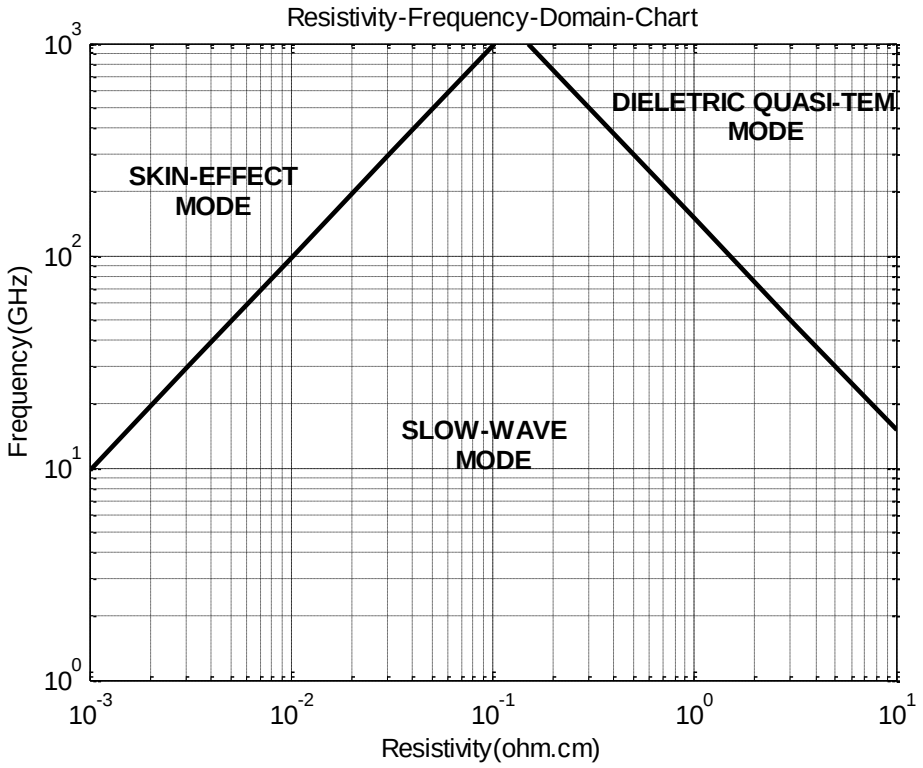

Figure 2.3: Resistivity-frequency domain chart of an MIS coplanar line.

2.2.2 Full-wave numerical analysis method

The second approach is the full-wave numerical analysis for the MIS structures. As the thickness ratio of the insulation layer and the semiconductor layer (or substrate layer) is quite large and the strip width is usually very small, so a 3D full-wave method such as finite element method with space-discretization is almost impossible to be used because it is very memory demanding. The method of lines [21], mode-matching method [22] and spectral-domain method [22] are usually considered to be the best choice to numerically predict the performance of the designed MIS structure. The semiconducting layer is treated as substrate with complex permittivity, and the complex propagation constant is obtained by searching a complex root of the determinant equation.

2.3 Loss mechanism and improvement of Q factor

To identify the sources of loss in the coplanar MIS structure, the unified transmission line model is first analyzed and discussed. Theoretical equations used to evaluate the loss (conductor and dielectric loss) represented by RLGC parameters are formulated.

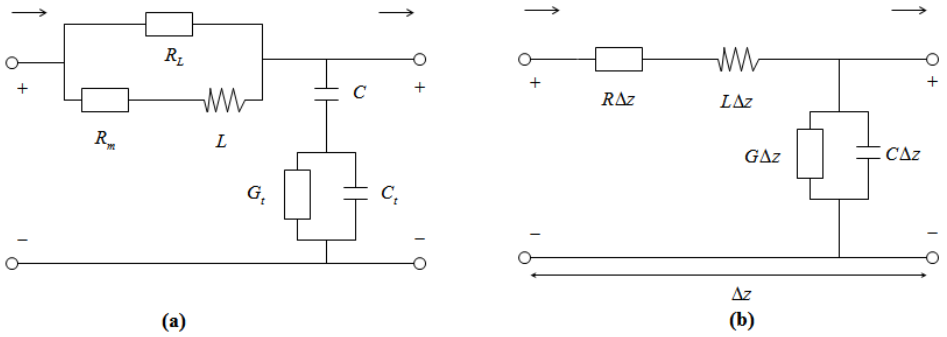

Figure 2.4: (a) Circuit model of the MIS CPW. (b) Equivalent lumped-element equivalent circuit.

$$\begin{cases} \dfrac{dV(z)}{dz} = -Z(\omega)I(z) \\ \dfrac{dI(z)}{dz} = -Y(\omega)V(z) \end{cases} \tag{2.3}$$

where if we assume $R_m \ll \omega L \ll R_{sub}$

$$\begin{cases} Z(\omega) = \dfrac{(R_m + j\omega L)R_{sub}}{R_m + j\omega L + R_{sub}} \approx \dfrac{j\omega L \cdot R_{sub}}{j\omega L + R_{sub}} \\ Y(\omega) = G + j\omega C_s \end{cases} \tag{2.4}$$

We can rewrite equations (2-3) in an uncoupled form

$$\frac{dV^2(z)}{dz^2} = \gamma^2 V(z) \tag{2.5}$$

$$\frac{dI^2(z)}{dz^2} = \gamma^2 I(z) \tag{2.6}$$

where

$$\gamma = \sqrt{ZY} = \sqrt{\frac{j\omega L \cdot R_{sub}}{j\omega L + R_{sub}}(j\omega C_s + G)} \approx j\omega\sqrt{LC_s}\left(1 - \frac{j\omega L}{2R_{sub}} + \frac{G}{2j\omega C_s} - \frac{G}{2j\omega C_s}\cdot\frac{j\omega L}{2R_{sub}}\right) \tag{2.7}$$

We assume $\omega L \ll R_{sub}$, $G \ll \omega C_s$ in the above equation, and then we have

$$\gamma \approx j\omega\sqrt{LC_s}\left(1 - \frac{j\omega L}{2R_{sub}} + \frac{G}{2j\omega C_s}\right) \tag{2.8}$$

$$\beta = \mathrm{Im}(\gamma) \approx j\omega\sqrt{LC_s} \tag{2.9}$$

$$\alpha = \mathrm{Re}(\gamma) \approx \frac{\omega^2 L}{2R_{sub}}\sqrt{LC_s} + \frac{G}{2}\sqrt{\frac{L}{C_s}} \tag{2.10}$$

For the coplanar MIS slow-wave structure, from equation (2.10), there are two sources of loss. One comes from the conductor loss as indicated in the first term of equation (2.10) and the other comes from the dielectric loss because of the semiconductor substrate used. The radiation loss can be ignored because of the CPW structure used.

The loss contribution of the above three types of losses is different for different kinds of MIS coplanar structure. The loss contribution versus frequency for the three types of MIS coplanar structures is summarized in Table 2.2.

To improve the quality factor which is defined as $Q = \beta/2\alpha \propto (\alpha\lambda_g)^{-1}$, we can increase the SWF while at the same time minimize the attenuation constant.

To increase the SWF, the basic idea is to increase the product of inductance and capacitance per unit length. The basic MIS structure shows an increased capacitance only and the separation of the electric energy and the magnetic energy is at the transverse direction. The shielded MIS coplanar structure can be used to separate storage of electric and magnetic energy in the longitudinal direction, so both the inductance and capacitance per unit length is increased.

To reduce the attenuation, that is to reduce the effective lossy interface between the slot edges, three approaches can be used. One is the cross-tie structure which periodically isolates the electric field from the semiconductor layer; the second method is to use the micro-sized structure

which reduces the slot width; the third approach is to have a Gaussian-like inhomogeneous doping profile inside the semiconductor substrate to reduce the effective lossy interface. The design of a coplanar MIS slow-wave structure is always a compromising work between characteristic impedance, attenuation and slow-wave factor.

Table 2.2: Loss contribution for three types of MIS coplanar structures

	Maximum operating f_{max}	Conductor loss	Transverse substrate loss	Longitudinal substrate loss
Thin-film MIS CPW	Several GHz	High to very low	Low to high	low
Thick-film μ-meter MIS CPW	Up to 30GHz	High to moderate	low	Low to moderate
Thin-film μ-meter MIS CPW	Up to 30GHz	High to moderate	low	Low

2.4 Extraction of characteristic parameters of MIS coplanar structures

2.4.1 Extraction of propagation constant and characteristic impedance

For a transmission line, the basic two characteristic parameters that can be used to characterize the performance are the complex propagation constant γ and the characteristic impedance Z_0. In this section, the algorithm for the extraction of the complex characteristic impedance, attenuation constant, slow-wave factor and quality factor is introduced.

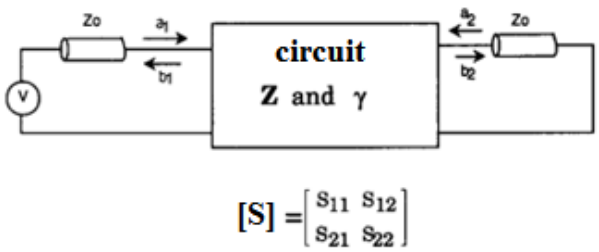

Figure 2.5: S matrix definition of 2-port network.

The transmission (or ABCD) matrix is defined for a two-port circuit where the total voltage and the total current are related in matrix form as [24]

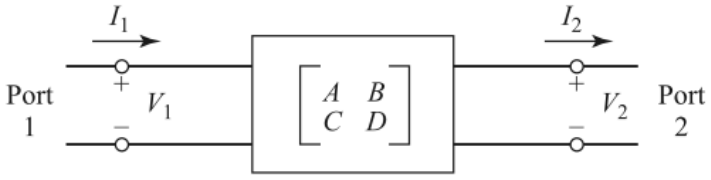

Figure 2.6: Transmission matrix definition of 2-port network.

$$\begin{bmatrix} V_1 \\ I_1 \end{bmatrix} = \begin{bmatrix} A & B \\ C & D \end{bmatrix} \begin{bmatrix} V_2 \\ I_2 \end{bmatrix} \tag{2.11}$$

For a transmission line with complex propagation constant γ and characteristic impedance Z_0, the transmission matrix can be calculated as such

$$\begin{bmatrix} A & B \\ C & D \end{bmatrix} = \begin{bmatrix} \cosh(\gamma l) & Z_0 \sinh(\gamma l) \\ Y_0 \sinh(\gamma l) & \cosh(\gamma l) \end{bmatrix} \tag{2.12}$$

From A= $\cosh(\gamma l)$, we have

$$\gamma l = \cosh^{-1}(A) = \ln(A \pm \sqrt{A^2 - 1}) \tag{2.13}$$

From S parameters to ABCD parameters conversion in Table 2.3, equation (2.13) is written as

$$e^{-\gamma l} = \left\{ \frac{1 - S_{11}^2 + S_{21}^2}{2S_{21}} \pm K \right\}^{-1} \tag{2.14}$$

Where

$$K = \left\{ \frac{(1 + S_{11}^2 - S_{21}^2)^2 - (2S_{11})^2}{(2S_{21})^2} \right\}^{1/2} \tag{2.15}$$

From

$$Z_0^2 = \frac{B}{C} \tag{2.16}$$

Table 2.3: S parameters to ABCD parameter conversion

ABCD	S
A	$\frac{(1+S_{11})(1-S_{22})+S_{12}S_{21}}{2S_{21}}$
B	$Z_0 \frac{(1+S_{11})(1+S_{22})-S_{12}S_{21}}{2S_{21}}$
C	$\frac{1}{Z_0} \frac{(1-S_{11})(1-S_{22})-S_{12}S_{21}}{2S_{21}}$
D	$\frac{(1-S_{11})(1+S_{22})+S_{12}S_{21}}{2S_{21}}$

We have

$$Z_0 = Z_r \sqrt{\frac{(1+S_{11})^2 - S_{21}^2}{(1-S_{11})^2 - S_{21}^2}} \tag{2.17}$$

where Z_r is defined as the reference characteristic impedance of the measurement equipment, which is 50 ohms in most of the cases.

As the phase is cyclically mapped from -180° to 180°, we have to convert to the real radian phase in extraction of the complex propagation constant γ and the characteristic impedance Z_0. The attenuation constant, slow-wave factor and quality factor can be expressed as

$$\begin{cases} \alpha(\mathrm{dB}/\lambda_g) = 8.686\,\mathrm{Re}(\gamma)\cdot\dfrac{2\pi}{\mathrm{Im}(\gamma)} = 54.55\dfrac{\mathrm{Re}(\gamma)}{\mathrm{Im}(\gamma)} \\ \alpha(\mathrm{dB}/\mathrm{mm}) = 8.686\,\mathrm{Re}(\gamma)\cdot 10^{-3} = 8.686\cdot 10^{-3}\,\mathrm{Re}(\gamma) \end{cases} \tag{2.18}$$

$$SWF = \frac{\beta}{\beta_0} = \frac{\mathrm{Im}(\gamma)}{\omega\sqrt{\varepsilon_0\mu_0}} \tag{2.19}$$

$$Q = \frac{\beta}{2\alpha} = \frac{\pi}{\alpha\lambda_g} \tag{2.20}$$

2.4.2 Extraction of effective RLGC parameters

In this section, the algorithm for the extraction of p-u-l RLGC parameters of the transmission line is presented.

From Figure 2.7, the series impedance and the shunt admittance can be expressed as

$$\begin{cases} Z = R + j\omega L \\ Y = G + j\omega C \end{cases} \tag{2.21}$$

From the Telegraph's equation, we know

$$\gamma = \sqrt{ZY} = \sqrt{(R + j\omega L)(G + j\omega C)} \tag{2.22}$$

$$Z_0 = \sqrt{\frac{Z}{Y}} = \sqrt{\frac{R + j\omega L}{G + j\omega C}} \tag{2.23}$$

From equations (2.36) and (2.37), we have

$$R = \mathrm{Re}\{\gamma Z_0\} \tag{2.24}$$

$$L = \mathrm{Im}\{\gamma Z_0\}/\omega \tag{2.25}$$

$$G = \mathrm{Re}\{\gamma / Z_0\} \tag{2.26}$$

$$C = \mathrm{Im}\{\gamma / Z_0\} / \omega \tag{2.27}$$

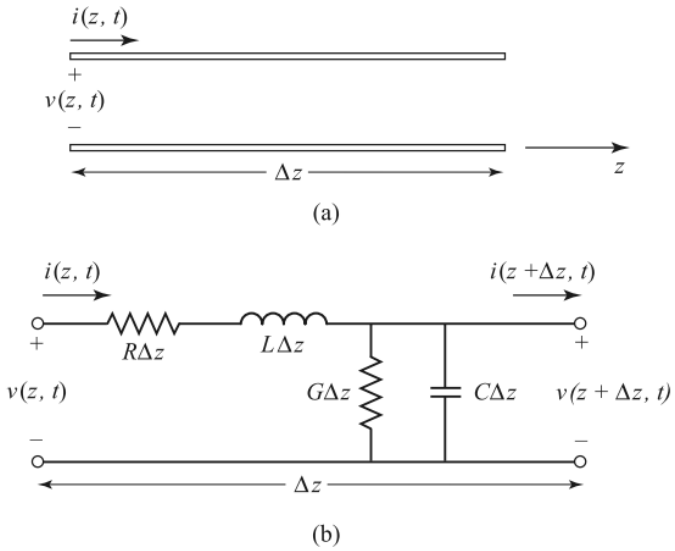

Figure 2.7: (a) Voltage and current definition for a transmission line of a unit length. (b) Lumped element equivalent for a transmission line of a unit length [23].

CHAPTER 3 MODELING OF MIS COPLANAR SLOW-WAVE STRUCTURE

3.1 Introduction

Two approaches are usually used to characterize the MIS coplanar slow-wave structure. One approach is the full-wave numerical analysis. The method of lines [21], Mode-matching method [22] and spectral-domain method [22] are usually employed to numerically predict the performance of the MIS coplanar structure. But some of the above numerical methods have assumed the perfect conductor and the conductor losses are systematically ignored. The other approach is the approximate and quasi-static analytical model approach [25-35]. As the MIS slow-wave structure can be sufficiently characterized by slow-wave factor, attenuation constant and characteristic impedance, some unimportant electromagnetic phenomena can be neglected and the characteristic parameter of these transmission lines can be calculated with quite acceptable accuracy based on the much simplified structure.

There are three difficulties in accurate modeling of the MIS coplanar slow-wave structures, they are: 1. Loss including conductor loss, transverse substrate loss, and longitudinal substrate loss caused by the magnetic coupling between the conductor and the lossy semiconductor layer; 2. Total capacitance of the insulation layer because of the fringing effect; 3. the internal inductance because of the skin-effect inside the conductors. As is shown in Table 3.1, the loss contribution from the above three types of loss is different for different MIS coplanar structures. That is why different equivalent circuits were proposed and reported but few of the models can be used for both the thick-film and thin-film MIS coplanar structures. The most important factors in modeling each MIS coplanar structure are summarized in Table 3.1.

This chapter is organized as follows:

1) First, a new unified model for both thick-film and thin-film MIS coplanar slow-wave structures is proposed.

2) A comparison of the proposed model and the other techniques in modeling the p-u-l lumped element of the coplanar circuit is then made, which is very useful in checking the accurateness of the proposed equivalent circuit model.

3) after that, the comparison is performed between the proposed model and the state-of-the-art modeling techniques in modeling both thick-film and thin-film MIS coplanar structures. The loss distribution in all of the three types of MIS coplanar structure is carefully calculated and discussed.

4) finally, an extensive analysis of the influence of conductivity of the semiconducting layer, the geometry and the thickness ratio on the performance of the MIS coplanar structure is made.

Table 3.1: Important factors in modeling different MIS coplanar structures

	Conductor loss	Transverse substrate loss	Longitudinal substrate loss	Internal inductance	Fringing capacitance
Thin-film MIS CPW		✓		✓	✓
Thin-film micrometer MIS CPW	✓			✓	✓
Thick-film micrometer MIS CPW	✓	✓	✓	✓	✓

3.2 A new unified analytical model for MIS coplanar slow-wave structure

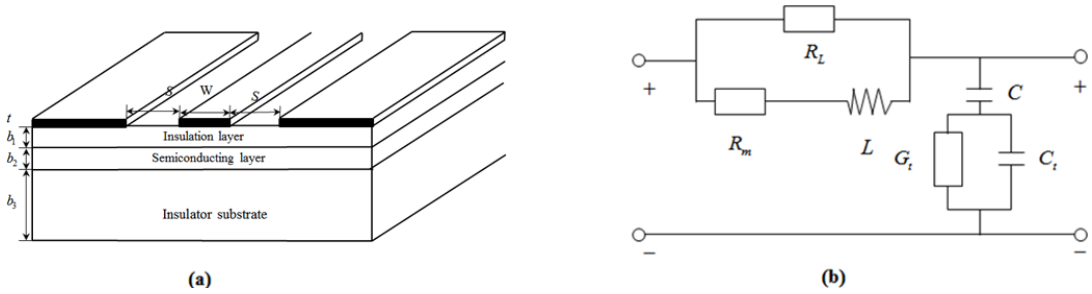

Figure 3.1: Approximate quasi-TEM model of the MIS coplanar structure. (a) Physical configuration. (b) Equivalent circuit model.

In this part, we will present a new unified analytical model for the MIS coplanar slow-wave structures. As shown in Figure 3.1(b), accurate modeling of the structure includes six lumped elements modeling. They are L and R_m of the conductor, R_L due to the magnetic coupling between the conductor and the semiconducting layer, C due to the electric energy confined inside the insulation layer, G_t and C_t due to the semiconducting layer.

3.2.1 Modeling of inductance and resistance of the conductor

As inductance L and resistance R_m are both very frequency-dependent, accurate modeling of L and R_m must take into account the finite conductivity and the finite thickness of the conductors. At low frequencies, the DC calculation can be used to approximate L and R_m; As frequency increases, the skin-effect occurs, when the skin-depth is less than one third of the conductor thickness t, the "Wheeler's Incremental Inductance Rule" [61] can be used to calculate L and R_m. Between these two regions, none of the above two approaches can be used. So smoothing terms are used to ensure the continuity of L and R_m and the first derivative of L and R_m at transition frequencies in the intermediate region. The expressions for the calculation of L and R_m are summarized in equation (3.3) and equation (3.6) [25]:

First, the external inductance $L_{e\infty}$ can be easily calculated as [26]

$$L_{e\infty} = \frac{1}{4c^2\varepsilon_0 F_0} = \frac{\mu_0}{4F_0} \tag{3.1}$$

Where the geometrical factor F_0 is

$$F_0 = \frac{K(k)}{K(k')} = \begin{cases} \dfrac{\pi}{\ln\left[\dfrac{2(1+\sqrt{k'})}{1-\sqrt{k'}}\right]}, & 0 \le k \le 0.707 \\ \dfrac{1}{\pi}\ln\left[\dfrac{2(1+\sqrt{k})}{1-\sqrt{k}}\right], & 0.707 \le k \le 1 \end{cases} \tag{3.2}$$

Where $k' = \sqrt{1-k^2}$, the total inductance can be calculated by equation (3.3) as the sum of the exte rnal inductance $L_{e\infty}$ and internal inductance L_i [25]

$$L_1 = L_{e\infty} + L_i = \begin{cases} L_{DC0} \cdot \left[1 + a_0^{(L)}(\dfrac{\omega}{\omega_{L0}})^2\right], & \omega \le \omega_{L0} \\ L_{e\infty} + L_{z1} \cdot (\dfrac{\omega}{\omega_{L1}})^{\nu_{z1}} \left[1 + a_1^{(L)}(\dfrac{\omega_{L0}}{\omega})^2 + a_2^{(L)}(\dfrac{\omega}{\omega_{L1}})^2\right], & \omega_{L0} \le \omega \le \omega_{L1} \\ L_{e\infty} + L_{z2} \cdot (\dfrac{\omega}{\omega_{L2}})^{\nu_{z2}} \left[1 + a_3^{(L)}(\dfrac{\omega_{L1}}{\omega})^2 + a_4^{(L)}(\dfrac{\omega}{\omega_{L2}})\right], & \omega_{L1} \le \omega \le \omega_{L2} \\ L_{e\infty} + \dfrac{F_L^{(c)} + F_L^{(g)}}{4F_0^2} \cdot \sqrt{\dfrac{\mu_0}{2\sigma\omega}} \left[1 + a_5^{(L)}(\dfrac{\omega_{L2}}{\omega})\right], & \omega \ge \omega_{L2} \end{cases} \tag{3.3}$$

with

$$\begin{aligned} L_{DC0} &= L_{DC}(\omega, \omega_g) \\ L_{z1} &= L_{DC}(\omega, \frac{3}{2}\omega) - \frac{\mu_0}{4} \cdot \frac{1}{F_1} \\ F_1 &= F_0 + \frac{K(k_2)}{K'(k_2)} - \frac{K(k_1)}{K'(k_1)} \\ L_{z2} &= \sqrt{\frac{\mu_0}{2\omega_{L2}\sigma}} \frac{F_L^{(c)} + F_L^{(g)}}{4F_0^2} \end{aligned} \tag{3.4}$$

And

$$\omega_{L0} = \frac{4}{\mu_0 \sigma t w_g}, \quad \omega_{L1} = \frac{4}{\mu_0 \sigma t w}, \quad \omega_{L2} = \frac{18}{\mu_0 \sigma t^2} \tag{3.5}$$

where ω_{L0} corresponds to the frequency at which the ground current distribution approximates the DC case. ω_{L1} denotes the frequency at which the center current distribution is uniform. ω_{L2} specifies the lower limit of the skin-effect frequency. The rest of the parameters can be referenced in [25]

Over low frequency range below ω_{L0}, the resistance can be approximated by the DC value. At frequencies when the skin-depth is less than one third of the conductor thickness, the "Wheeler's Incremental Inductance Rule" is used to calculate the R_m which is equal to ωL_i. The intermediate frequency range can be approximated by linear log-log frequency behaviour [25]. The total R_m can be calculated as the sum of the center conductor resistance $R_{c,m}$ and the ground conductor resistance $R_{c,m}$.

$$R_m = R_{c,m} + R_{g,m} \tag{3.6}$$

where

$$R_{c,m} = \begin{cases} R_{c0} \cdot \left[1 + a_1^{(c)} (\dfrac{\omega}{\omega_{c1}})^2\right], & \text{DC: } \omega \le \omega_{c1} \\ R_{c1} \cdot (\dfrac{\omega}{\omega_{c2}})^{\nu_c} \left[1 + a_2^{(c)} (\dfrac{\omega_{c1}}{\omega})^2 + a_3^{(c)} (\dfrac{\omega}{\omega_{c2}})^2\right], & \text{intermediate: } \omega_{c1} \le \omega \le \omega_{c2} \\ \dfrac{F_L^{(c)}}{4F_0^2} \cdot \sqrt{\dfrac{\omega\mu_0}{2\sigma}} \left[1 + a_4^{(c)} (\dfrac{\omega_{c2}}{\omega})^2\right], & \text{Skin-effect: } \omega \ge \omega_{c2} \end{cases} \tag{3.7}$$

$$R_{g,m} = \begin{cases} R_{g0} \cdot \left[1 + a_1^{(g)} (\dfrac{\omega}{\omega_{g1}})^2\right], & \text{DC: } \omega \le \omega_{g1} \\ R_{g1} \cdot (\dfrac{\omega}{\omega_{g2}})^{\nu_g} \left[1 + a_2^{(g)} (\dfrac{\omega_{g1}}{\omega})^2 + a_3^{(g)} (\dfrac{\omega}{\omega_{g2}})^2\right], & \text{intermediate: } \omega_{g1} \le \omega \le \omega_{g2} \\ \dfrac{F_L^{(g)}}{4F_0^2} \cdot \sqrt{\dfrac{\omega\mu_0}{2\sigma}} \left[1 + a_4^{(g)} (\dfrac{\omega_{g2}}{\omega})^2\right], & \text{skin-effect: } \omega \ge \omega_{g2} \end{cases} \tag{3.8}$$

With

$$R_{c0} = \frac{1}{\sigma w t}, \quad R_{c1} = \sqrt{\frac{\omega_{c2}\mu_0}{2\sigma}} \frac{F_L^{(c)}}{4F_0^2}, \quad R_{g0} = \frac{1}{2\sigma w_g t}, \quad R_{g1} = \sqrt{\frac{\omega_{g2}\mu_0}{2\sigma}} \frac{F_L^{(g)}}{4F_0^2} \tag{3.9}$$

$$\omega_{c1}=\sqrt{2}\frac{4}{\mu_0\sigma wt},\quad \omega_{c2}=\frac{8}{\mu_0\sigma}\left(\frac{w+t}{wt}\right)^2,\quad \omega_{g1}=\frac{2}{\mu_0\sigma w_g t},\quad \omega_{g2}=\frac{2}{\mu_0\sigma}\left(\frac{2w_g+t}{w_g t}\right)^2 \tag{3.10}$$

where ω_{ci} and ω_{gi} specifies the transition frequencies of the center and ground conductors

3.2.2 Modeling of magnetic coupling

The longitudinal substrate loss resistance R_L can be approximated by

$$R_L=\begin{cases}\rho_s\dfrac{1}{A}=\dfrac{1}{\sigma_s W b_2}, t\le\delta_s\\ \rho_s\dfrac{1}{W\delta_s}=\dfrac{1}{\sigma_s W\delta_s}, t\ge\delta_s\end{cases} \tag{3.11}$$

where ρ_s and σ_s are the resistivity and the conductivity of the semiconducting layer. W and b_2 are the center conductor width and the semiconducting layer thickness, respectively. δ_s is the skin-depth of the semiconducting layer.

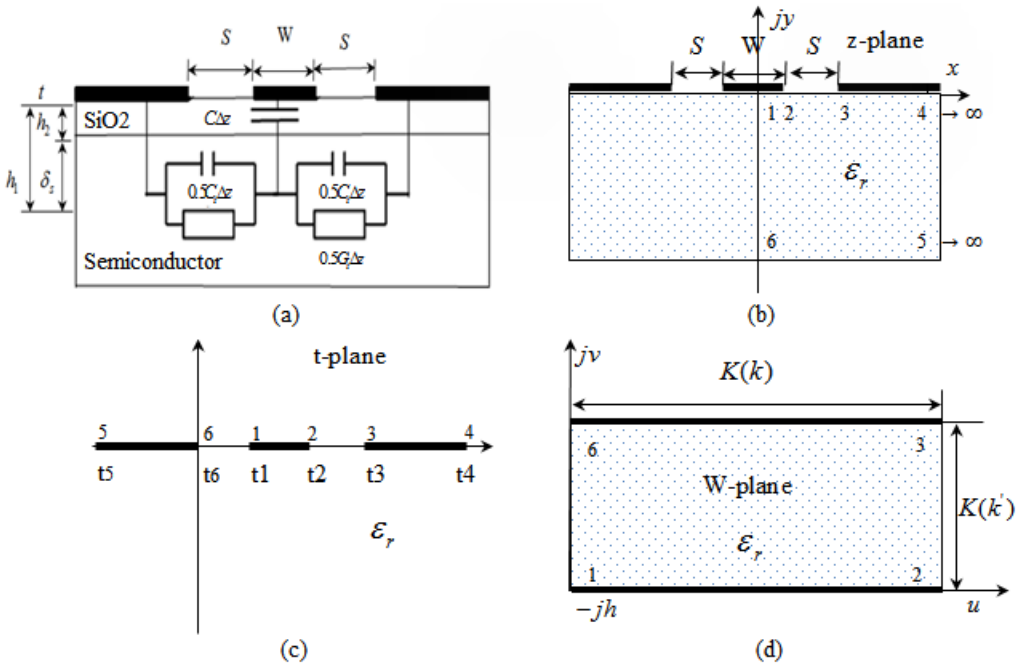

Figure 3.2: Conformal mapping for the calculation of filling factor. (a) Physical configuration. (b) z-plane. (c) t-plane. (d) W-plane.

3.2.3 Modeling of capacitance including fringing effect

To better account for the contribution to the total p-u-l capacitance due to the fringing effect of the conductor of finite thickness, the fringing effect because of the rectangular edge can be approximated as in the case of a circular cross-section conductor over a ground plane [27].

$$C_d = \varepsilon_0 \varepsilon_{ox} \left[\frac{s - 0.5t}{h_{ox}} + \frac{2\pi}{\ln(1 + \frac{2h_{ox}}{t} + \sqrt{\frac{2h_{ox}}{t}(\frac{2h_{ox}}{t} + 2))}} \right] \quad (S \geq 0.5t) \tag{3.12}$$

3.2.4 Modeling of capacitance and conductance of the semiconductor layer

In this part, unified frequency-dependent G_t and C_t are presented for both thick-film and thin-film MIS coplanar slow-wave structures. The transverse loss contribution can be calculated accurately by the geometrical filling factor F using the conformal mapping technique.

The conformal mapping technique will follow two steps: to begin with, the Schwartz-Christoffel transformation is used to map the right half of the MIS coplanar structure from the Z-plane to the T-plane

$$t = \cosh^2(\frac{\pi z}{2h}),\ z = x + jy \tag{3.13}$$

So the six points in the T-plane can be calculated as

$$\begin{aligned} &t_1 = \cosh^2(0) = 1, t_2 = \cosh^2(\frac{\pi s}{2h}) \\ &t_3 = \cosh^2(\frac{\pi(s+w)}{2h}) \\ &t_4 = t_5 = \infty, t_6 = 0 \end{aligned} \tag{3.14}$$

Then, the T-plane is transformed to the W-plane by the following Schwart-Christoffel transformation

$$W = u + jv = K(k) + K(k') = \int_1^t \frac{A \cdot dt}{\sqrt{t(t-t_1)(t-t_2)(t-t_3)}} \tag{3.15}$$

where $K(k)$ is the complete elliptical integral of the 1st kind, and

$$k = \frac{\sinh(\frac{\pi.W}{4h})}{\sinh\left\{\frac{\pi.(W/2+S)}{2h}\right\}}, \quad \lim_{h\to\infty} k = \frac{W}{W+2S} \tag{3.16}$$

If we define

$$k_2 = \frac{\sinh(\frac{\pi.W}{4(h_2)})}{\sinh\left\{\frac{\pi.(W/2+S)}{2(h_2)}\right\}} = \frac{\sinh(\frac{\pi.W}{4(b_1)})}{\sinh\left\{\frac{\pi.(W/2+S)}{2(b_1)}\right\}} \tag{3.17}$$

$$k_1 = \begin{cases} \dfrac{\sinh(\frac{\pi.W}{4(b_1+b_2)})}{\sinh\left\{\frac{\pi.(W/2+S)}{2(b_1+b_2)}\right\}}, & b_2 \le \delta_s \\ \dfrac{\sinh(\frac{\pi.W}{4(b_1+\delta_s)})}{\sinh\left\{\frac{\pi.(W/2+S)}{2(b_1+\delta_s)}\right\}}, & b_2 \ge \delta_s \end{cases} \tag{3.18}$$

So the geometrical filling factor of the semiconducting layer can be calculated as

$$F = F(h_1) - F(h_2) = \frac{K(k_1)}{K(k_1')} - \frac{K(k_2)}{K(k_2')} \tag{3.19}$$

Then we have

$$G_t = 2\sigma_s F, \; C_t = 2\varepsilon_0\varepsilon_r F \tag{3.20}$$

$$\begin{cases} Z(\omega) = (R_m + j\omega L) \| R_L = \dfrac{(R_m + j\omega L)\cdot R_L}{(R_m + j\omega L) + R_L} \\ Y(\omega) = \dfrac{1}{\dfrac{1}{j\omega C} + \dfrac{1}{G_t + j\omega C_t}} \end{cases} \tag{3.21}$$

From the Telegraph's equation, we know

$$\gamma(\omega) = \sqrt{Z(\omega)Y(\omega)},\ Z_0 = \sqrt{\frac{Z(\omega)}{Y(\omega)}} \tag{3.22}$$

3.3 Comparison of modeling techniques for longitudinal series impedance Z(ω)

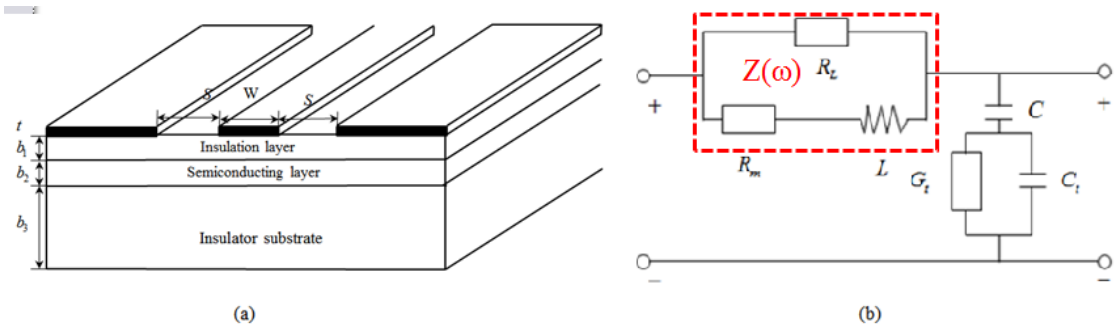

Figure 3.3: Illustration of MIS coplanar structure and its equivalent circuit. (a) Structural parameters. (b) Equivalent circuit.

In this part, the state-of-the art techniques for modeling the series impedance including conductor loss resistance, substrate loss resistance and total inductance are presented and compared. The structural parameters and the material parameters of Figure 3.3(a) are listed below [25]

$$w = 40\mu m, s = 5\mu m, w_g = 200\mu m, t = 1.5\mu m$$
$$b_1 = 0.53\mu m \qquad \sigma = 3\times 10^7 (S/m)$$
$$f = [f_{\min}, f_{\max}] = [0.01GHz, 100GHz]$$

3.3.1 Frequency-dependent series inductance *L*

As the inductance *L* is frequency dependent, accurate modeling of *L* must take into account the finite conductivity and the finite thickness of the conductors. The total inductance is the sum of external inductance $L_{e\infty}$ and internal inductance L_i because of the current inside the conductors.

1) In 1987, Kwon [19] calculated the external inductance only of the conductor which is assumed to be a zero thickness, the calculation procedures can be formulated as follows:

$$C = 4\varepsilon_0 \frac{K(k)}{K(k^{'})} \rightarrow L_2 = \frac{\mu_0}{4F_0} = \frac{1}{4\varepsilon_0 c^2} \frac{K(k^{'})}{K(k)} \tag{3.23}$$

where F_0 can be found in equation (3.2), $K(k)$ is the complete elliptical integral of the 1st kind.

2) To account for the fringing effect and the case of finite ground width, Veljko Milanović *et al* [28] approximated the inductance as the sum of the external inductance and the internal inductance because of the field penetration. First, the external inductance can be calculated by

$$L_{e\infty} = \frac{1}{c^2 C} = \frac{1}{4\varepsilon_0 c^2} \frac{1}{\left[K(k^{'})/K(k) + t/2w \right]} \tag{3.24}$$

where

$$C = 4\varepsilon_0 \left[\frac{K(k^{'})}{K(k)} + \frac{t}{2w} \right] \tag{3.25}$$

$$k = \frac{c}{b} \sqrt{\frac{b^2 - a^2}{c^2 - a^2}}; \; k^{'} = \sqrt{1 - k^2} \tag{3.26}$$

Where *b* and *a* are the ground distance and the center conductor width respectively. The second term in calculating *C* in (3.25) is a correction term used to account for the finite thickness effect. The ratio of the elliptical integral in the expression *C* can be calculated as such [29]

$$\frac{K(k)}{K(k^{'})} = \begin{cases} \dfrac{2\pi}{\ln\left(2\dfrac{\sqrt{1+k} + \sqrt[4]{4k}}{\sqrt{1+k} - \sqrt[4]{4k}}\right)}, 0 \le k \le 0.707 \\ \dfrac{1}{2\pi} \ln\left(2\dfrac{\sqrt{1+k} + \sqrt[4]{4k}}{\sqrt{1+k} - \sqrt[4]{4k}}\right), 0.707 \le k \le 1 \end{cases} \tag{3.27}$$

As frequency increases, the skin-depth decreases and becomes less than the metal thickness. To account for the internal impedance due to the field penetration, in 1989, Hai-Young Lee and T. Itoh [30] proposed a phenomenological loss equivalent method; the internal impedance is calculated by an equivalent single strip and can be expressed by

$$\begin{aligned} Z_{i,c} &= Z_s \cdot G \cdot \cot(\tau \cdot GA_c) \\ Z_{i,g} &= Z_s \cdot G \cdot \cot(\tau \cdot GA_g) \end{aligned} \tag{3.28}$$

where Z_s the surface resistance of the conductors, A_c and A_g are the cross-section area of the centre conductors and ground conductors, δ is the skin-depth of the conductors and all of them can be calculated by

$$Z_s = \sqrt{\frac{j\omega\mu}{\sigma}},\ \tau = \sqrt{j\omega\mu\sigma} \tag{3.29}$$

$$A_c = st; A_g = 0.5(c - s - 2w)t \tag{3.30}$$

The coefficient g is calculated as the derivative of the external inductance over the incremental recession of the conductor walls by a half the skin-depth $\delta/2$ as a function of frequency where

$$G = \frac{1}{\mu_0}\frac{\partial L_\delta}{\partial \delta} \tag{3.31}$$

So the internal inductance can be calculated by

$$L_i = \frac{\mathrm{Im}(Z_i)}{\omega} = \frac{\mathrm{Im}(Z_{i,c} + 0.5Z_{i,g})}{\omega} \tag{3.32}$$

and the total inductance can be summed as

$$L_3 = L_{e\infty} + L_i \tag{3.33}$$

The frequency dependence of the three total inductance calculations is shown and compared in Figure 3.4. When the frequency is close to DC range, all of the three calculations show a great difference but only L_1 is close to the DC case value which can be calculated by the magneto-static method. In the intermediate and skin-effect frequency range, both L_1 and L_3 show $1/\sqrt{f}$ frequency dependence. While L_2 remains almost constant in the whole frequency range, this is

due to the fact that L_2 only calculates the $L_{e\infty}$ term. For the high frequency limit, both L_1 and L_3 converge to the external inductance $L_{e\infty}$ of a perfect conductor. The HFSS simulation results for inductance L is calculated using the equation (2.25).

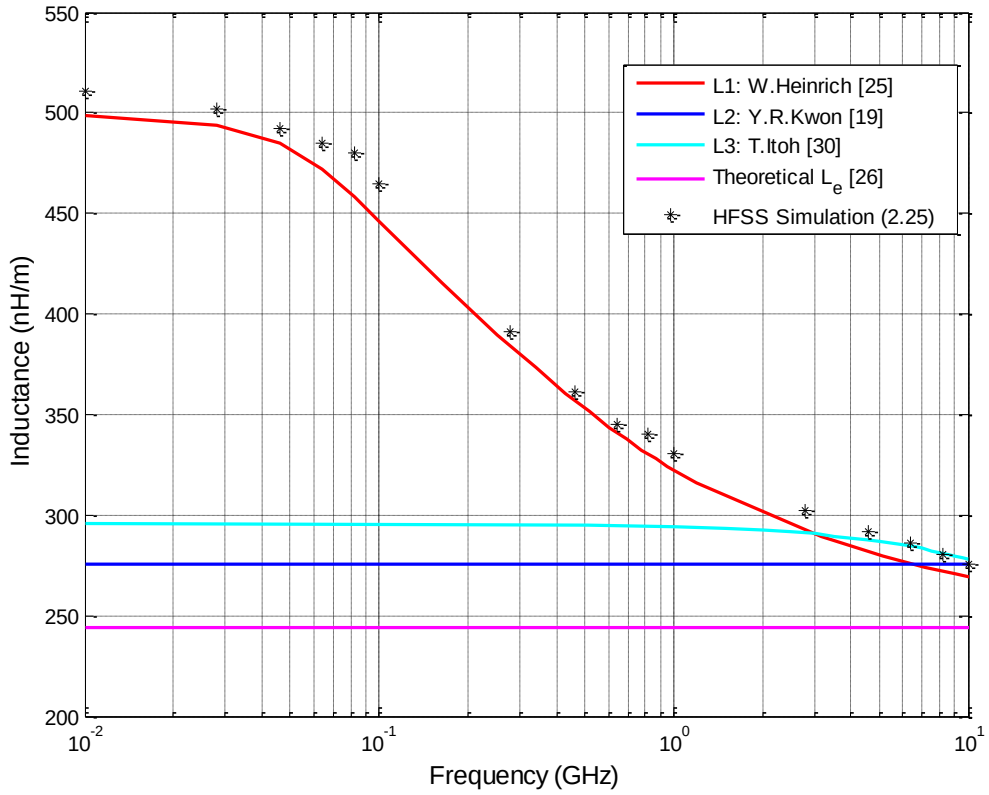

Figure 3.4: Comparison of total inductance calculations of the CPW line in Fig 3.3. w=40μm, s=5μm, t=1.5μm, b_1=0.53μm, b_2=530μm, σ=3× 10^7(S/m).

3.3.2 Frequency-dependent conductor loss resistance R_m

1) In 1987, Kwon [19] approximated the conductor loss resistance with such a simple expressions as

$$R_2 = \begin{cases} \rho\dfrac{1}{A} = \dfrac{1}{\sigma st}, t \le \delta_c \\ \rho\dfrac{1}{s\delta_c} = \dfrac{1}{\sigma s\delta_c}, t \ge \delta_c \end{cases} \tag{3.34}$$

where ρ and σ are the resistivity and the conductivity of the conductor. t is the conductor thickness. δ_c is the skin-depth of the conductor at certain frequency point. The skin-depth is related to the conductivity and the frequency as follows

$$\delta_c = \sqrt{\frac{2}{\omega\mu_0\sigma}} \tag{3.35}$$

2) As proposed by T. Itoh [30], the p-u-l transverse resistance R_m can be calculated by the phenomenological loss equivalent method as

$$R_3 = \mathrm{Re}(Z_i) = \mathrm{Re}(Z_{i,c} + 0.5Z_{i,g}) \tag{3.36}$$

where the equations for the calculation of $Z_{i,c}$ and $Z_{i,g}$ can be found in equations (3.28)

3) To account for the longitudinal conductive loss because of the current on the conductor, Jin-Su Ko [31] used the "Wheeler's incremental inductance rule" to model the conductive loss based on the quasi-static assumptions and when all the side-walls are recessed by $\delta_c/2$. As the "Wheeler's incremental inductance rule" is valid only when the thickness of the conductor is larger than 4 times of the skin-depth, this expression is only applicable to conductors with a large thickness. The expression used to approximate the resistance of the CPW structure is as follows

$$R_4 = 5.62\times10^{-5} R_s \varepsilon_r \cdot 2Z_c^2 \frac{F^2 P}{\pi w}\cdot\left(1+\frac{s}{w}\right) \cdot \frac{1+\dfrac{1.25}{\pi}\left(\ln\dfrac{4\pi s}{t}+\dfrac{t}{s}\right)}{\left[2+\dfrac{s}{w}-\dfrac{1.25t}{\pi w}\left(1+\ln\dfrac{4\pi s}{t}\right)\right]^2} \tag{3.37}$$

Where

$$Z_c = \sqrt{\frac{L}{C_d}},\ \varepsilon_{re} = \frac{\varepsilon_r+1}{2},\ R_s = \frac{1}{\sigma\delta_c(1-e^{-t/\delta_c})} \tag{3.36}$$

$$P = \begin{cases} \dfrac{k}{(1-\sqrt{1-k^2})(1-k^2)^{0.75}} & ,0 < k \le 0.707 \\ \dfrac{1}{\sqrt{k}(1-k)F^2} & ,0.707 \le k < 1 \end{cases} \tag{3.39}$$

As is shown in Figure 3.5, when frequency is close to DC range, all of R_1, R_2 and R_3 calculations show almost the same results. This is because the calculation of R_4 is for very thick metal when the thickness is thicker than 4 times of the skin-depth. In the intermediate and skin-effect frequency range, all of R_1, R_2 and R_3 calculations show $\sqrt{f}$ frequency dependence. But the resistance calculated by R_1 is much larger than the rest in this frequency range. In the skin-effect frequency limit, both R_1 and R_3 converge to the same resistance value calculated by full-wave HFSS simulation results.

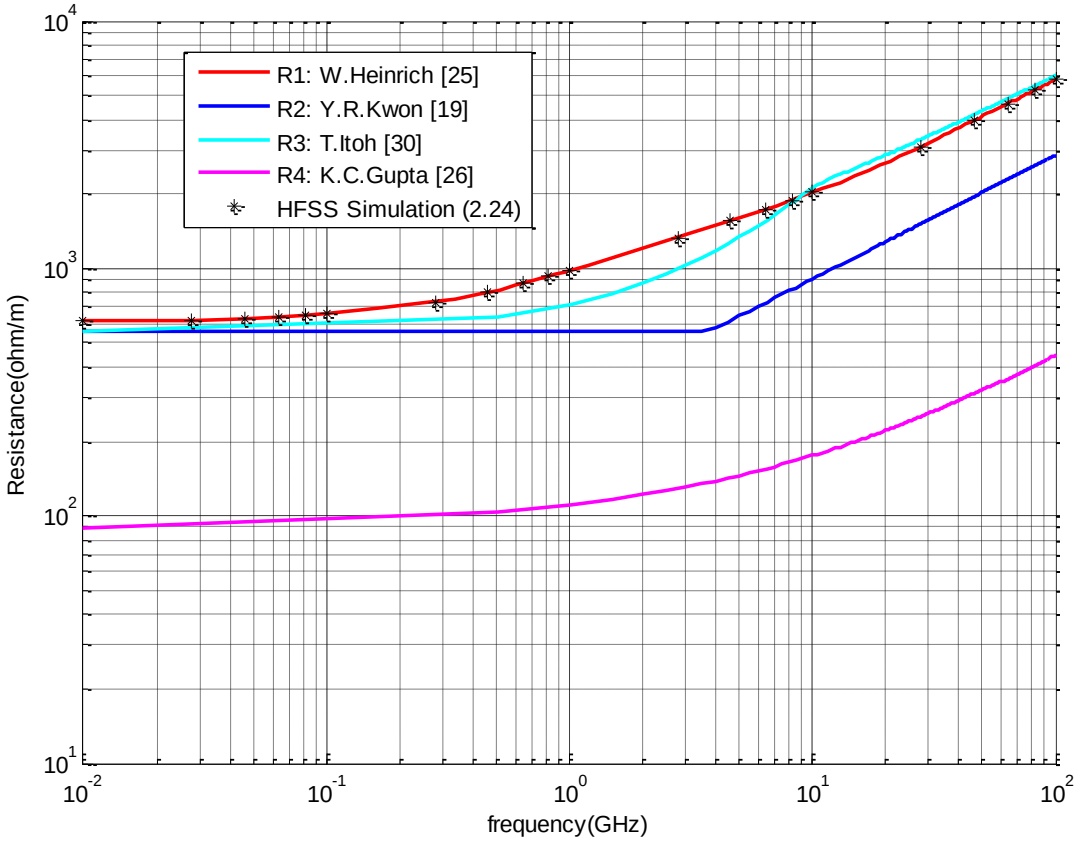

Figure 3.5: Comparison of conductor resistance calculations of the CPW line in Fig 3.3. w=40μm, s=5μm, t=1.5μm, b_1=0.53μm, b_2=530μm, σ=3× 10^7(S/m).

3.3.3 Frequency-dependent magnetic coupling

The extent to which the substrate affects the total performance of the MIS coplanar slow-wave structure depends greatly on the conductivity of the semiconductor layer, the frequency and the

geometry of the coplanar structure (line width, gap and distance between the conductor to the substrate layer). The magnetic coupling between the conductors and the substrate induces loss which is modeled by the resistance R_L(ohm/m). As the longitudinal current flows in addition to the current on the conductor; the resistance R_L is modeled in parallel with the series impedance.

Kwon [19] approximated the resistance R_L as

$$R_L = \rho_s \frac{1}{S\delta_s} = \frac{1}{\sigma_s S\delta_s} \tag{3.40}$$

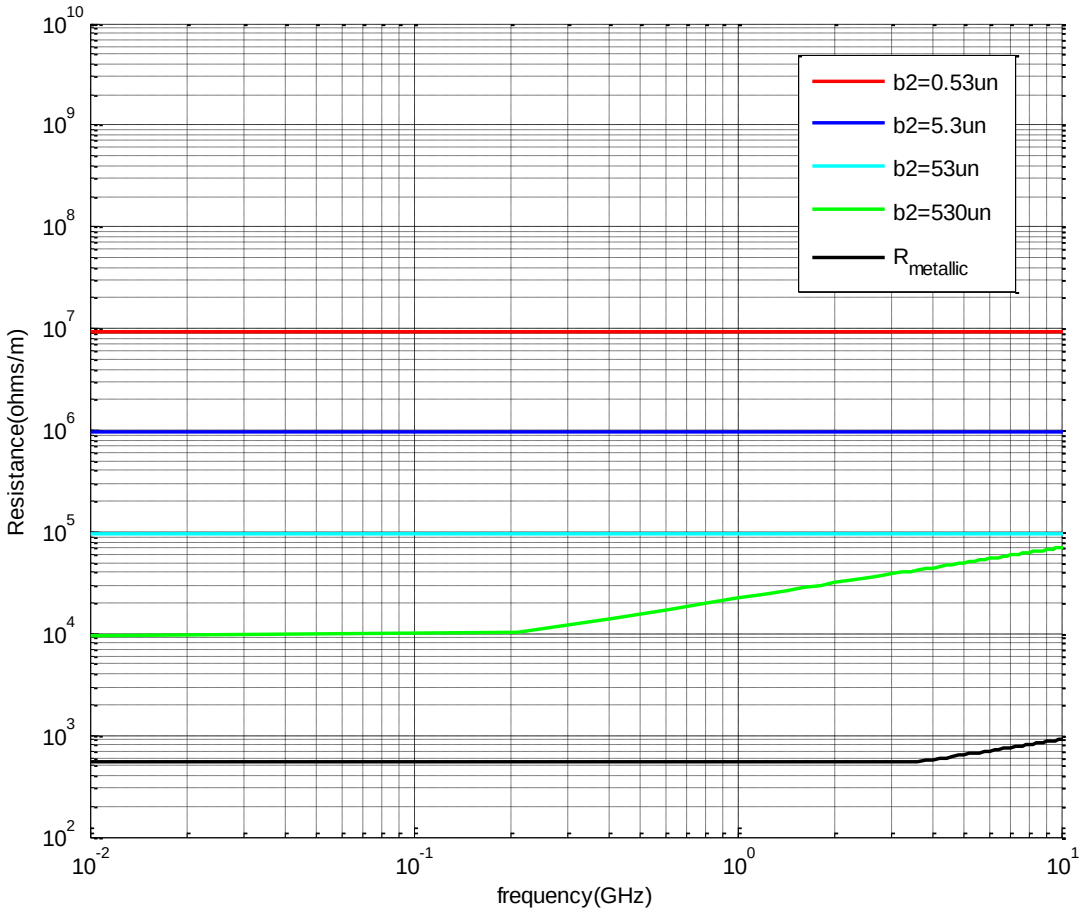

Figure 3.6: Comparison of longitudinal substrate loss resistance in Fig 3.3. w=40μm, s=5μm, t=1.5μm, b_1=0.53μm, σ_s=5000(S/m), σ=3× 10^7(S/m).

This expression only considers the case of a thick-film MIS coplanar structure. For the thin-film case, we shall substitute the skin-depth δ_s by the semiconducting layer thickness b_2. As can be observed in Figure 3.6, the thicker the semiconductor layer is, the smaller the longitudinal substrate resistance becomes. So the longitudinal substrate resistance modeled by R_L is very important for the thick-film micrometer- sized MIS coplanar structures.

3.4 Comparison of modeling techniques for transverse shunt admittance Y(ω)

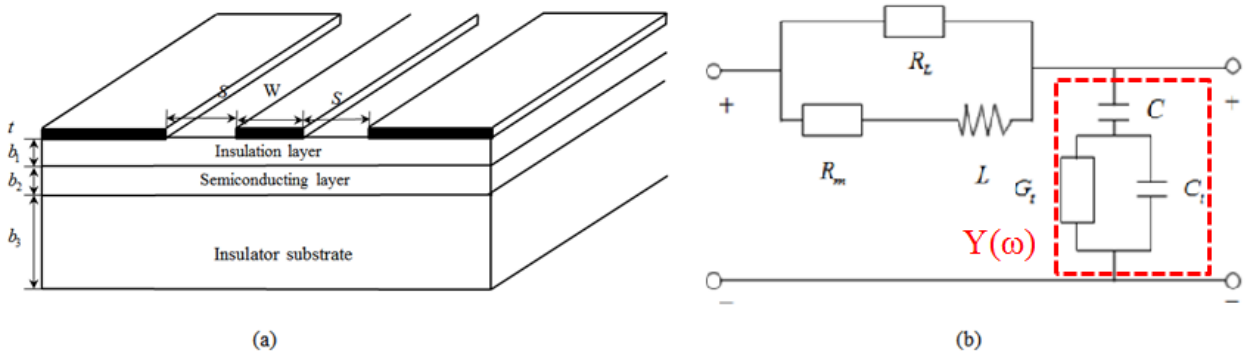

Figure 3.7: Illustration of the MIS coplanar structure and the equivalent circuit. (a) Structural parameters. (b) Equivalent circuit.

In this part, the state-of-the art techniques for modeling the shunt admittance including transverse substrate loss resistance (or conductance), insulation layer capacitance and semiconducting layer capacitance are presented and compared, the structural parameters and the material parameters of Figure 3.7(a) are listed below [25]

3.4.1 Shunt capacitance with fringing effect

1) Kwon [19] modeled the p-u-l capacitance as K=1.1

$$C_1 = \varepsilon_0 \varepsilon_{ox} \frac{s}{h_{ox}} K \tag{3.41}$$

where d is the insulation thickness and coefficient K is used to include the fringing field effect and K>1.

2) The electric energy storage associated with the transverse electric field can be modeled as capacitance in the equivalent circuit. The electric energy is mainly confined inside the insulation layer. To better account for the contribution to the total p-u-l capacitance due to the fringing effect of the conductor of finite thickness, T. N. Trick [27] approximated the fringing effect because of the rectangular edge as in the case of a circular cross-section conductor over an ground plane, the capacitance including fringing effect can be calculated as

$$C_2 = \varepsilon_0 \varepsilon_{ox} \left[\frac{s - 0.5t}{h_{ox}} + \frac{2\pi}{\ln(1 + \frac{2h_{ox}}{t} + \sqrt{\frac{2h_{ox}}{t}(\frac{2h_{ox}}{t} + 2))}} \right] f_c \qquad (3.42)$$

$$(S \geq 0.5t)$$

where f_c is used as a correction factor to account for the trapezoidal cross-section of the conductor, here as the geometry of the conductor is rectangular, f_c is equal to 1.

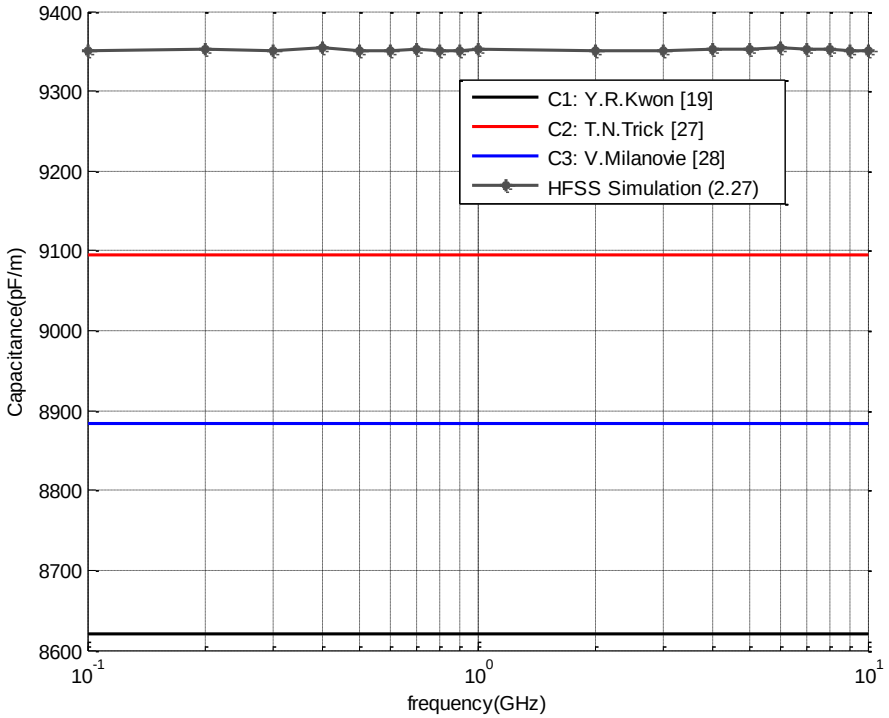

Figure 3.8: Comparison of capacitance calculations of the insulation layer of CPW line in Fig 3.3. w=40μm, s=5μm, t=1.5μm, b_1=0.53μm, b_2=530μm, σ_s=5000(S/m), σ=3× 10^7(S/m).

3) In 1998, Veljko Milanovi é *et al* [28] proposed an approximate expression which is fitted from the commercial two-dimensional finite element simulation of different center conductor width *s*, the expression is given by

$$C_3 = \varepsilon_0 \varepsilon_{ox} \frac{s}{h_{ox}} + 1.5\varepsilon_0 \varepsilon_{ox} (\frac{s}{h_{ox}})^{0.1} \tag{3.43}$$

As shown in Figure 3.8, the above three capacitance calculations show a frequency-independent response. The calculated values are only 10% in difference, the calculation of C3 involves a constant K to approximate the fringing effect but there are no criteria to guide the selection of the constant K. Comparatively, the equation (3.42) approximates the capacitance much more accurately.

3.4.2 Shunt resistance and capacitance of the semiconducting layer

1) The loss associated with the transverse current is modeled as resistance R_s. For the semiconductor layer, $\sigma_s \gg \varepsilon_0 \varepsilon_s \omega$ is normally satisfied. The derivation of the above equation is analogous to the case of deriving the inverse transverse capacitance of CPW. so the p-u-l resistance R_s is resistive and can be approximated by Kwon [19] as

$$G_2 = 2\sigma_s F, C_2 = 2\varepsilon_0 \varepsilon_r F \tag{3.44}$$

2) In 1998, Veljko Milanovi é [28] calculated conductance G_s based on the conformal mapping analysis of a multi-layered structure. The p-u-l resistance G_s is approximated as

$$G_3 = 2\sigma_s F_s, C_3 = 2\varepsilon_0 \varepsilon_s F_s \tag{3.45}$$

Where $F_s = F(\infty) - F(h_{ox})$, F is the same as the one calculated above in equation (3.2), $F(h_{ox})$ can be calculated by

$$F(h) = \frac{K(k(h)')}{K(k(h))}, k(h_{ox}) = \frac{c(h)}{b(h)} \sqrt{\frac{b^2(h) - a^2(h)}{c^2(h) - a^2(h)}} \tag{3.46}$$

where $a(h), b(h), c(h)$ are the transformed dimensions. The transformation is defined as

$$x(h) = \sinh(\frac{\pi \cdot x}{2h}),\ x = a, b, c \tag{3.47}$$

where a, b, c is the center conductor width, inner ground-to-ground width and outer ground-to-ground width.

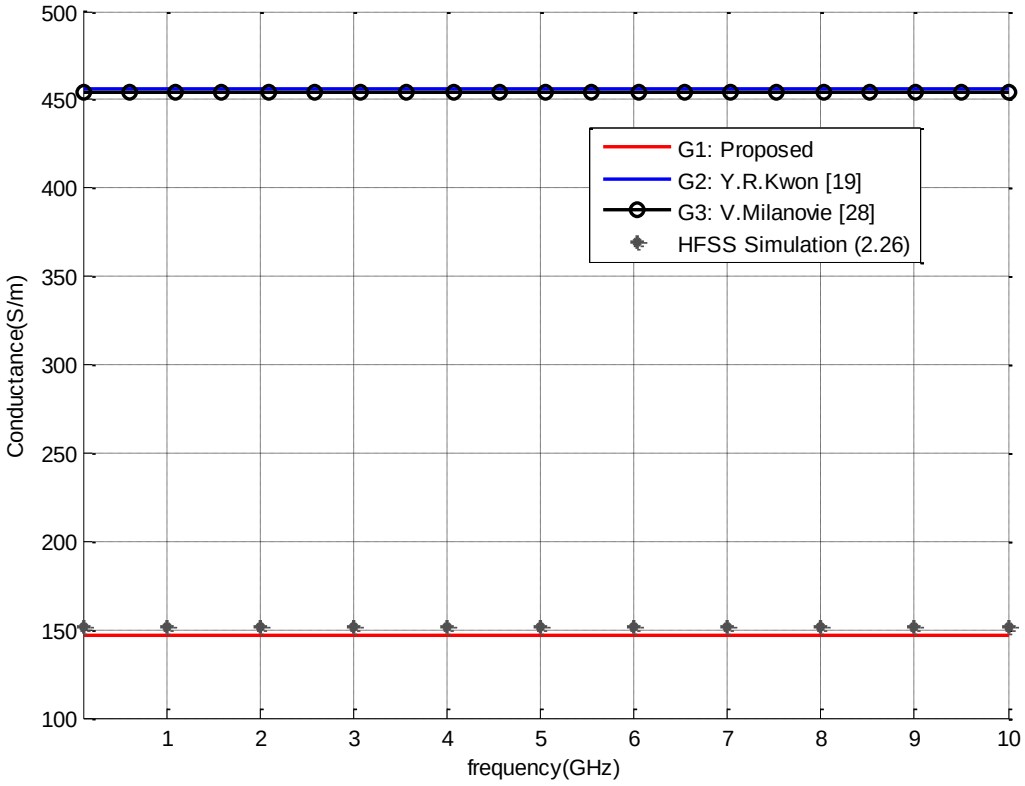

Figure 3.9: Comparison of conductance calculations of the semiconducting layer in Fig 3.3. w=40μm, s=5μm, t=1.5μm, b_1=0.53μm, ε_1=ε_2=12.9, b_2=3μm, σ_s=1× 10^4 (S/m), σ=3× 10^7(S/m).

Figure 3.9 shows the frequency response of the conductance of semiconducting layer. G_1 is calculated by equation (3.20). As can be observed from the graph, only G_1 and G_3 can accurately model the transverse substrate loss. The calculated values for G_2 cannot accurately predict the conductance of the thin-film MIS coplanar structure.

3.5 Comparison of the state-of-the-art models for MIS coplanar slow-wave structures

In this part, a comparison of the state-of-the-art models for MIS coplanar slow-wave structures is made; the criteria for accurate evaluation of the models must include the following factors:

1) Accurate modeling of both external inductance and internal inductance $L_e + L_i$

2) Accurate modeling of the conductor loss resistance R_m

3) Accurate modeling of the longitudinal substrate loss resistance R_L

4) Accurate modeling of the transverse substrate loss conductance G_t

5) The capacitance C of the insulation layer including the fringing effect

The state-of-the-art MIS coplanar slow-wave (MIS-CSWS) models are listed and compared in Table 3.2. The performance of these models is compared with full-wave simulations and reported experiment results.

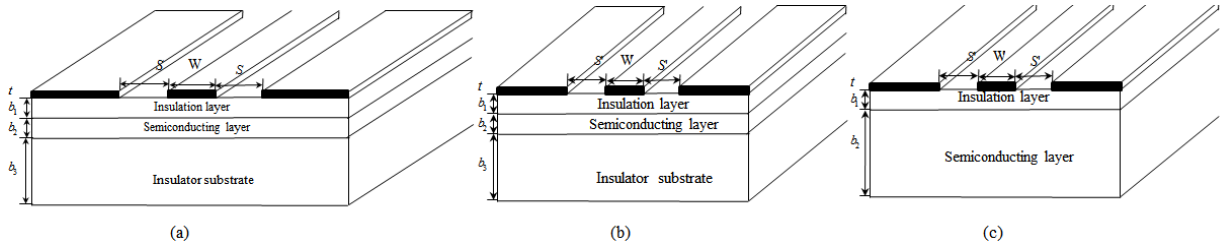

Figure 3.10: MIS coplanar SWS used for the comparison of different models. (a) Thin-film MIS-CSWS. (b) thin-film μ-sized MIS-CSWS. (c) thick-film μ-sized MIS-CSWS.

As shown in Figure 3.10, three MIS coplanar slow-wave structures are used for the evaluation of different models. They are thin-film MIS coplanar slow-wave structure in Figure 3.10 (a) for evaluating the capability of predicting accurately the transverse substrate loss; Thin-film micrometer-sized MIS coplanar slow-wave structure in Figure 3.10 (b) for evaluating the capability of predicting accurately the conductor loss; Thick-film micrometer-sized MIS coplanar slow-wave structure in Figure 3.10 (c) for evaluating the capability of predicting accurately the conductor loss and longitudinal substrate loss. The state-of-the-art modeling techniques for the MIS coplanar slow-wave structure are listed in Table 3.2. The information on how many lumped elements are included in their proposed model is also summarized. Observed from the models listed in Table 3.2, the model presented by Kwon [19] and Milanović [28] are used to compare

with the proposed model. This is because the above two models included as many lumped elements into consideration as possible.

Table 3.2: Comparison of the state-of-the-art MIS coplanar slow-wave models

	L_e	L_i	R_m	R_L	C	G_t	C_t
Y. R. Kwon [19]	✓		✓	✓	✓	Thick-film	
V.Milanovié[28]	✓	✓	✓	✓	✓	Thick film	✓
Jin-Su Ko [31]	✓		Thick metal		✓	Thick film	
J. Lescot [32]	✓		✓		✓	Thick-film	
L. Liu [33]	✓	✓	✓		✓	Thick-film	✓
P. S. Wang [34]	✓		Thick metal		✓	Thick film	
Ch. Seguinot [35]	✓		✓	✓	✓	Thin-film	✓

3.5.1 Thin-Film MIS Coplanar Slow-wave Structure

As shown in Figure 3.9 (a), the structural parameters and the material parameters of the Thin-Film MIS Coplanar Slow-wave Structure are given below:

$$W = 100\mu m, S = 450\mu m, t = 1.0\mu m, b_1 = 0.4\mu m, b_2 = 3\mu m, b_2 = 530\mu m$$
$$\sigma = 4.09\times10^7 (S/m), \sigma_s = 1.8\times10^4 (S/m), \varepsilon_{r1} = 8.5, \varepsilon_{r2} = 13.1$$

Observed from Figure 3.11, both the proposed model and Milanovie's model can predict the attenuation, slow-wave factor and characteristic impedance very accurately within the whole frequency range from 0.1GHz to 3GHz. The reason why Milanovie's model can also predict the attenuation quite accurately in this case is because the longitudinal loss resistance for the thin-film MIS coplanar structure is very large. Inaccurate calculation of R_L will not affect the result. As expected, the Kwon's model fails to predict both attenuation and slow-wave factor. This is because the geometrical filling factor F_0 in Kwon's model is a good approximation for the thick-film MIS coplanar slow-wave structure only but not for the thin-film case.

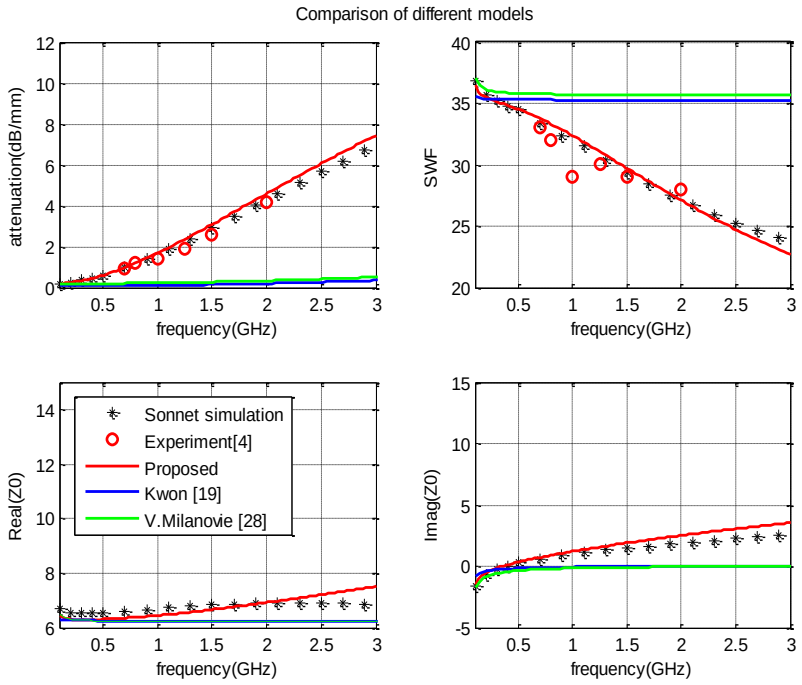

Figure 3.11: Comparison of the modeled, simulated and reported measurement results.

Figure 3.12(a) and Figure 3.12(b) are the simulated and modeled results with different transverse geometrical dimensions respectively. We can observe that these two results are very close to each other, which verify the effectiveness of the proposed model. With the continuous reduction in transverse geometrical dimensions, the SWF and attenuation continue to decrease. This is due to the continuous reduction in the total transverse capacitance and transverse substrate loss, which in turn increases the characteristic impedance.

Figure 3.13 is the calculated loss contribution results with different transverse geometrical dimensions. For the original thin-film MIS structure, the transverse substrate loss dominates. With the continuous reduction in transverse geometrical dimensions, the conductor loss increases while the transverse substrate loss continues to decrease. The longitudinal substrate loss maintains at a low level.

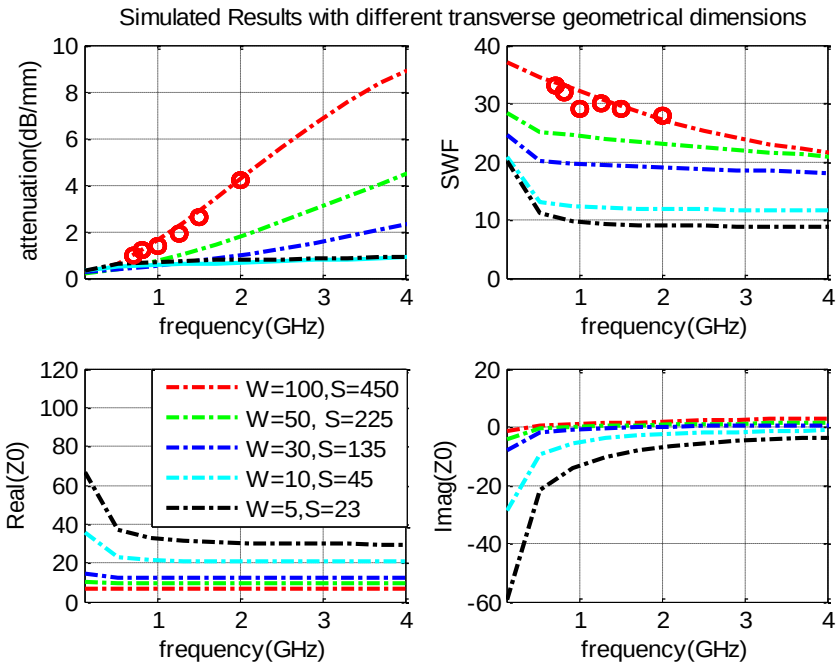

(a)

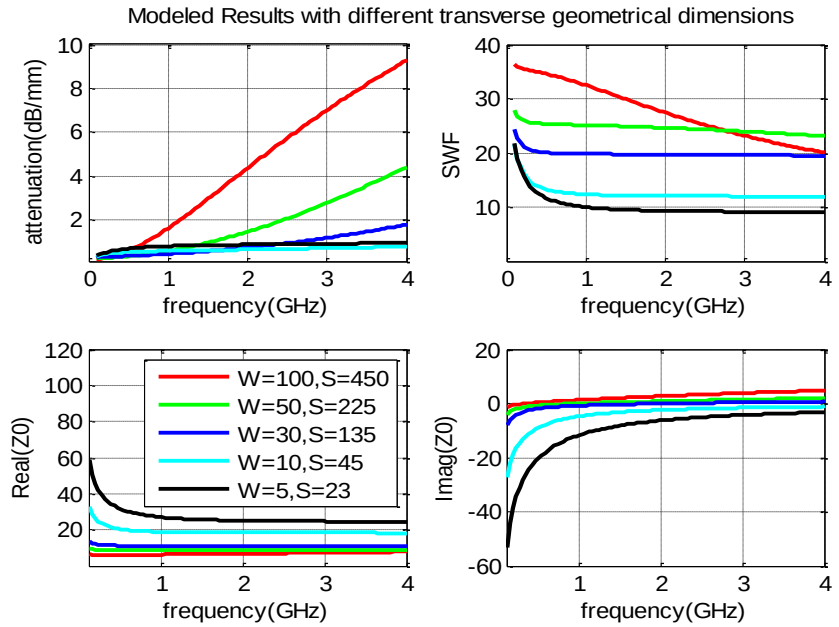

(b)

Figure 3.12: Calculated results with different transverse geometrical dimensions. (a) Simulated. (b) Modeled.

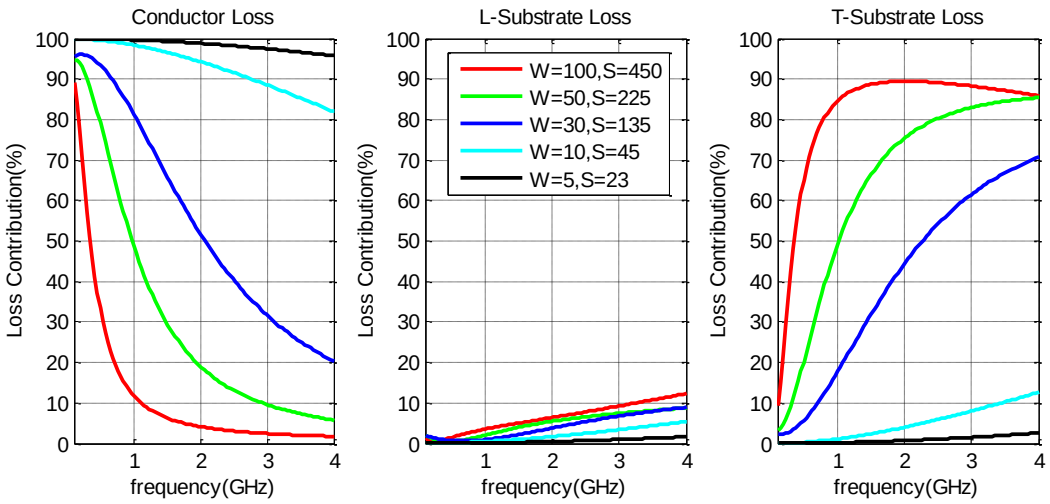

Figure 3.13: Calculated loss contribution results with different transverse geometrical dimensions.

3.5.2 Thin-Film micrometer-sized MIS Coplanar Slow-wave Structure

As shown in Figure 3.10 (b), the structural parameters and the material parameters of the Thin-Film MIS Coplanar Slow-wave Structure are given below:

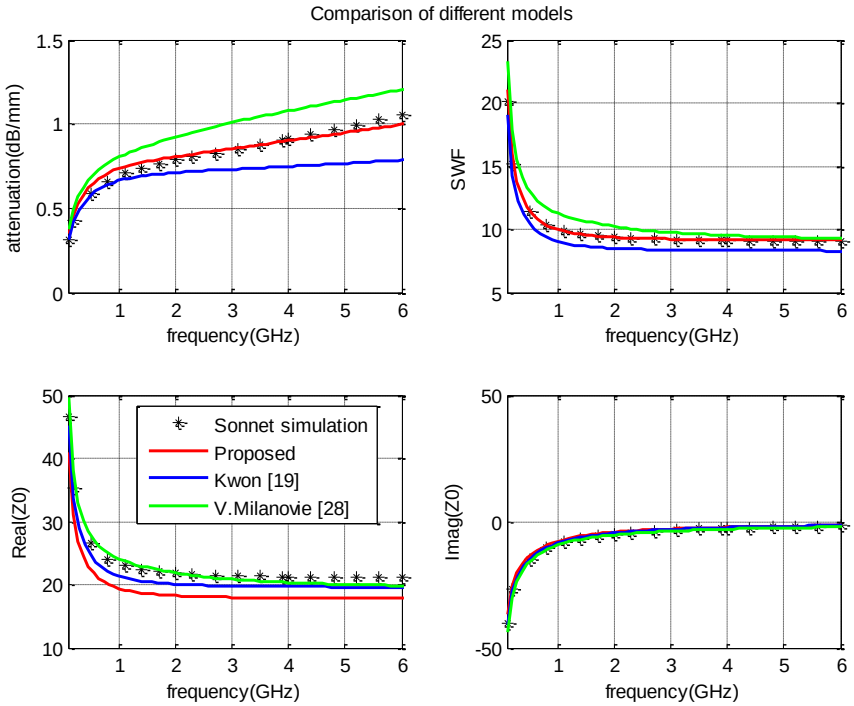

Figure 3.14: Comparison of the modeled and simulated results.

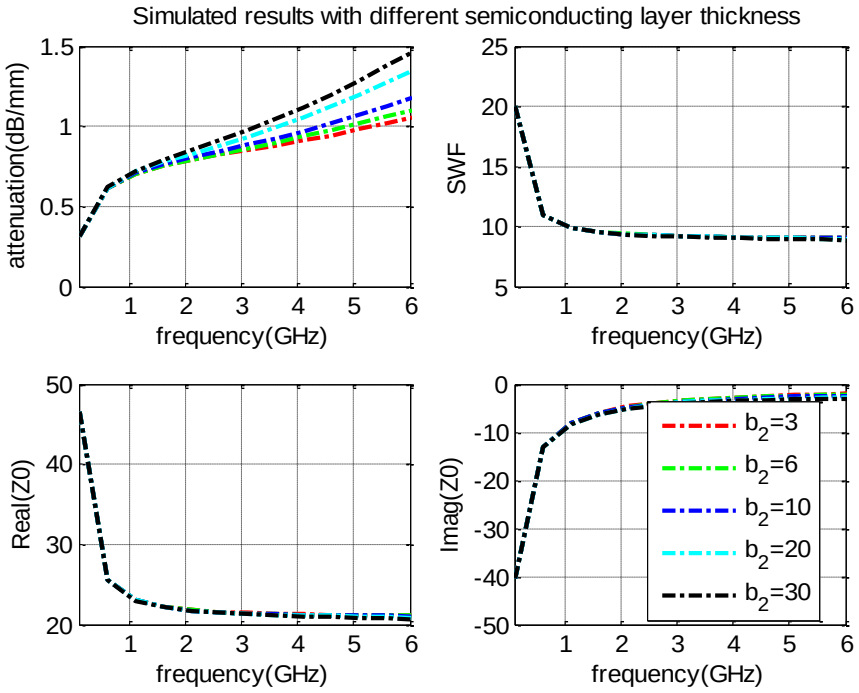

(a)

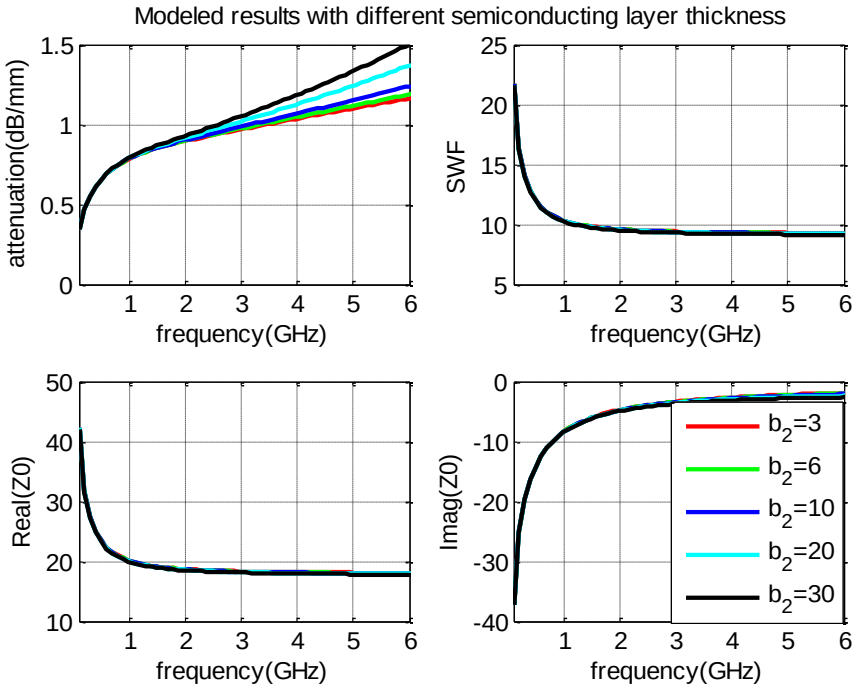

(b)

Figure 3.15: Calculated results with different semiconducting layer thickness. (a) Simulated. (b) Modeled.

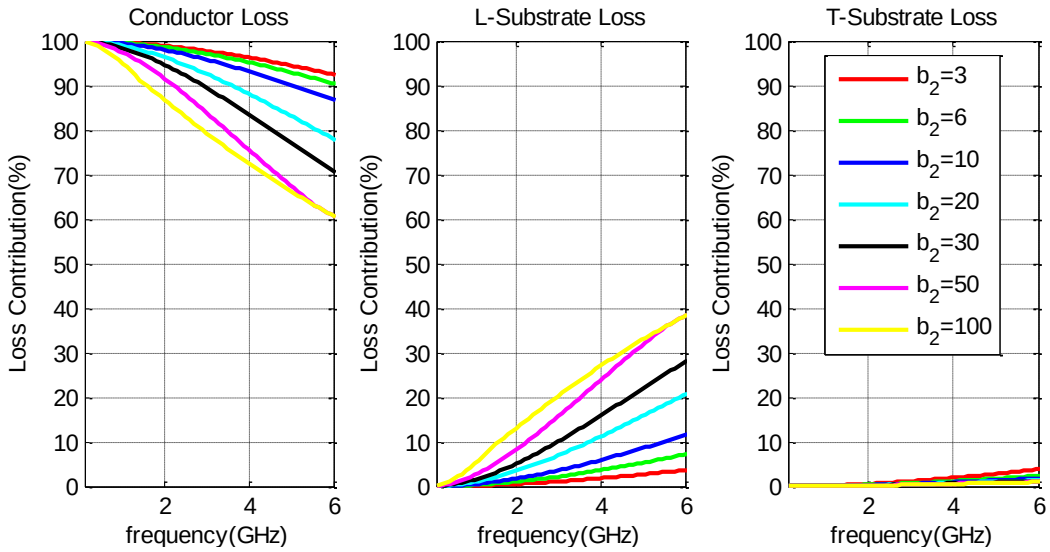

Figure 3.16: Modeled loss contribution results with different semiconducting layer thickness.

$$W = 7.5\mu m, S = 10.5\mu m, t = 1.0\mu m, b_1 = 0.4\mu m, b_2 = 3\mu m, b_3 = 530\mu m$$
$$\varepsilon_{r1} = 8.5, \varepsilon_{r1} = 13.1, \sigma = 4.09\times10^{7}(S/m), \sigma_s = 1.8\times10^{4}(S/m)$$

Observed from Figure 3.14, all of the three modes give very accurate results for slow-wave factor and characteristic impedance. The only big difference lies in the prediction of the attenuation. Only the results by the proposed modeling technique agree very well the the full-wave sonnet simulation results, which is contributed to the comparatively more accurate modeling of the equivalent resistance.

Figure 3.15(a) and Figure 3.15(b) are the simulated and modeled results with different semiconducting layer thickness respectively. We can observe that these two results are very close to each other, which verify the effectiveness of the proposed model. With the continuous increase in semiconducting layer thickness, only the total attenuation continues to increase. Both *SWF* and characteristic impedance remain the same. This is because once the dimensions of the CPW circuit are defined, both the effective inductance and the effective capacitance are determined.

The calculated loss contribution results with different semiconducting layer thickness are shown in Figure 3.16. For the original thin-film micrometer-sized MIS structure, the conductor loss dominates. When the semiconducting layer thickness increases, the contribution of the conductor

loss decreases while the contribution of the longitudinal substrate loss continues to decrease. The transverse substrate loss is not sensitive to semiconductor layer thickness.

3.5.3 Thick-Film micrometer-sized MIS Coplanar Slow-wave Structure

As shown in Figure 3.10 (c), the structural parameters and the material parameters of the thick-film MIS coplanar Slow-wave Structure are given below:

$$W = 7.5\mu m, S = 10.5\mu m, t = 1.0\mu m, b_1 = 0.53\mu m, b_2 = 530\mu m$$
$$\sigma = 3.5\times 10^7 (S/m), \sigma_s = 5000(S/m), \varepsilon_{r1} = 4, \varepsilon_{r1} = 12$$

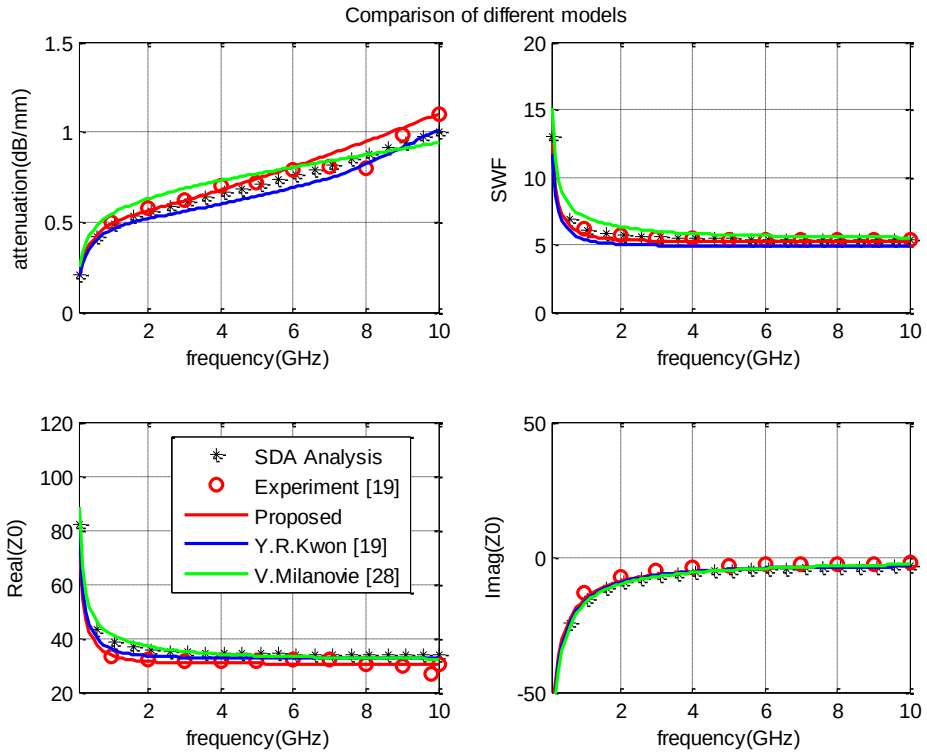

Figure 3.17: Comparison of the modeled, simulated and reported measurement results.

Observed from Figure 3.17, all of the three models can accurately predict the performance of the above thick-film MIS coplanar structure. Comparatively, the proposed model shows closer results with simulation and measurement results [19]. Another observation is that a very low attenuation is achieved at the cost of reduced slow-wave factors. The characteristic impedance can be easily designed to be integrated with the standard 50 ohms systems.

Table 3.3: Comparison of the state-of-the-art MIS coplanar slow-wave models

Models	Thin-film MIS coplanar slow-wave structures			
	α	*SWF*	$Z_{c,r}$	$Z_{c,i}$
Proposed	✓	✓	✓	✓
Kwon[19]			✓	✓
Veljko[28]	✓	✓	✓	✓
	Thin-film micrometer-sized MIS coplanar slow-wave structures			
	α	*SWF*	$Z_{c,r}$	$Z_{c,i}$
Proposed	✓	✓	✓	✓
Kwon[19]		✓	✓	✓
Veljko[28]			✓	✓
	Thick-film micrometer-sized MIS coplanar slow-wave structures			
	α	*SWF*	$Z_{c,r}$	$Z_{c,i}$
Proposed	✓	✓	✓	✓
Kwon[19]	✓	✓	✓	✓

In Table 3.3, the performance of the above three state-of-the-art models are compared and summarized. The criteria for practical evaluation of the models is that the performance (attenuation, slow-wave factor and characteristic impedance) of both thick-film and thin-film MIS coplanar slow-wave structures can be predicted accurately by the same model. The conclusion is that all of the above three models can give accurate results for thick-film MIS slow-

wave structures, but only the proposed model can solve both the thick-film and thin-film structure in a unified way. In the following chapter, the proposed model will be used to design the VO_2-loaded thermo-tunable MIS coplanar structures.

3.6 Analysis of the MIS coplanar slow-wave structures

Since losses and slow-wave effects depend greatly on the field distribution inside the MIS structure, extensive and accurate analysis is needed for the determination of the most favorable conditions for the MIS structure. In this section, the influence of the various structural and dielectric parameters on the characteristics of the thin-film MISCPW is investigated. Design criteria are given for low-attenuation slow-wave propagation based on the proposed modeling techniques presented in section 3.2.

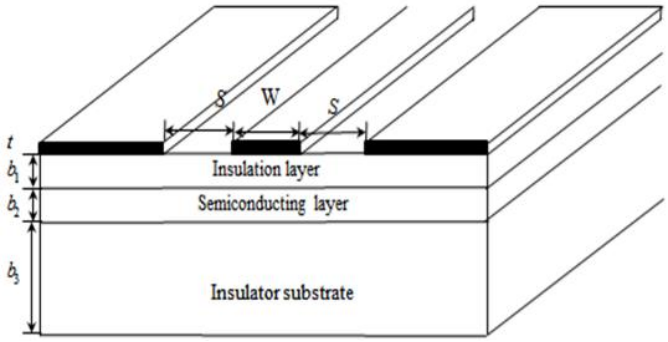

Figure 3.18: Illustration of the thin-film MISCPW.

Figure 3.18 is a sketch of the thin-film MIS coplanar waveguide. The performance of the thin-film MISCPW depends on a number of quantities: the frequency *f*, the widths of the strip conductor W, the distance between the ground planes *w*+2*s*, the thickness of the top metallization *t*, the thickness of each substrate layer b_i (i=1,2,3), the dielectric constant and resistivity of the semiconducting layer. For the thin-film MISCPW, the conductor loss is very low (see Figure 3.13), so the thickness of the metallization has a negligible effect. The influence of the insulator substrates (quartz or sapphire for example) can be neglected too. Because of the scaling properties of the Maxwell's Equations, the results obtained at 1GHz can be easily extended to other structure by reducing the geometrical dimensions and the resistivity of the semiconducting

layer by a factor of *f* at *f* GHz.

In section 3.5.1, we have demonstrated the agreement between the attenuation and the slow-wave factors calculated by the modeling techniques with the full-wave solutions and the results experimented by Hasegawa [4]. These results suggest the feasibility of the equivalent circuit for the extensive analysis of the slow-wave MISCPW with acceptable accuracy. In the following analysis, two criteria other than one must be satisfied: 1. Increase the Q factors $Q=\beta/2\alpha$; 2. the slow-wave factor must be larger than the predefined value over the whole frequency range. Here we choose 15 for example.

3.6.1 Effect of thickness ratio and transverse ratio

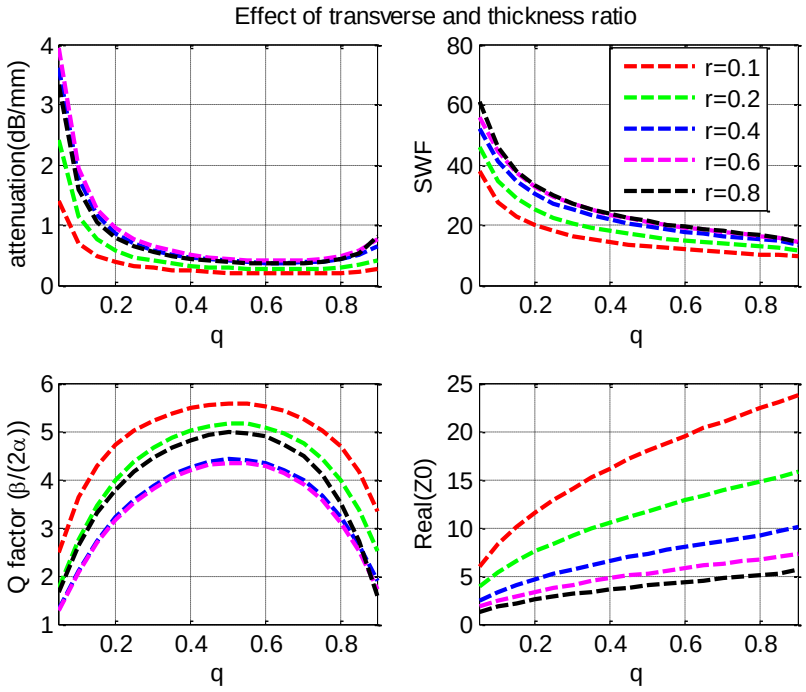

Figure 3.19: Effect of thickness ratio and transverse ratio, f=1GHz, *s*=450μm, *w*=100μm, *t*=1μm, b_1=0.4μm, b_2=3μm, b_3=530μm, $\sigma_s=1.8\times10^4$ (S/m), ε_{r1}=8.5, ε_{r2}=13.1.

We start our calculations of the attenuation, slow-wave factors, the Q factors and the characteristic impedance from the structure experimented by Hasegawa [4]. The attenuation, *SWF*, Q factors and Z_c are plotted against the thickness ratio *q* and the transverse ratio *r* at 1GHz in Figure 3.19, where

$$q = \frac{b_1}{b_1 + b_2}, \quad r = \frac{w}{w + 2s} \tag{3.48}$$

q and r are used to characterize the geometrical dimensions and the layer thicknesses. The thickness of the insulation layer plus the semiconducting layer and the total distance between the grounds w+2 s are kept the same as that in [4].

It is observed in Figure 3.19 that both the attenuation and the slow-wave factor depend greatly on the thickness ratio q and the transverse ratio r. The competing effect between the attenuation and the slow-wave factor can be evaluated by the Q factor. When the transverse ratio r=0.1 and the thickness ratio q≈0.5, we have the highest Q factor. The characteristics of the real part of the characteristic impedance Z_c can be explained by means of the traditional Q-TEM transmission lines. The semiconducting layer has the effect of confining the electric field inside the insulation layer. When the thickness ratio q increases, the capacitance per unit length reduces and so the characteristic impedance increases. We can also observe that when the transverse ratio r increases, the capacitance per unit length increases and so the characteristic impedance decreases.

3.6.2 Effect of ground distance

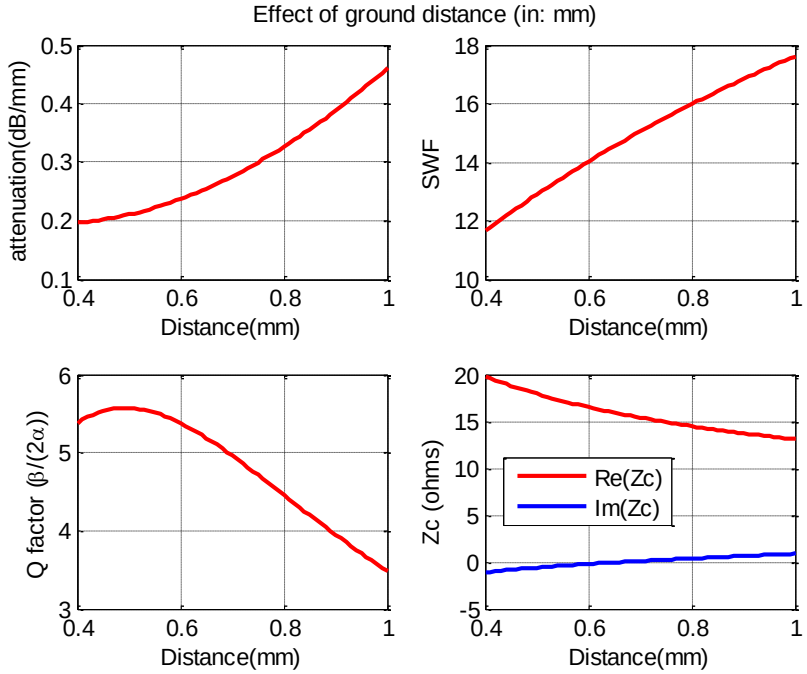

Figure 3.20: Effect of ground distance of the thin-film MISCPW, f=1GHz, b_1+ b_2=3.4μm, r=0.1, q=0.5, t=1μm, σ_s=1.8 × 10^4 (S/m), ε_{r1}=8.5, ε_{r2}=13.1.

As is shown in Figure 3.19, when the ground distance is kept the same, attenuation can be minimized by reducing the width of the central signal line *w*. In fact, the attenuation can be minimized by reducing the *w* and the ground distance *w*+2*s* at the same time.

Figure 3.20 shows the computed characteristics of the thin-film MISCPW against the ground distance *w*+2*s* with *q*=0.5 and *r*=0.1. When *w*+2*s* decreases, both the attenuation and the slow-wave factor decrease continuously. But the *SWF* decreases to a lesser extent. The highest Q factor can be obtained when the ground distance *w*+2*s*=500 μm. The real part of Z_c slightly increases because of the reduced capacitance per unit length when the width of the central signal line decreases. The imaginary part of Z_c has a very small value close to zero.

3.6.3 Effect of conductivity, permittivity and thickness of the semiconductor layer

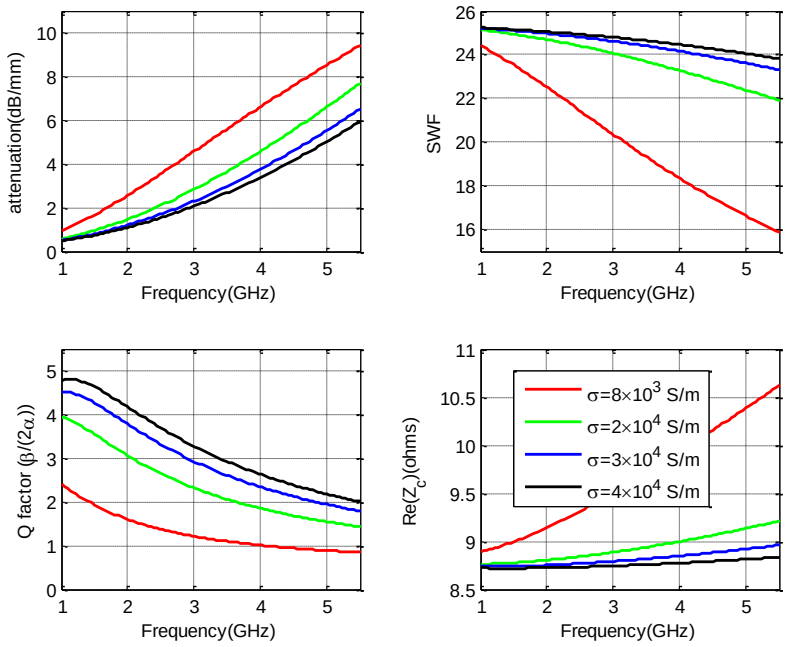

Figure 3.21: Effect of conductivity of the semiconducting layer, *s*=225μm, *w*=50μm, *t*=1μm, b_1=0.4μm, b_2=3μm, ε_{r1}=8.5, ε_{r2}=13.1.

The semiconducting layer has the effect of confining the electric field mainly inside the

insulation layer, thus increasing the p-u-l capacitance. The conductivity of the semiconducting layer has a big influence on the characteristics of the thin-film MISCPW. To satisfy the two design criteria of the MISCPW at the same time, as is shown in Figure 3.21, the characteristics of the thin-film MISCPW is computed against frequency with different conductivity values of the semiconducting layer. It is observed that when the conductivity σ_s increases, the slow-wave factor increases while the attenuation decreases, which leads to a big increase in the Q factor. The real part of Z_c also decreases because more electric field is confined inside the insulation layer when the conductivity increases.

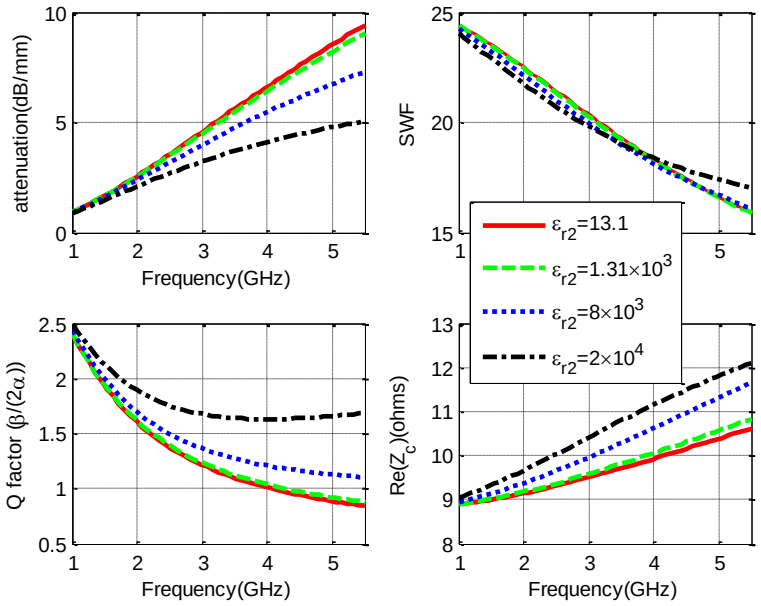

Figure 3.22: Effect of permittivity of the semiconducting layer, s=225μm, w=50μm, t=1μm, b_1=0.4μm, b_2=3μm, σ_s=8000(S/m), ε_{r1}=8.5.

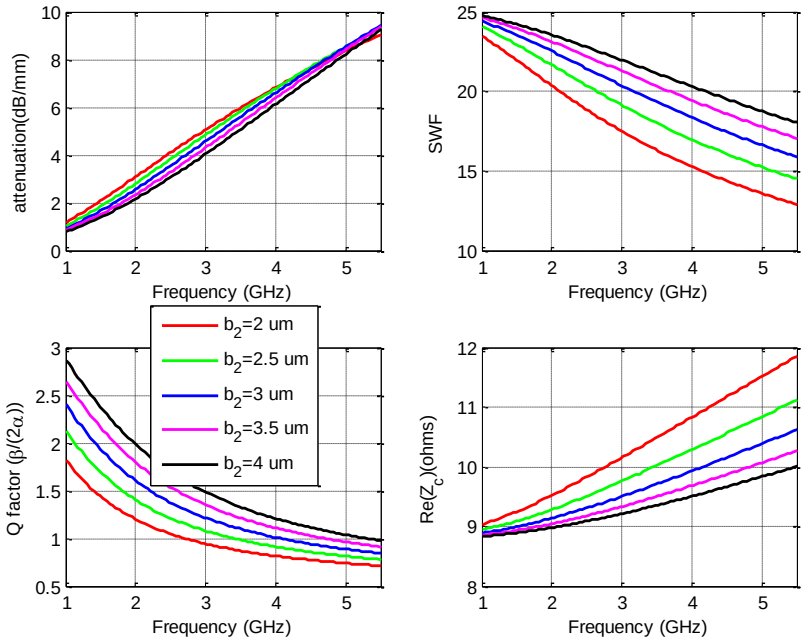

Figure 3.23: Effect of semiconductor layer thickness, s=225μm, w=50μm, t=1μm, b_1=0.4μm, σ_s=8000(S/m), ε_{r1}=8.5, ε_{r2}=13.1.

The study of the permittivity of the semiconducting layer on the characteristics of the thin-film MISCPW is very important for the further design of the VO_2-loaded thermo-tunable coplanar SWS. This is because the VO_2 thin film shows a high relative dielectric constant because of the dielectric mixture phenomena. It is seen in Figure 3.22 that the permittivity of the semiconducting layer has the similar influence as the conductivity on the attenuation and the Q factor but the slow-wave factor is less sensitive to the permittivity of semiconductor layer.

As is shown in Figure 3.23, when the thickness b_2 increases, the slow-wave factor increases while the attenuation decreases, which leads to an increase in the Q factor. The real part of Z_c also decreases because more electric field is confined inside the insulation layer when the thickness b_2 increases. Here the conductivity is chosen as σ_s =8000(S/m). This is because the measured conductivity of the VO_2 thin-film at 70^{o}C is close to 8000(S/m). By doing so, we can make sure the designed thermo-tunable VO_2-loaded MISCPW has a performance not worse than that when the temperature increases over T_c.

3.6.4 Effect of permittivity of the insulation layer

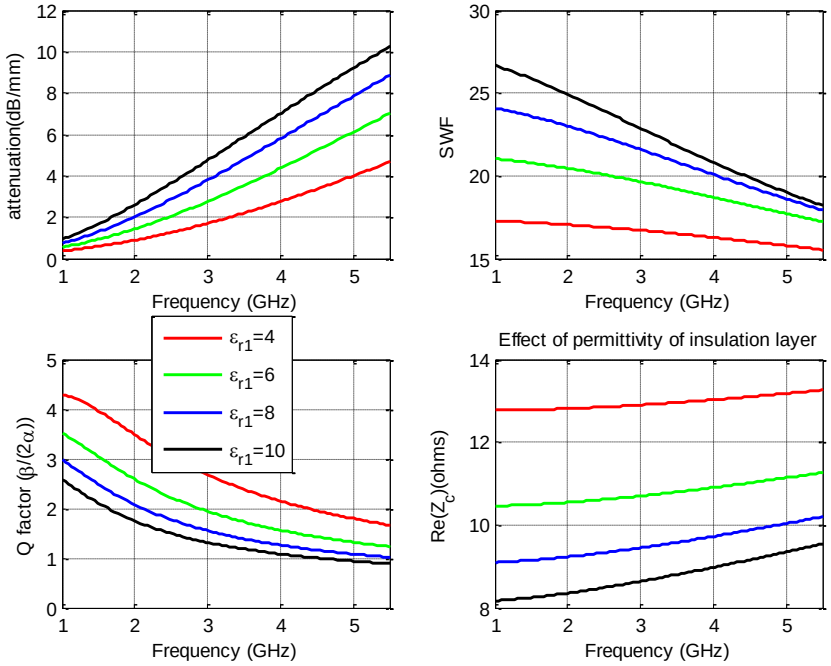

Figure 3.24: Effect of permittivity of the insulation layer, s=225μm, w=50μm, t=1μm, b_1=0.4μm, b_2=4μm, σ_s=8000(S/m), ε_{r2}=13.1.

The permittivity of the insulation layer has a big influence on the characteristics of the thin-film MISCPW. When the permittivity increases, more electric field is confined inside the insulation layer and will have more interaction with the semiconducting layer. Thus the slow-wave factor increases and the attenuation decreases.

As is shown in Figure 3.24, the characteristics of the thin-film MISCPW is plotted against the frequency with different permittivity of the insulation layer. It is observed that when the permittivity ε_{r1} decreases, both the slow-wave factor and the attenuation decrease. But the slow-wave factor decreases to a less extent which leads to an increase in the Q factor. The real part of the Z_c increases because less electric field is confined inside the insulation layer when permittivity ε_{r1} decreases. So the p-u-l capacitance decreases.

3.6.5 Effect of thickness of the insulation layer

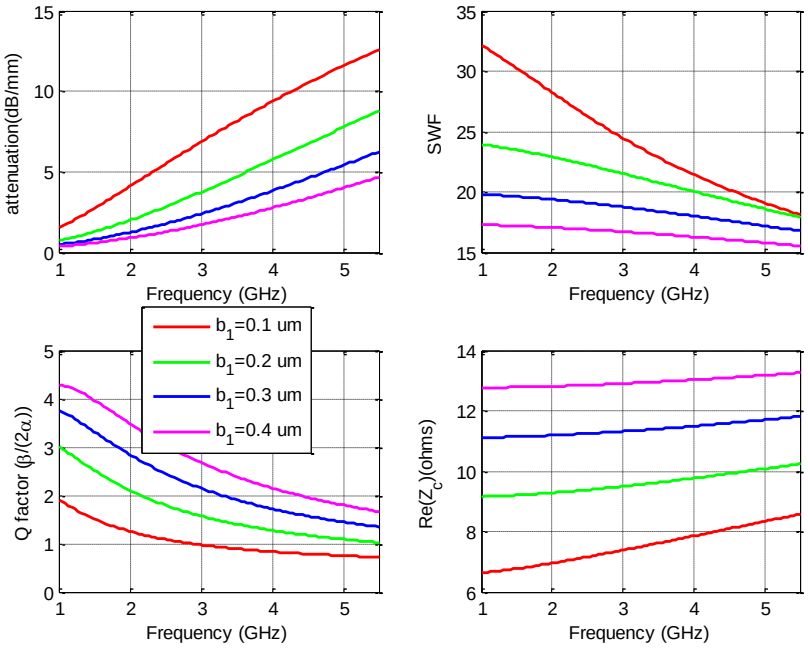

Figure 3.25: Effect of thickness of the insulation layer, S=225μm, W=50μm, t=1μm, b_2=4μm, σ_s=8000(S/m), ε_{r1}=4, ε_{r2}=13.1.

The effect of the insulation layer b_1 is plotted in Figure 3.25. As expected, when the thickness b_1 decreases, more electric field will be confined inside the insulation layer, which leads to an increase in the attenuation and the slow-wave factor but a decrease in the real part of Z_c. The Q factor decreases when the thickness b_1 decreases.

From the above analysis, we can come to the conclusion that:

1) To increase the slow-wave factor and reduce the attenuation at the same time, we can increase the conductivity σ_s , the permittivity ε_{r2} or the thickness b_2 of the semiconductor layer.

2) The thickness ratio q, transverse ratio r, ground distance W+2S, the permittivity ε_{r1} and the thickness b_1 of the insulation layer have a competing influence on the slow-wave factor and the attenuation.

CHAPTER 4 THERMO-TUNABLE MIS COPLANAR SLOW-WAVE STRUCTURES BASED ON VANADIUM DIOXIDE PHASE TRANSITION

4.1 Introduction

The MIS coplanar slow-wave structure can be used to reduce the size and cost of the passive circuit to realize phase shifters and delay lines. According to the analysis in section 3.6, the conductivity and the permittivity of the semiconducting layer have substantial influence on the performance of the MISCPW. As the permittivity and the conductivity of the VO2 thin-film increase continuously with temperature, we can design a thermo-tunable MIS coplanar slow-wave structure if we substitute the semiconducting layer in conventional MIS structures by the VO_2 thin-film. This is very useful for the design of tunable delay lines, phase shifters, or tunable filters. This chapter is organized as follows:

1) First, the general material properties of VO_2 is introduced, followed by the preparation techniques, preparation process and excitation method.

2) Broadband relative dielectric constant of VO_2 thin-film at semiconductor state and metal state is experimentally extracted. Comparison of the measured data with the published results is also made along with the reason why high relative dielectric constant of VO_2 thin-film is observed at metal phase.

3) Finally, based on the extracted dielectric constant of the vanadium dioxide thin film and the extensive analysis of the MISCPW, a thermo-tunable MISCPW based on the VO_2 phase transition is demonstrated.

4.2 The material properties of VO_2 thin-film

The VO_2 is a highly correlated transition-metal oxide with SMT at 68 ℃. SMT exhibits a huge change in infrared transmission and resistivity shown in Figure 4.1 [42]. At room temperature, VO_2 has a monoclinic structure [42] with shorter distances between pairs of V atoms indicating metal-metal bonding. Above 68 ℃ the structure changes to a tetragonal structure [42] and the metal-metal bonds are broken causing an increase in electrical conductivity and magnetic susceptibility as the bonding electrons are “released”.

The properties of SMT in VO_2 vary greatly with different structure parameter; substrate choice [43], device sizes [44] and sample deposition conditions [45-46] have great influence on the parameters of SMT. The characterization for the quality of the VO_2 thin film is given via electrical measurement of resistance change ΔR and transition width ΔT_{MIT}. Extensive research has been conducted on the VO_2 thin film growth. Representative preparation techniques of VO_2 thin films are [47]: sputtering deposition, chemical vapor deposition, Sol-Gel Synthesis and Pulsed Laser Deposition.

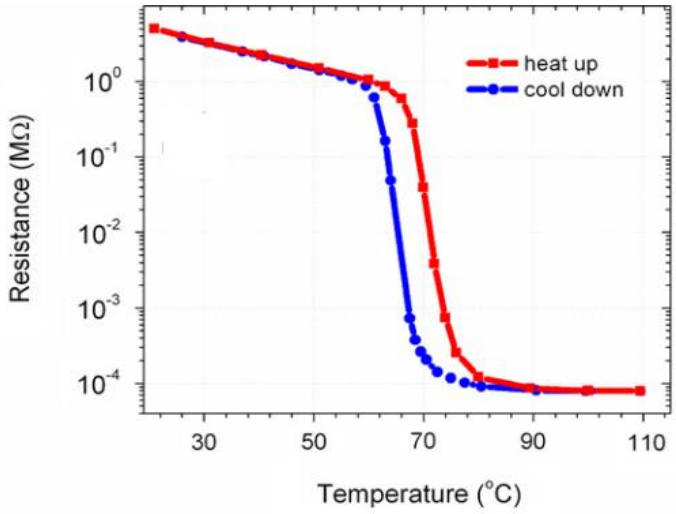

Figure 4.1: Resistance change of VO_2 thin-film versus temperature [37].

The reported SMT is usually observed when VO_2 is thermally heated above transition temperature. Besides, SMT can also be induced by optical [48] and electrical excitation [49]. Different excitation methods pose different requirements on the size of VO_2 in the circuit. A typical intensity value of the laser sufficient to excite VO_2 (200nm in thickness) is 25mJ/cm2 [50], if excited electrically, the typical value of the field strength is in the order of MV/m[51], which means to excite a 100um by 100um size of VO_2, we need a voltage of at least 100V to produce a 1MV/m electric field strength on VO_2 to induce SMT, because of this, the size of VO_2 which is electrically excited is limited to tens of micros in dimension. While compared to electrically excited VO_2, thermal excitation could be employed if one layer of VO_2 needs to be excited. So we conclude that to utilize VO_2 in planar waveguide circuit (like CPW and microtrip line) as a dielectric layer, thermal excitation or optical excitation is needed.

For the mechanism of SMT in VO_2, there are several explanations. Mott transition [52] and Peierls transition [53] are the two main transition models. The phase transition can be tuned via the control of key parameters such as band filling, bandwidth, and dimensionality and these parameters are experimentally varied by doping, pressure, chemical composition, and magnetic fields for the transition of VO_2. Controversy still remains whether SMT in VO_2 is a Mott transition or a Peierls transition. In the Peierls transition model, the lattice transformation at structural phase transition temperature is accompanied by the band structure changes that result in the opening of the band gap and thus SMT. In the Mott transition model, electron correlations are considered the first importance to cause SMT while the electron-lattice interactions are of the second importance.

4.3 Broadband Measurement of relative dielectric constant of VO_2 thin-film

4.3.1 Overview of characterization method of vanadium dioxide

Table 4.1: Summary of relative dielectric constant measurement of VO_2 thin-film

Reference	VO_2 form	method	Frequency range	Relative dielectric constant		
				semiconductor	metal	ratio
Hood, P. J. [54]	Thin-film	Quasi-optical method	38GHz	100 60°C	9×10^4	~10^3
Yang [55]	Thin-film	Capacitance method	1MHz	36 23°C	6×10^4	~10^3

As the device scales down to the square root of the relative dielectric constant, the loss increases proportionally to the conductivity, and the impedance matching of the circuit can only be achieved when the relative dielectric constant is known. To better utilize VO_2 in RF-microwave tunable circuit design, the broadband complex permittivity needs to be known first. Up till now,

only two papers have reported the characterization work of VO_2 thin film at two single frequency points of 38GHz [54] and 1MHz [55] respectively, no broadband microwave characterization of the VO_2 thin film has been reported to the best of our knowledge.

Even so, as the permittivity of VO_2 thin film depends greatly on the deposition conditions, the reported permittivity of VO_2 cannot be used directly in our design work. Here in this part, we carried out measurement using coplanar waveguide circuit. For the measurement of relative dielectric constant of semiconductor phase, the VO_2 thin-film is deposited directly below the CPW electrode on the SiO_2 substrate. As for the measurement of the metal phase, an insulation layer of silicon dioxide is deposited between the CPW electrode and the VO_2 thin-film in order to avoid short circuit. The frequency range covers from 2GHz to 30GHz for the semiconductor phase; for the metal phase, the frequency range covers from 1GHz up to 5.5GHz. This work has never been conducted before and is extremely important if researchers want to design VO_2-based microwave circuits.

4.3.2 Device design and VO_2 thin-film fabrication

1) Fabrication of the VO_2 thin-film

Figure 4.2: Reactive pulsed laser deposition facility in INRS.

The deposition work is done in INRS. The 600 nm thick VO_2 thin films were deposited on 530 um thick fused silica substrates by reactive pulsed laser deposition shown in Figure 4.2. A pure

vanadium metal target was ablated using a KrF excimer laser operating at 248 nm at 2 J/cm^2 with a frequency of 10 Hz. Before deposition, the chamber was pumped down to 10^{-6} Torr. During deposition, the oxygen pressure was kept constant at 5 mTorr with an oxygen flow of 5 sccm. The target-substrate distance was set at 6.5 cm and the substrate temperature was kept at 500 ℃. The focusing lens was translated and both substrate and targets were rotated during deposition in order to get good film homogeneity.

2) VO_2-loaded coplanar waveguide design

As temperature increases, the relative dielectric constant of VO_2 will change, which will enable the characteristic impedance of the designed CPW lines to change. To avoid the systematic errors of common measurement techniques when the characteristic impedance of the lines does not match that of the measurement equipment, the Multiline Method [56] is used here. We measure two CPW lines of different lengths without calibrating the equipment and without assuming the port-match.

As the pitch size of the probe we use is 250μm, the line width of the CPW is chosen as w=340μm, the gap between the line and the top ground g=40μm. The length of the line pairs are designed according to the conventional TRL calibration for a ratio of frequency range equals to 8, the substrate used is quartz ($\varepsilon_r = 3.8$). The designed lengths of the CPW lines are listed below in Table 4-2.

Table 4.2: Longitudinal dimensions of the CPW lines

Dimensions	L_1	L_2	L_3	L_4
Values (mm)	5.270	15.810	1.580	4.745

To cover the frequency range from 2GHz to 30GHz, we need to design two sets of CPW transmission line, L_1 and L_2 cover the frequency range from 1GHz to 8GHz, L_3 and L_4 for the frequency range from 3.3GHz to 26.4GHz. According to [56], L_2 is designed as three times the

length of L_1; L_4 is designed as three times the length of L_3. It must be pointed out that the CPW lines are designed for the electrode on bare quartz only, the measurable frequency range will be narrowed when the CPW lines are loaded with the VO_2 thin-film at different temperatures.

4.3.3 Extraction of the effective relative dielectric constant of VO_2-loaded CPW lines

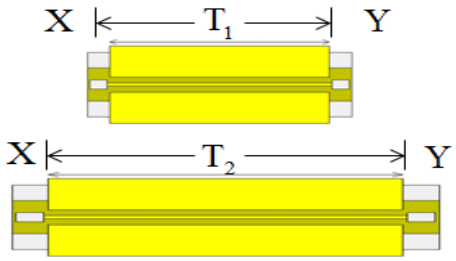

Figure 4.3: Two CPW lines with the same transverse dimensions but different lengths.

First, the uncalibrated S parameter for l_1 and $l_2$was measured, we then form a cascaded matrix M_i, defined as [57]

$$M_i = \begin{bmatrix} -\det(S^i)/S^i_{21} & S^i_{11}/S^i_{21} \\ -S^i_{22}/S^i_{21} & 1/S^i_{21} \end{bmatrix} \tag{4.1}$$

Where

$$M_1 = XT_1Y, \quad M_2 = XT_2Y \tag{4.2}$$

We assume the discontinuities on the left and right of the waveguide is assumed to be the same, so the matrix X and Y are the same in the formulation of matrix M_1 and M_2, then we have

$$M_1M_2^{-1} = XT_1T_2^{-1}X^{-1} \tag{4.3}$$

$$Tr(M_1M_2^{-1}) = Tr(T_1T_2^{-1}) = 2\cosh(\gamma\Delta d) \tag{4.4}$$

$$\gamma = \frac{\ln[\frac{1}{2}(\lambda_1+\lambda_2)]}{\Delta d} = \frac{\ln[\frac{1}{2}(\lambda_1+\lambda_2)]}{l_2-l_1} \tag{4.5}$$

Where λ_1 and λ_2 are the two eigenvalues of matrix $M_1 M_2^{-1}$, then the effective relative dielectric constant of the CPW line can be obtained

$$\varepsilon_{eff} = -(\frac{\gamma}{k_0})^2 \tag{4.6}$$

Where k_0 is the wave number of the free space.

4.3.4 Measurement of the relative dielectric constant of VO_2 at semiconductor phase

The complex permittivity of VO_2 can be extracted by the combination of conformal mapping method (CMM) and partial-capacitance technique (PCT), we refer the reader to [59]. Take a two layered CPW structure shown in Figure 4.4 for example, the transverse dimensions of the VO_2-loaded CPW lines are listed in Table 4-3. The process of performing the CMM is illustrated step-by-step in Figure 4.5.

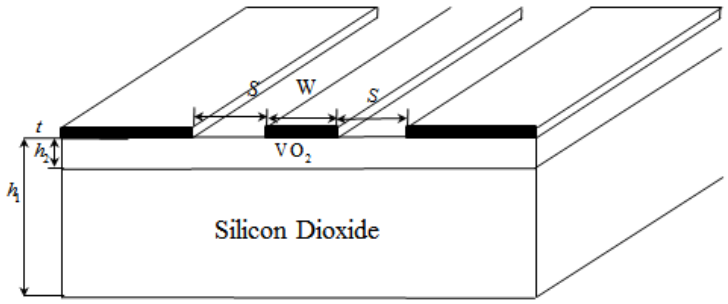

Figure 4.4: Illustration of the VO_2-loaded CPW line for semiconductor phase.

Table 4.3: Transverse dimensions of the CPW lines

Dimensions	w	s	t	h_1	h_2
Units (μm)	340	40	1	530.6	0.6

The effective permittivity can be expressed as the weighted sum of the relative dielectric constant of each layer as

$$\varepsilon_{eff} = 1 + q_1(\varepsilon_1 - 1) + q_2(\varepsilon_2 - \varepsilon_1) \tag{4.7}$$

Where q_i (i=1, 2) are the filling factors which depend on the CPW geometry and calculated by the CMM method, q_i (i=1, 2) are given by

$$q_i = \frac{1}{2}\frac{K(k_i)}{K(k_i')}\frac{K(k_0')}{K(k_0)}, i = 1,2 \tag{4.8}$$

And

$$k_i = \frac{\sinh(\frac{\pi s}{2h_i})}{\sinh(\frac{\pi(s+g)}{2h_i})},\ \ i = 1,2,\ k_0 = \frac{s}{s+g},\ k_i' = \sqrt{1-k_i^2} \tag{4.9}$$

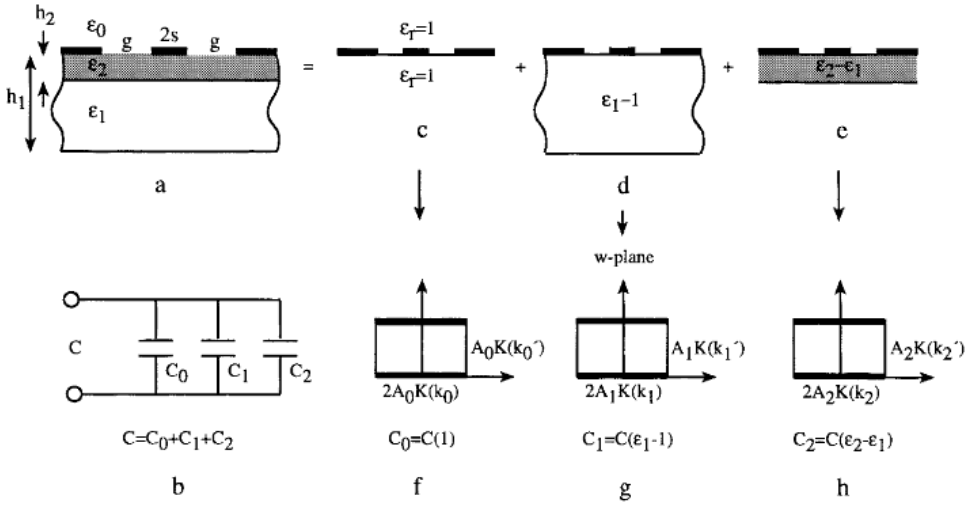

Figure 4.5: CMM and PCT for CPW with two-layer substrate [60].

For VO_2 deposited on quartz substrate, there are two layers and we use the value of ε_1=4.0 for the quartz, then we can obtain the desired relative dielectric constant of VO_2. To eliminate the conductor loss of the CPW line, we define a reference line of the same size and configuration as that of VO2 loaded CPW except that there is no VO_2 layer. So the complex propagation constant of the reference line and test line can be written as [58]

$$\gamma^{ref} = \sqrt{(R + j\omega L)(G^{ref} + j\omega C^{ref})} \tag{4.10}$$

And the complex propagation constant of the VO2 loaded line is given by

$$\gamma^{VO2} = \sqrt{(R + j\omega L)(G^{VO2} + j\omega C^{VO2})} \tag{4.11}$$

As both reference line and VO_2-loaded CPW line use the same structure and conductive material (1um copper), the term R + jωL is the same in both equation (4.10) and equation (4.11).

Combing equations (4.7), (4.10) and (4.11), the complex permittivity of VO_2 can be extracted from the following expression

$$\frac{\varepsilon_{eff}^{VO2} - \varepsilon_{eff}^{ref}}{\varepsilon_{eff}^{ref}} = \frac{q_2(\varepsilon_2 - \varepsilon_1)}{1 + q_1(\varepsilon_1 - 1)} \tag{4.12}$$

So the relative dielectric constant of the VO_2 thin-film at semiconductor phase can be extracted

$$\varepsilon_{VO2} = \frac{\varepsilon_{eff}^{VO2} - \varepsilon_{eff}^{ref}}{\varepsilon_{eff}^{ref}} \frac{1 + q_1(\varepsilon_1 - 1)}{q_2} + \varepsilon_1 \tag{4.13}$$

4.3.5 Measurement of the relative dielectric constant of VO_2 at metal phase

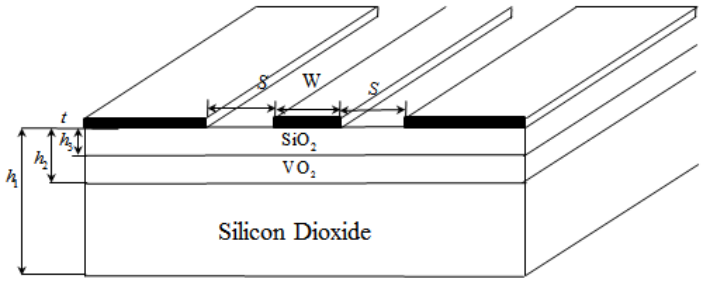

Figure 4.6: Illustration of the fabricated CPW line for metal phase.

For the measurement of the metal phase, an insulation layer of silicon dioxide of the thickness 100nm is deposited between the CPW electrode and the VO2 thin-film in order to avoid short circuit. An illustration of the designed VO_2-loaded CPW lines is shown in Figure 4.6. The transverse dimensions of the CPW lines are listed in Table 4-3. As the electric field of the CPW

lines are strong around the signal line. To have a better field interaction between the VO_2 thin film and the electric field, the thickness of the deposited silicon dioxide must be as thin as possible. The frequency range covers from 1GHz up to 5.5GHz due to the increased effective permittivity.

Table 4.4: Transverse dimensions of the CPW lines for metal phase

Dimensions	w	g	t	h_1	h_2	h_3
Units (μm)	340	40	1	530.7	0.7	0.1

To extract the relative dielectric constant of the VO2 thin-film at metal phase, an optimization process is performed:

1) First, the effective permittivity of the CPW lines $\varepsilon_e = \varepsilon_e' - j\varepsilon_e''$ is experimentally extracted.

2) Then, the starting values of relative dielectric constant ε' and conductivity σ are chosen according to the published results [55].

3) The assumed ε' and σ are fed to the full-wave MoM-based Sonnet® Simulator, from which we can have the simulated value of $\varepsilon_s = \varepsilon_s' - j\varepsilon_s''$.

4) After that, an optimization process combined with the full-wave Sonnet® Simulator is performed to minimize the error function

$$E(\varepsilon,\sigma) = 0.5\left\|\varepsilon_e^{'}\right| - \left|\varepsilon_s^{'}\right\| + 0.5\left\|\varepsilon_e^{''}\right| - \left|\varepsilon_s^{''}\right\| \tag{4.14}$$

5) Optimized results of the $\varepsilon'$and σ can be used as the starting point for the rest of the frequency points.

4.3.6 Experimental results of extracted relative dielectric constant of VO_2 thin-film

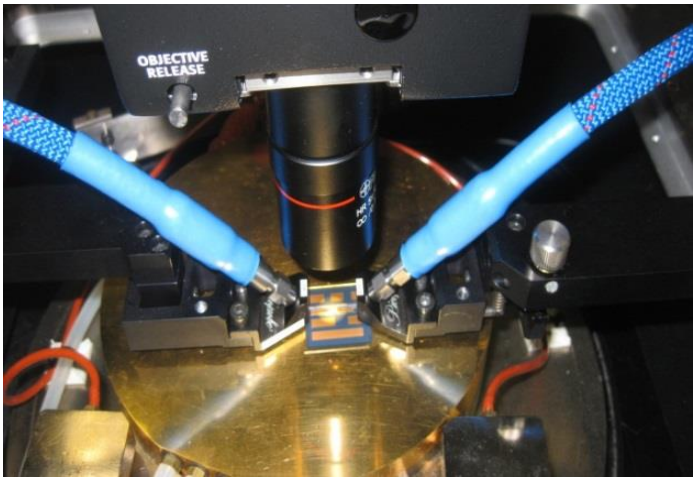

Figure 4.7: Measurement setup for the characterization of VO_2-loaded MIS coplanar circuit.

Figure 4.7 is the measurement setup used for the characterization of VO_2-loaded MIS coplanar circuit. The probing station is a semi-automatic model PA150 from Suss Microtec including a thermal chuck for measurement of the temperature range from -40 C to +150 C. A vacuum pump is used for a better positioning of the circuit on the thermal chunk. The GSG probes of 250µm pitch are connected by the coaxial cable to the Network Analyzer. The Network Analyzer Anritsu 37397 is used for the measurement of S parameters.

1) Experimental results for quartz substrate

In order to check the accuracy of the parameter extraction process, a reference CPW line with only one-layer of quartz substrate is characterized, as shown in Figure 4.7. The dimensions of the CPW line is the same as listed in Table 4-2 and Table 4.3. Following the extraction process in section 4.3.3, we have the experimental results of the effective relative dielectric constant of the reference CPW lines first. As shown in Figure 4.8, for a frequency range from 2GHz to 30GHz, the extracted real part of effective permittivity is close to 2.5, while the imaginary part of the effective permittivity is close to 0, which is very close to results calculated from the LineCalc® from ADS®.

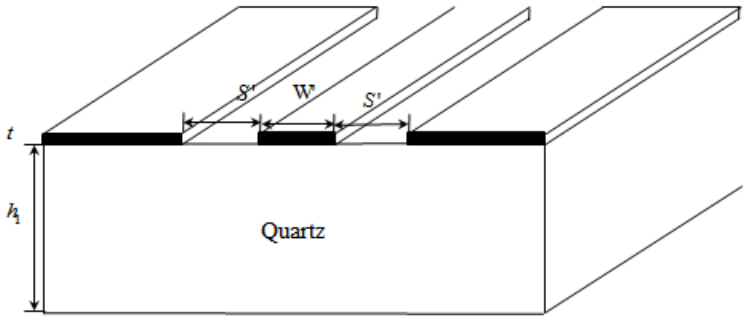

Figure 4.8: Illustration of the fabricated reference line.

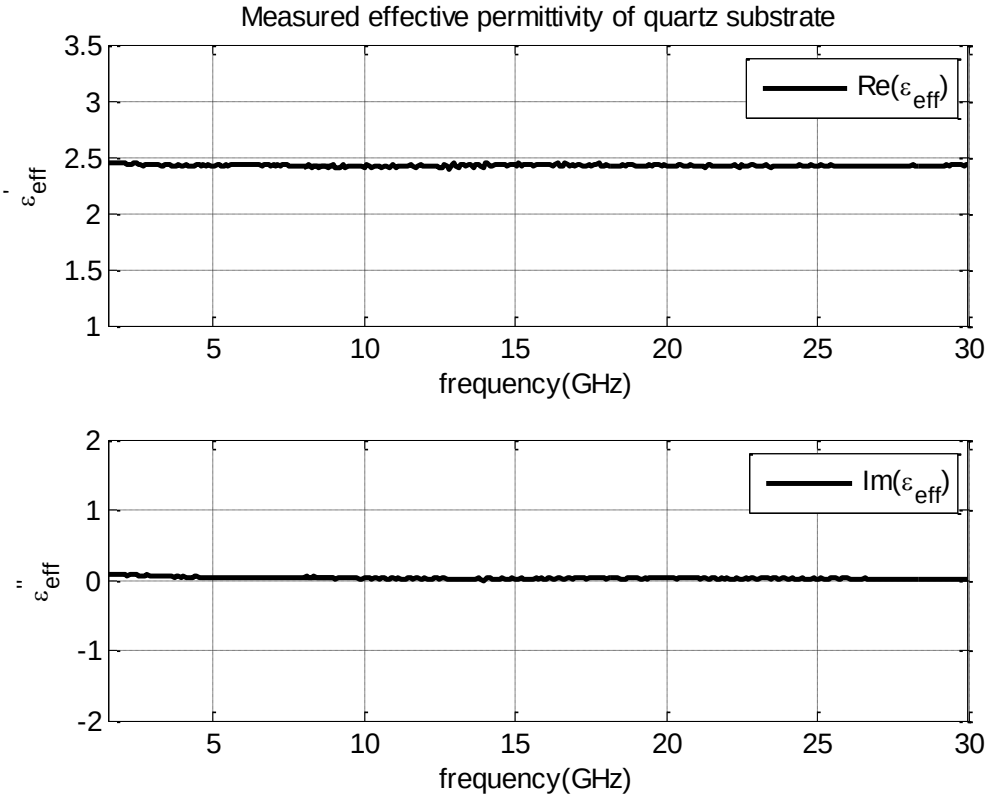

Figure 4.9: Experimental results of the effective relative dielectric constant of the reference line.

The relative dielectric constant of the quartz can be extracted by the combination of conformal mapping method (CMM) and partial-capacitance technique (PCT) following the extraction algorithm in section 4.3.4. As can be observed in Figure 4.9, the extracted permittivity is close to 4 and the conductivity is close to zero over the whole frequency range from 2GHz to 30GHz,

which verifies the feasibility of the parameter extraction process.

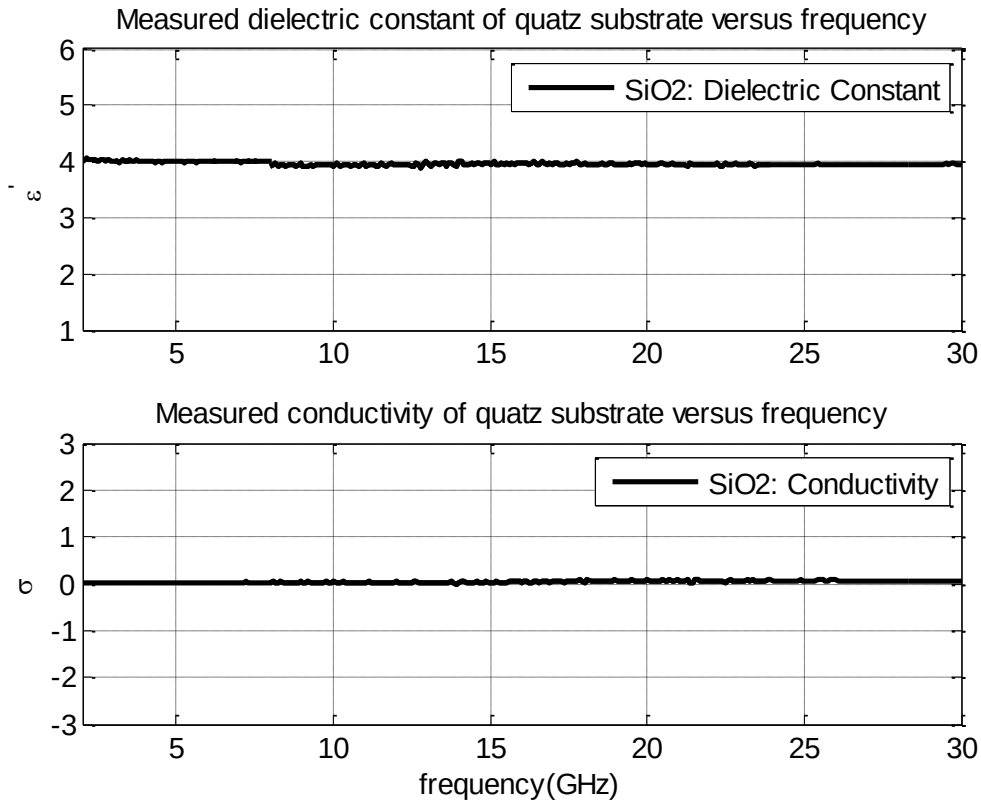

Figure 4.10: Experimental results of the relative dielectric constant of the quartz substrate.

2) Experimental results for VO_2 thin-film at semiconductor phase

Figure 4.11 shows experimentally extracted effective relative dielectric constant of the VO_2-loaded CPW lines during heating with the temperature ramping up from 22 to 60 ℃, which is below the transition temperature T_c =68 ℃. Comparing to the reference CPW lines, we can observe an obvious increase in both the real part and the imaginary part effective relative dielectric constant, which indicates an increase in the permittivity and the conductivity of the VO_2 thin-film when the temperature increases. At temperatures far below the transition temperatures, there is no sharp increase in the effective relative dielectric constant between different temperatures.

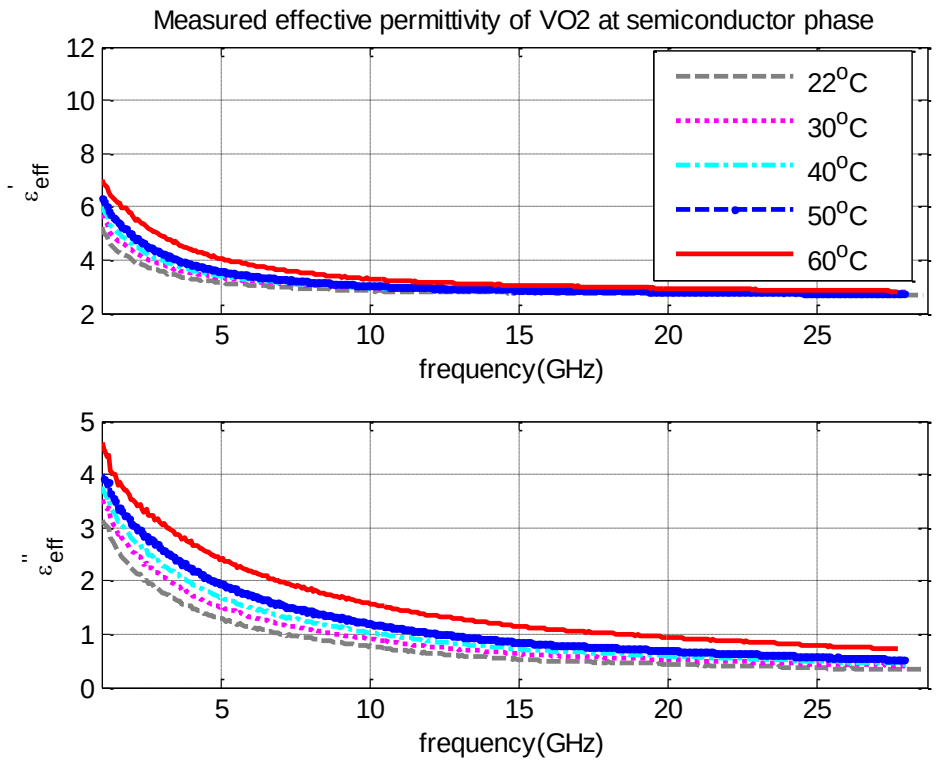

Figure 4.11: Experimental results of the effective relative dielectric constant of the VO_2-loaded CPW lines at varying temperatures below T_c.

After the effective relative dielectric constant of the VO_2-loaded CPW lines is obtained, we can follow the algorithm in section 4.3.4 to extract the relative dielectric constant and the conductivity of the VO_2 thin-film when temperature increases. As shown in Figure 4.11, we have three observations:

1) When temperature increases, both the relative dielectric constant and the conductivity of the VO_2 thin-film increase, the measurable frequency range is narrowed.

2) When frequency increases from 2GHz to 30GHz, the relative dielectric constant decreases from several hundred to around 80.

3) When frequency increases from 2GHz to 30GHz, the conductivity increases from around 30 to 100 (S/m).

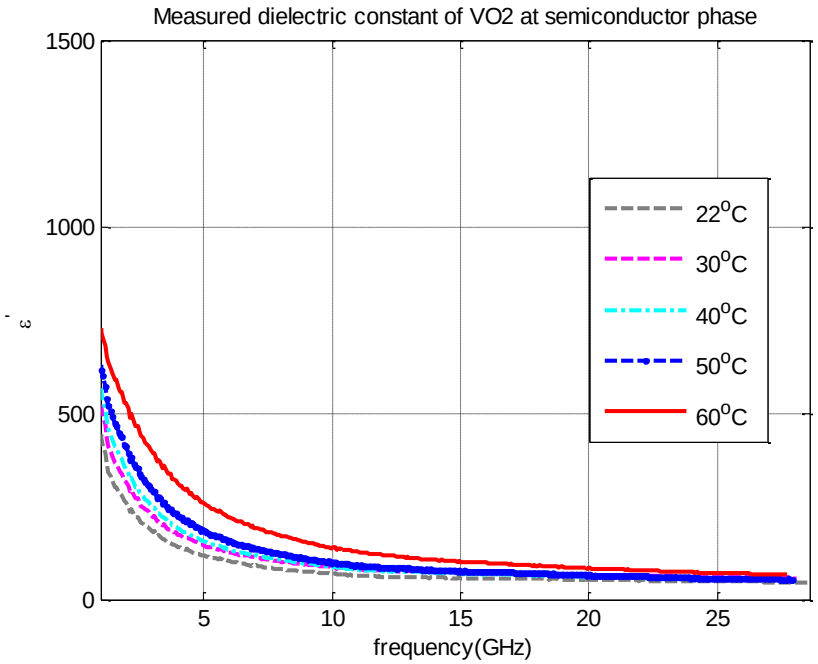

(a)

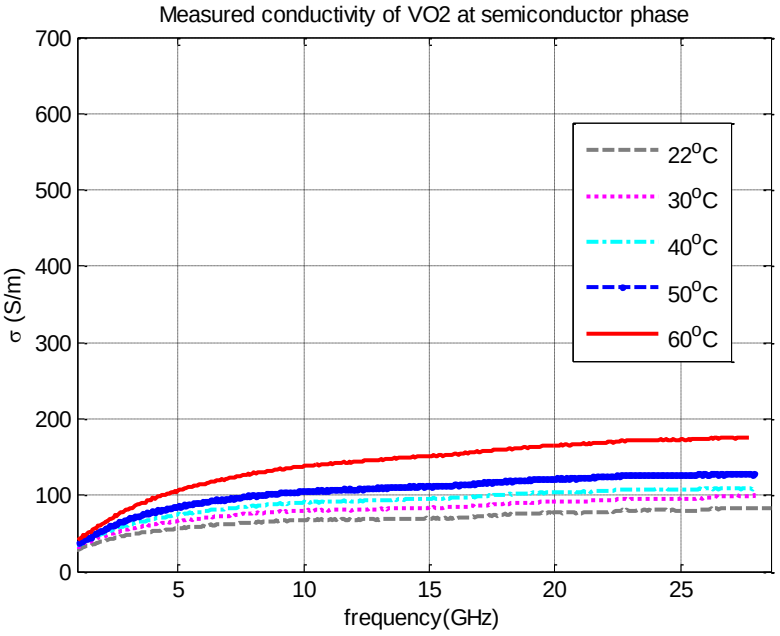

(b)

Figure 4.12: Experimental results for VO_2 thin-film at varying temperatures below T_c.

(a) Relative dielectric constant. (b) Conductivity.

2. Experimental results for VO_2 thin-film at metal phase

Figure 4.12 shows experimentally extracted effective relative dielectric constant of the VO_2-loaded CPW lines during heating with the temperature ramping up from 70 to 100 ℃. When the temperature increases over the transition temperature T_c=68 ℃, the VO_2 thin-film changes to metal phase. We can observe a sharp increase in both the real part and the imaginary part of the effective permittivity. The measurable frequency range is greatly narrowed. Comparing to the case when the temperature is well below T_c, we can observe a sharp increase in the effective relative dielectric constant, which indicates a sharp increase in the permittivity and the conductivity of the VO_2 thin-film when temperature increases. At temperatures above the transition temperatures, the effective relative dielectric constant increases continuously with temperature.

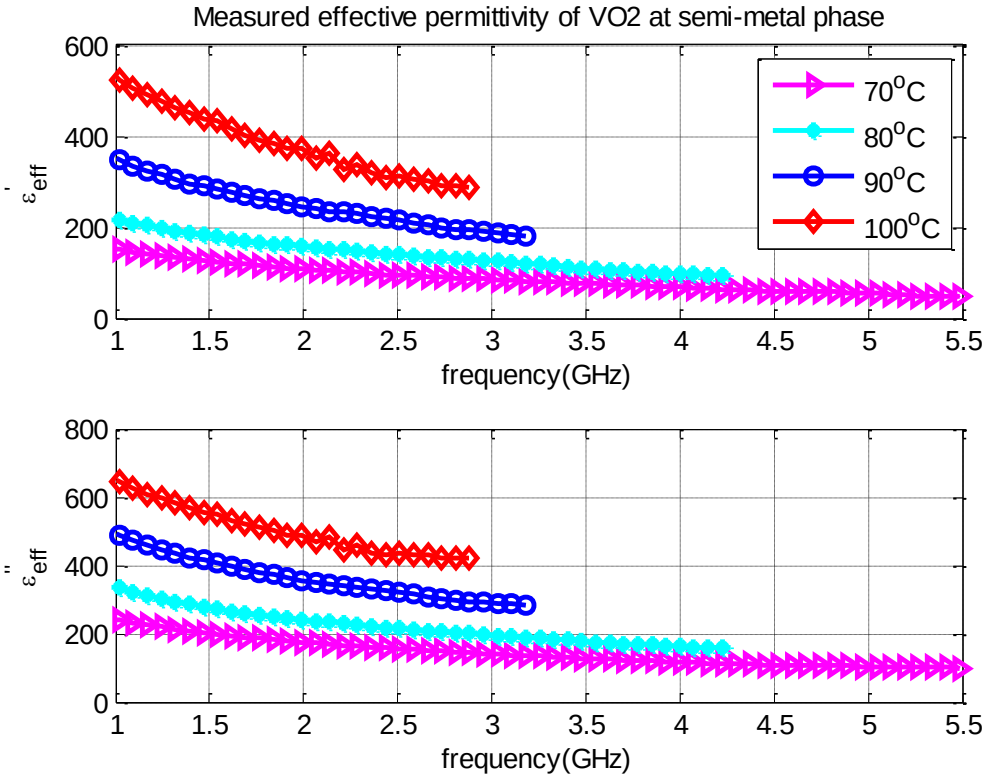

Figure 4.13: Experimental results for effective relative dielectric constant of the VO_2-loaded CPW lines at varying temperatures above T_c.

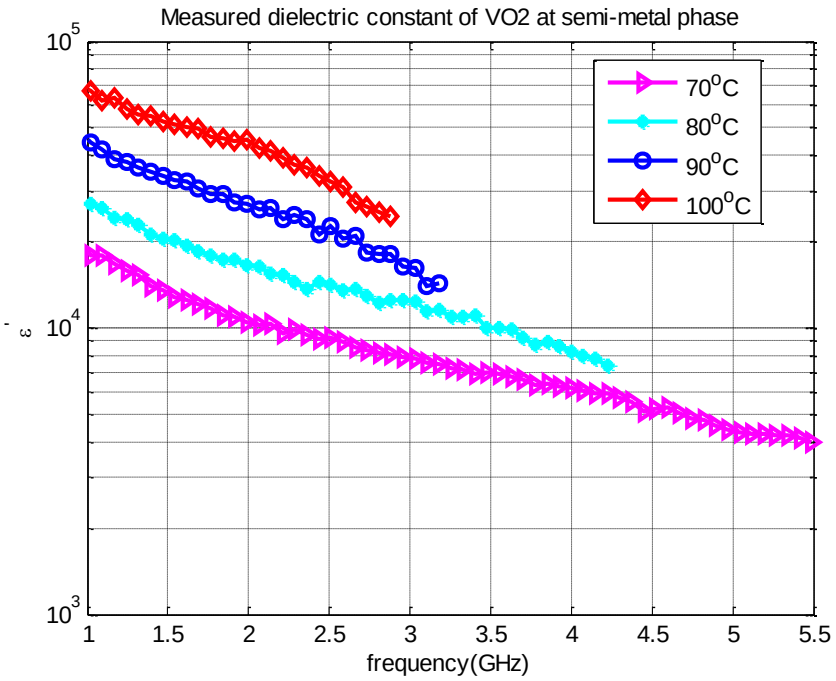

(a)

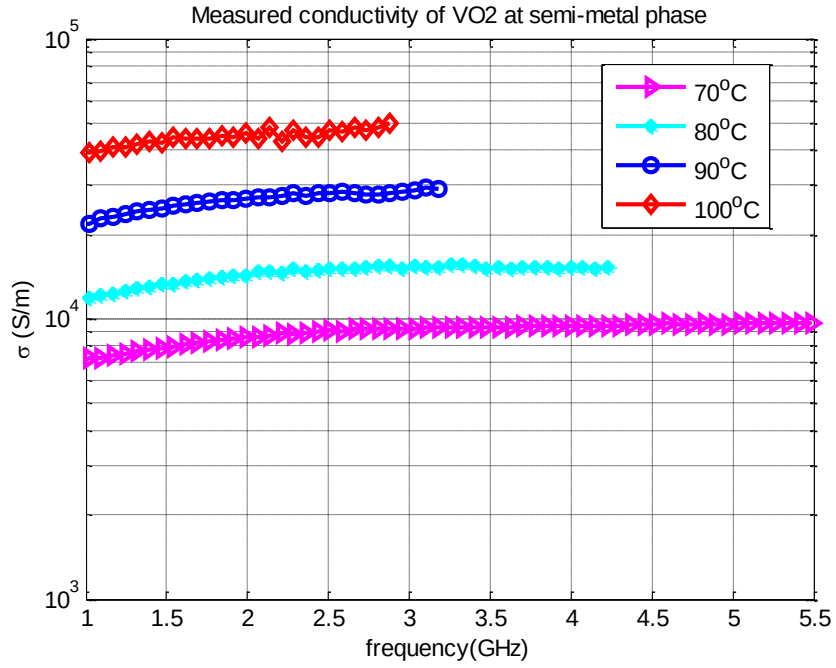

(b)

Figure 4.14: Experimental results. (a) Relative dielectric constant. (b) Conductivity.

After the effective relative dielectric constant of the VO_2-loaded CPW lines is obtained, we can follow the algorithm in section 4.3.5 to extract the relative dielectric constant and the conductivity of the VO_2 thin-film at metal phase. As shown in Figure 4.13, we have three observations:

1) When the temperature increases over the transition temperature, both the relative dielectric constant and the conductivity of the VO_2 thin-film increase. The relative dielectric constant and the conductivity of the VO_2 thin-film at 100 ℃ are around three times those at 22 ℃. The measurable frequency range is greatly narrowed as a result of the very high relative dielectric constant of the VO_2 thin-film above the transition temperatures.

2) When frequency increases from 1GHz to 5.5GHz, the relative dielectric constant of the VO_2 thin-film decreases, which maintains at a value in the order of 4.

3) When frequency increases from 1GHz to 5.5GHz, the conductivity of the VO_2 thin-film increases, which also maintains at a value in the order of 4.

4.3.7 Discussions on the measurement results

1) Measurable frequency range

As shown in Table 4-2, L_2 is designed as three times the length of L_1; L_4 is designed as three times the length of L_3. So the phase difference between the line pairs is equal to 90^o, which corresponds to one quarter wavelength at the maximum frequency.

Assume the designed length of the CPW is L, and then we can express the effective relative dielectric constant of the CPW lines by the maximum measurable frequency range and length L as

$$\sqrt{\varepsilon_r} = \frac{\lambda_0}{4L} = \frac{c}{4fL} \tag{4.15}$$

From equation (4.15), we know that the measurable frequency range is inversely proportional to the product of line length L and the square root of the effective relative dielectric constant of the CPW line. For the shortest line length L_3 and the frequency range up to 30GHz, we can plot the theoretical asymptote according to the equation (4.15).

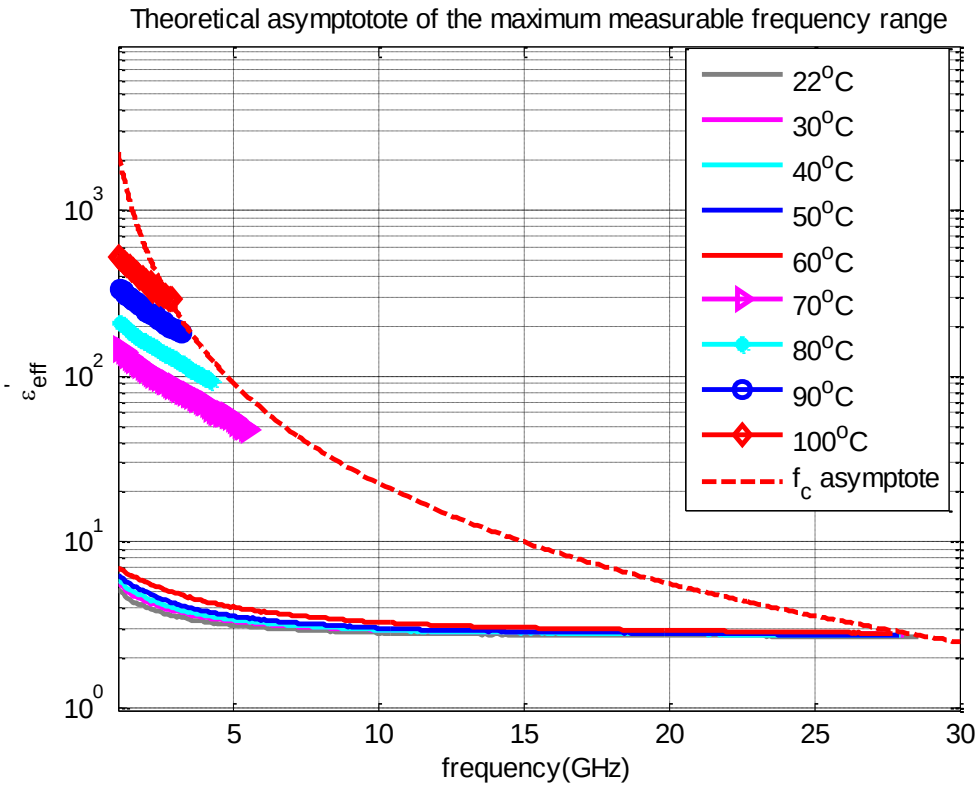

Figure 4.15: Theoretical asymptote of the maximum measurable frequency range.

As shown in Figure 4.15, the theoretical asymptote is very close to the maximum measurable Frequency at different temperatures. The higher the heating temperature is, the higher the effective relative dielectric constant of the CPW lines is and the narrower the maximum measurable frequency range becomes.

2) Comparison with the published measurement results

The temperature dependence of the relative dielectric constant and the conductivity of VO_2 thin-film at 2.5GHz are shown in Figure 4.15. The relative dielectric constant increases from ~53 at room temperature to $\sim 4.5 \times 10^4$ at 100 ℃. The conductivity increases from ~40 at room temperature to 4.6×10^4 at 100 ℃. Literature values for VO_2 thin-film are shown in Figure 4.15 for

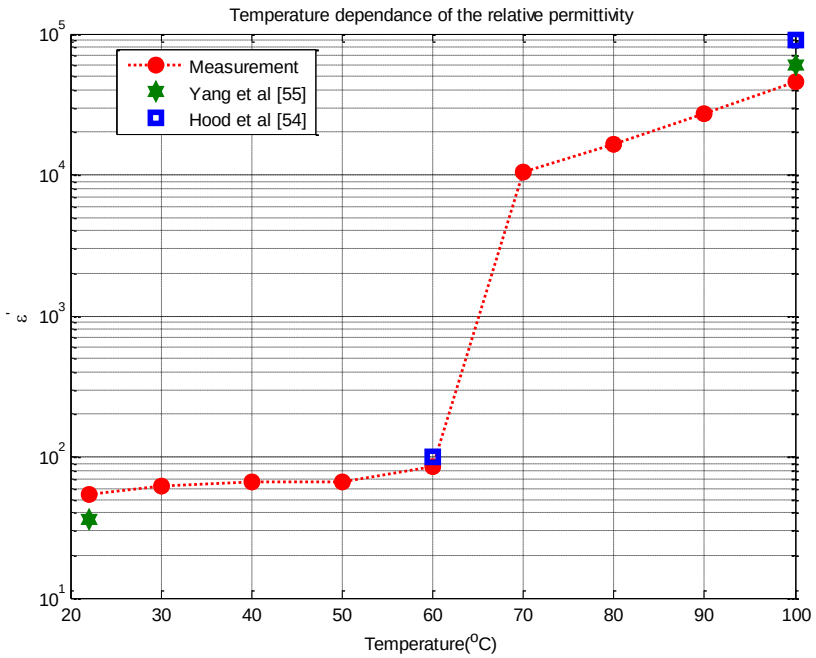

(a)

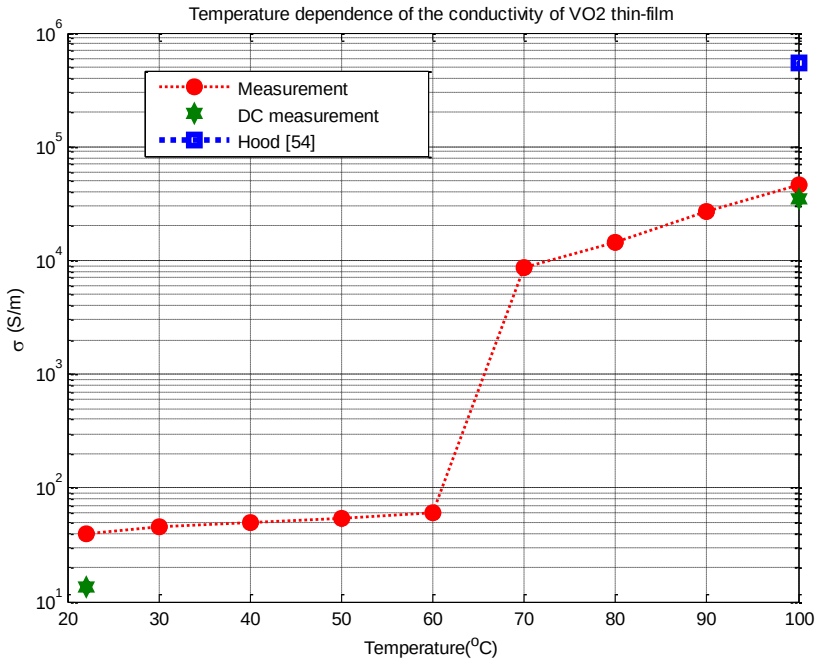

(b)

Figure 4.16: Comparisons with the literature values. (a) Relative dielectric constant. (b) Conductivity.

comparison purposes. The significant increase in both the relative dielectric constant and the conductivity arises from the thermally induced phase transition inside the VO_2 thin-film. The measured results are consistent with the reported results indicating the validity of the measurement methods used.

3) Dielectric mixture theory

According to literature [54], the temperature dependence of the measured dielectric constant indicates that the dielectric mixture phenomena occur inside the VO_2 thin films. To well explain the temperature dependent dielectric property of the VO_2 thin films, the Bruggement mixture theory is used to relate the volume fraction of the thin film in the conductivity state and the dielectric property of the conductive/insulating state to the dielectric property of the mixture. So the complex dielectric property of the mixture can be expressed as

$$\varepsilon = \varepsilon_2 + \varepsilon_1 \left[\frac{(1-\alpha)^2 \left[\frac{\varepsilon_2}{\varepsilon_1} - 1 \right]^2}{2} - \left[\frac{\varepsilon_2}{\varepsilon_1} - 1 \right] \sqrt{\frac{(1-\alpha)^4 \left[\frac{\varepsilon_2}{\varepsilon_1} - 1 \right]^2}{4} + (1-\alpha)^2 \left(\frac{\varepsilon_2}{\varepsilon_1} \right)} \right] \tag{4.16}$$

Where α is the volume fraction of the film in the conductive state, ε_1, ε_2 and ε are the complex dielectric constant of the insulating, conductive phases and the mixture, respectively.

We assume the real part of the relative dielectric constant of the insulating phase ε_1'=50, which is on the same order of the measurement results. The conductivity of the insulating phase σ_1 equals to 30(S/m) and the conductivity of the conductive phase σ_2 equals to 6×10^4(S/m). As the conductivity σ_2 of the conductive phase is much greater than the real part of the relative dielectric constant ε_2, we can choose the real part of the relative dielectric constant of the conductive phase ε_2'=ε_1'. The temperature-dependent relative dielectric constant and the conductivity of the mixture are shown in Figure 4.16 (a) and Figure 4.16 (b) respectively. The dominant features we can observe in Figure 4.16(a) are the strong resonance of ε' at a high volume fraction ($\approx 99\%$) of the conductive phase and the sensitivity of ε' at resonance to the conductivity of the insulating phase. As shown in Figure 4.16(b), we can also observe the insensitivity of σ of the mixture to the conductivity of the insulating phase.

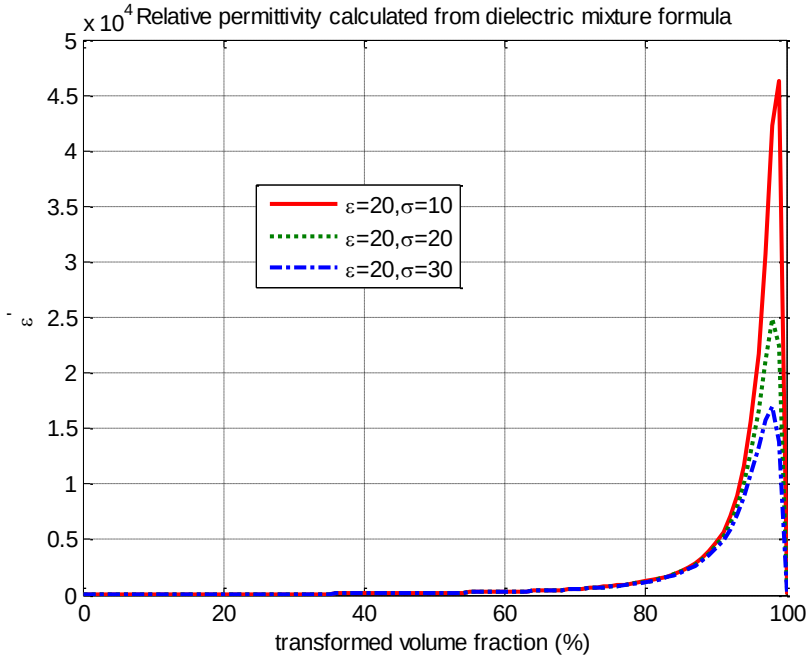

(a)

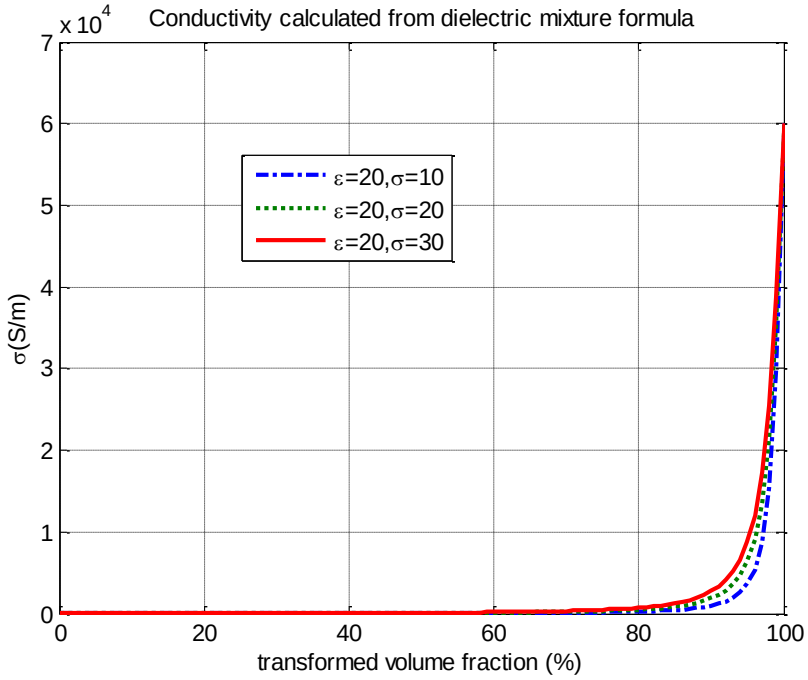

(b)

Figure 4.17: The dielectric property of the mixture. (a) Relative dielectric constant. (b) Conductivity.

4.4 Design of the thermo-tunable MIS coplanar slow-wave structures

From the analysis in section 3.6, there are three possible ways of designing a tunable MISCPW. As summarized in Table 4.5, if the transverse geometrical dimensions of the metallization can be reconfigured, we can realize a reconfigurable MISCPW. If we can control thickness b_1 using the bias voltage, we can design the voltage-dependent Schottky-contacted MISCPW. Another possible way of controlling the propagation velocity is by changing the conductivity and/or permittivity of the semiconductor layer.

Table 4.5: Three possible ways of designing tunable MIS coplanar SWS

Types	Mechanism	Parameter	Example
Type 1	Centre conductor	W	Reconfigurable MISCPW
	Gap	S	
Type 2	Insulation layer thickness	b_1	Schottky-contact MISCPW
Type 3	Conductivity and permittivity	σ_s, ε_{r2}	VO2-loaded MISCPW

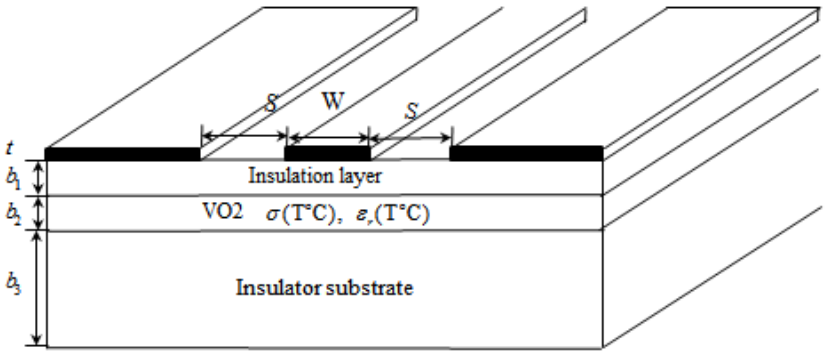

Figure 4.18: Illustration of the VO_2-loaded MISCPW.

Figure 4.18 is a simple illustration of the VO_2-loaded MISCPW. In this simple model, the semiconductor layer in the MIS structure is substituted by the VO_2 thin-film. If the temperature is varied, the permittivity and the conductivity of the VO_2 thin-film will change. In this way, the velocity of the wave propagation in MIS structure can be controlled. For a practical use of the MISCPW, instead of increasing only the Q factor, the slow-wave factor must be no less than the predefined value. It is also very important that the designed CPW fits the pitch size of the GSG probe available in our Poly-Grames Research Center. In section 4.3, we have fabricated and measured an MISCPW loaded with VO_2 thin film, the geometrical dimensions and the material parameters are listed in Table 4.6 (Line 1). The performance of this circuit will be used to compare with the new designed MISCPW here. The design objective is summarized as follows:

1) The slow-wave factor of the newly designed VO_2-loaded MISCPW must be comparable to that of Line 1. That is the slow-wave factor must be larger than 15 over the whole frequency range after phase transition.

2) The attenuation must be less than one half of that of Line 1.

Based on the analysis work done in section 3.6, we choose the following structural and material parameters shown in Table 4.6 (Line 2). Observed from Figure 3.25, the slow-wave factor over 15 can be achieved over the whole frequency range with the structural and the material parameters of Line 2.

Table 4.6: Structural and material parameters of the VO_2-loaded MISCPW

Dimension & permittivity	s	w	t	b_1	b_2	b_3	ε_{r1}
Line 1	40μm	340μm	1μm	0.1μm	0.6μm	530μm	4
Line 2	225μm	50μm	1μm	0.4μm	4μm	530μm	4

4.4.1 Frequency response of the thermo-tunable MISCPW

As discussed in Chapter 2, there are two frequencies limiting the propagation of the slow-wave inside the MIS structure. One is the dielectric relaxation frequency and the other is the frequency associated with the skin-effect mode. The dielectric relaxation frequency f_d which defines the boundary between the slow-wave mode and the lossy dielectric mode is expressed as

$$f_d = \frac{\sigma_s}{2\pi\varepsilon_0\varepsilon_s} \tag{4.17}$$

The characteristic frequency for skin-effect f_s is defined as

$$f_s = \frac{1}{\pi\mu_0\sigma b_2^{\,2}} \tag{4.18}$$

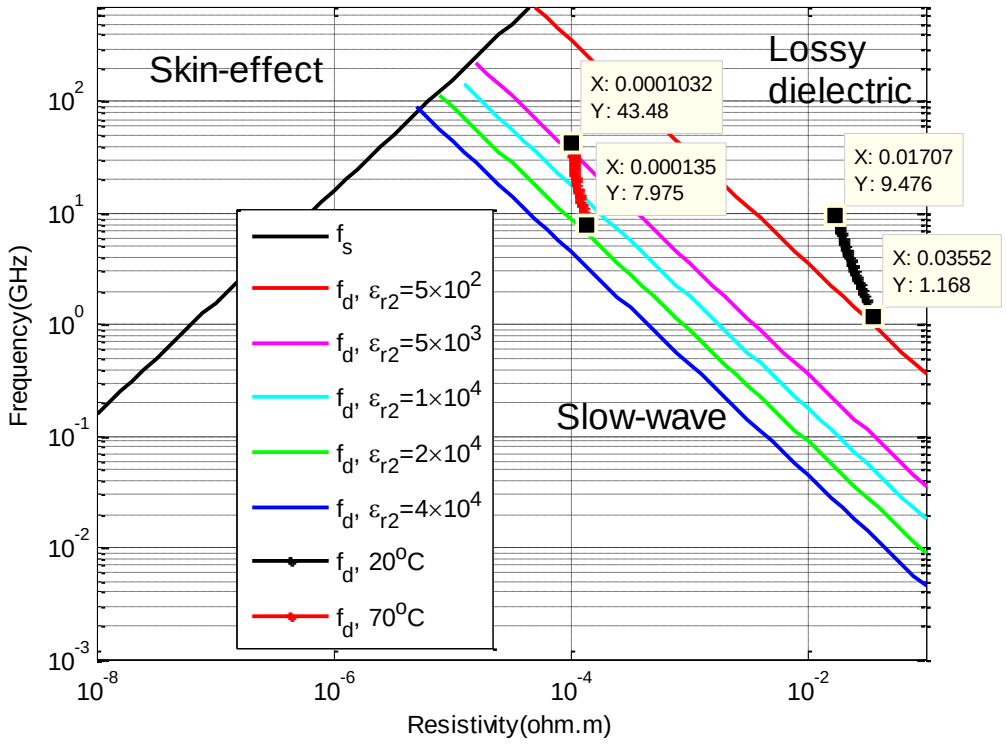

Figure 4.19: Resistivity-frequency domain chart for VO_2-loaded MISCPW at 22°C and 70°C.

As introduced in the beginning of this chapter, before the transition temperature T_c, the VO_2 thin film is at semiconducting phase with a very low conductivity value around 100(S/m). When temperature increases over T_c, the VO_2 thin film undergoes a sharp phase transition to metal phase whose conductivity increases by 3 orders. Taking the two limiting cases of 22°C and 70°C for example, as shown in Figure 4.19, at 22°C, the frequency limit f_d computed by equation (4.17) using the measured permittivity and conductivity of the VO_2 thin-film is 1.17GHz and 9.47GHz, which is very close to the operating frequency from 1GHz to 5.5GHz at 22°C. At 70°C, we can read from Figure 4.19 that the dielectric relaxation frequency f_d is 7.97GHz and 43.50GHz, which is much higher than the operating frequency. So the operating point at 70°C locates in the slow-wave region. Four curves of limiting relaxation frequency f_d corresponding to the permittivity from 5×10^2 to 4.0×10^4 are also plotted as the reference lines, which can help to identify the range of the permittivity value corresponding to 22°C and 70°C. In fact, it is much easier to confirm the existence of slow-wave from the field distribution.

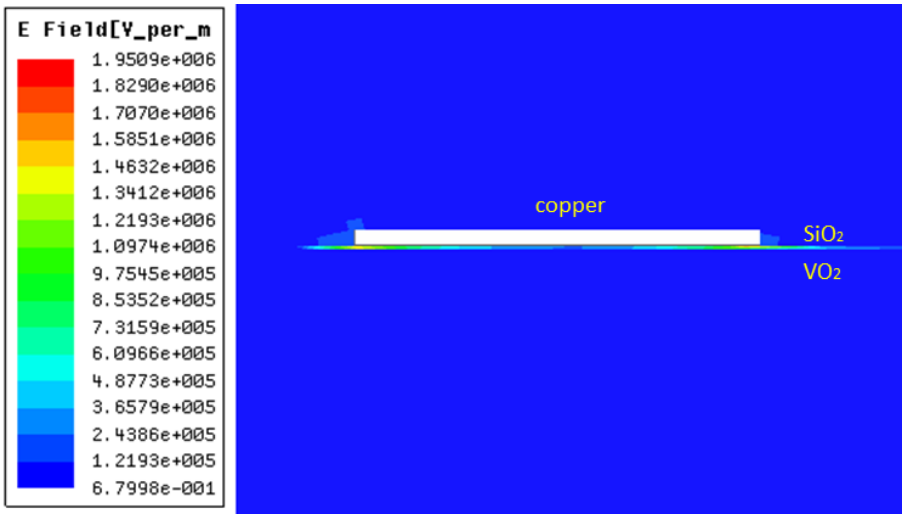

Figure 4.20: Electric field distribution for Line 2 at 22°C at 2.5GHz.

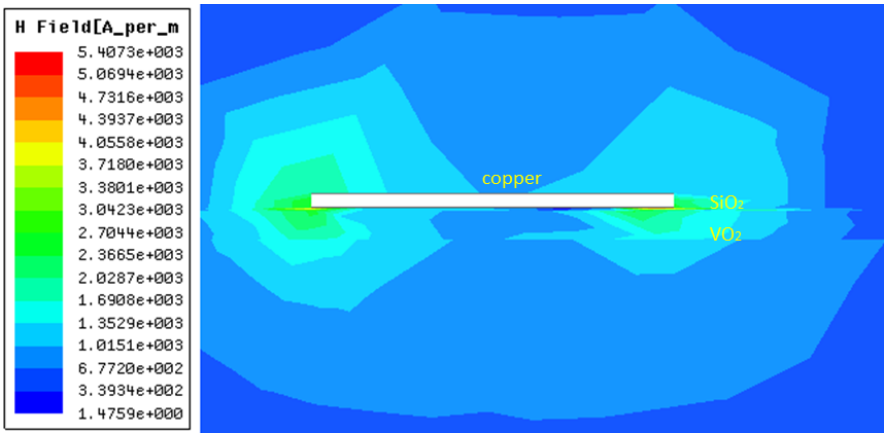

Figure 4.21: Magnetic field distribution for Line 2 at 22^{o}C at 2.5GHz.

It is observed from Figure 4.20 and Figure 4.21 that the electric field is confined inside the thin silicon dioxide layer. The magnetic field is similar to the case when no semiconductor layer exists. It suggests that a slow-wave is supported inside the VO_2-loaded MISCPW at 22^{o}C.

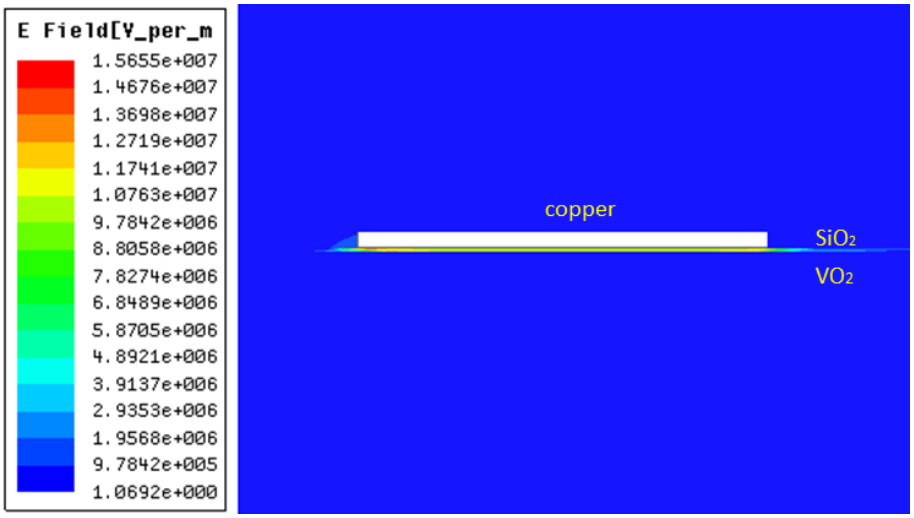

Figure 4.22: Electric field distribution for Line 2 at 70^{o}C at 2.5GHz.

It is seen from Figure 4.22 that the electric field is highly confined inside the thin silicon dioxide layer. The magnitude of the electric field is more than one order higher at 70^{o}C compared to the electric field distribution at 22^{o}C. The magnetic field in Figure 4.23 is also similar to the case

when no semiconductor layer exists. The above two graphs of field distribution also suggests the slow-wave propagation inside the VO_2-loaded MISCPW at 70°C.

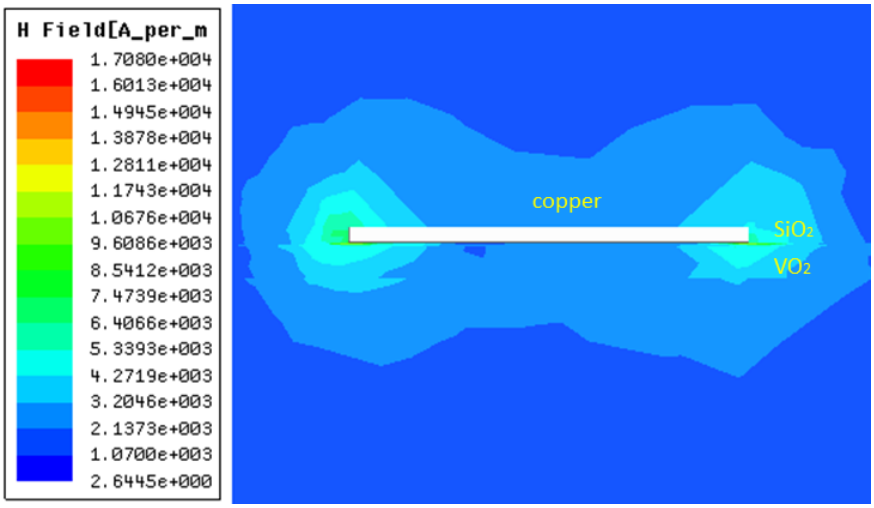

Figure 4.23: Magnetic field distribution for Line 2 at 70°C at 2.5GHz.

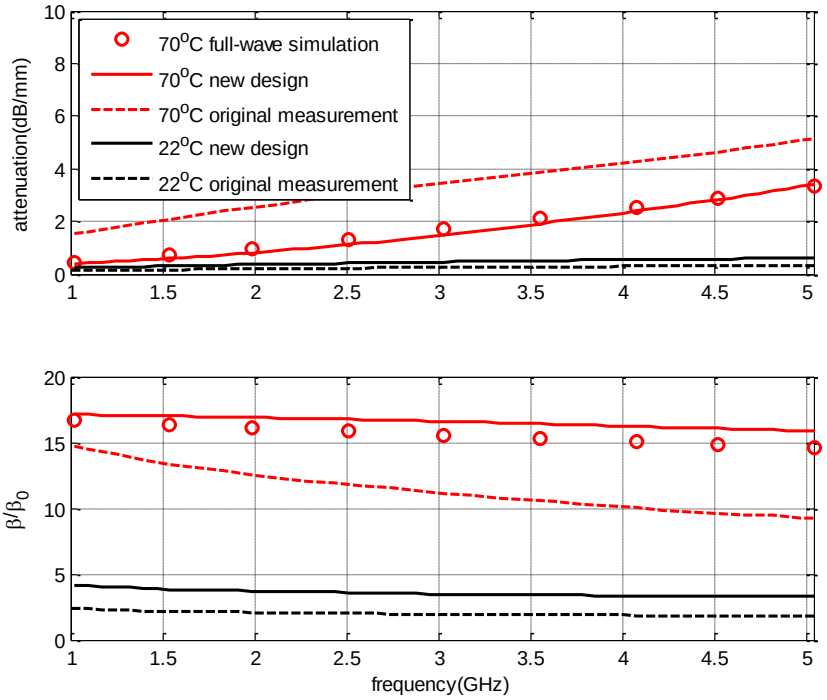

Figure 4.24: Attenuation and SWF of VO_2-loaded MISCPW at 22°C and 70°C.

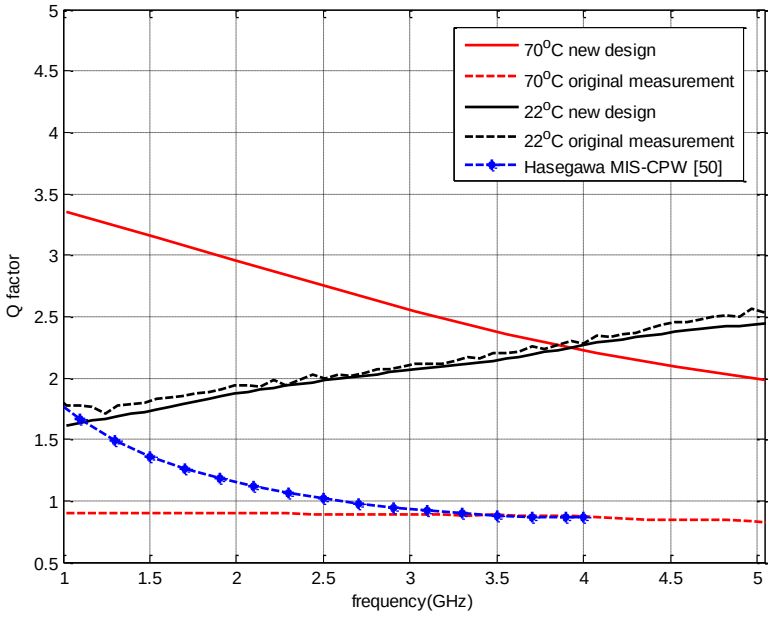

Figure 4.25: Q factor of VO_2-loaded MISCPW versus frequency at 22°C and 70°C.

The characteristics of the VO_2-loaded MISCPW are plotted against frequency in Figure 4.24 and Figure 4.25 from 1GHz to 5.5GHz at 22°C and 70°C respectively. The experimental results of Line 1 are also plotted for comparison purposes. Over the whole frequency range, the slow-wave factor is over 15 at 70°C. The attenuation is kept around 0.3dB/mm at 1GHz and below 3.3dB/mm at 5.5GHz. The performance of Line 2 is much better in attenuation, slow-wave factor and Q factor compared to Line 1. It is also seen that there is a big increase in slow-wave factor at 70°C compared to 22°C, but the attenuation increases to a less extent, which leads to an increase in Q factor. The Q factor of Line 2 is much higher than that experimented by Hasegawa [4].

4.4.2 Thermally-controlled VO_2-loaded MISCPW

To investigate the performance of the VO_2-loaded MISCPW versus temperature, the frequency limit f_d computed from the permittivity and conductivity of VO_2 thin film versus temperature at 2.5GHz is shown in Figure 4.26. It is observed that before the transition temperature, the maximum limiting frequency is 2.93GHz, which is higher but very close to the operating

frequency 2.5GHz. When temperature increases over T_c, the minimum limiting frequency corresponding to 70°C is 17.6GHz, which is much higher than the operating frequency. So the MISCPW works in the slow-wave region after the phase transition.

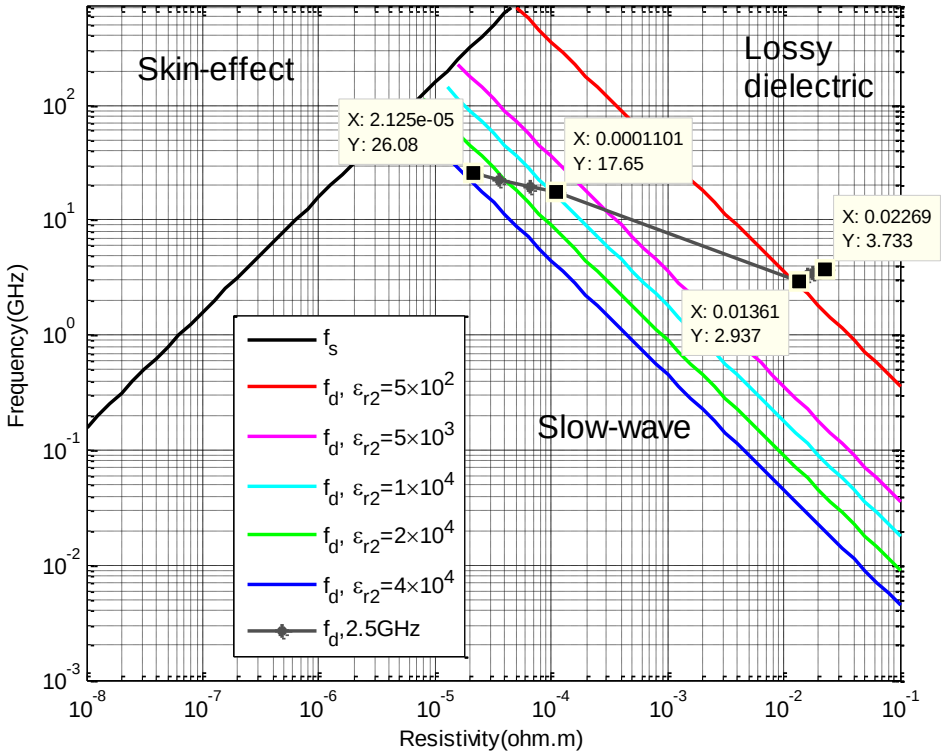

Figure 4.26: Resistivity-frequency domain chart for VO_2-loaded MISCPW versus temperature.

The performance of the VO_2-loaded MISCPW versus temperature is shown in Figure 4.27. It is seen that before the phase transition of the VO_2 thin film, the performance of Line 2 is comparable to that of Line 1. After the phase transition, there is an obvious increase in slow-wave factor and Q factor, the attenuation of Line 2 is maintained below 1.3dB/mm over the whole temperature range. It is observed that the slow-wave factor is comparable to that of the original measurement results and it is more than 15 after the phase transition. But the attenuation of Line 2 is greatly minimized which is only about one third of that of Line 1.

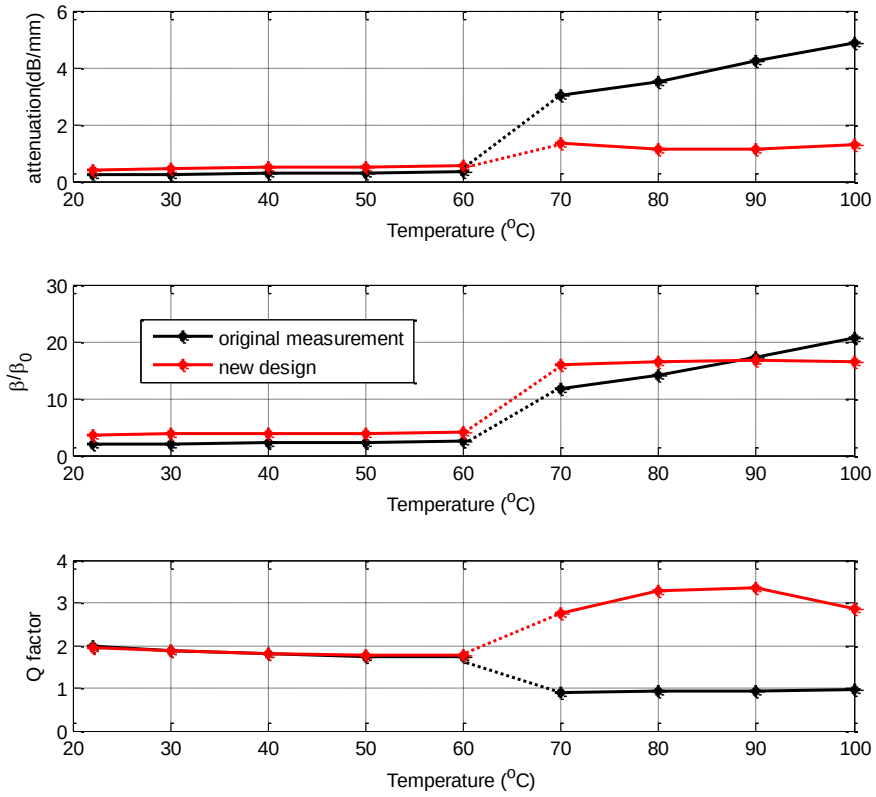

Figure 4.27: Performance of VO_2-loaded MISCPW versus temperatures at 2.5GHz.

CONCLUSION

The thermo-tunable MISCPW based on vanadium dioxide phase transition is presented and validated in this dissertation. As the conductivity and the permittivity of the VO_2 thin film change with temperature, we can observe a continuous tunability in attenuation, slow-wave factor and Q factors of the VO_2-loaded MISCPW, which is the key concept of designing the thermo-tunable MISCPW. When temperature increases over the transition temperature T_c, there is a dramatic increase in both conductivity and permittivity, which leads to a sharp difference in the performance of MISCPW before and after the phase transition. Combining the thermally tunable characteristics of the VO_2 thin film and the possible slow-wave propagation of the MIS structure, the VO_2-loaded MISCPW is very promising for the design of tunable delay lines, phase shifters and filters.

Before the final thermo-tunable MISCPW is demonstrated, three basic techniques are thoroughly discussed and analyzed. All of them make it possible to design and validate the thermo-tunable MIS coplanar slow wave structures:

1) Modeling techniques for MIS coplanar slow-wave structures

A new closed-form analytical model is proposed for the analysis of MIS-CSWS with acceptable accuracy. Compared with the approximate models in [28]–[35], the proposed model is capable of modeling both the thin-film and the thick-film MIS coplanar slow-wave structure. Comparisons with the state-of-the-art modeling techniques show the effectiveness of the proposed modeling technique. The proposed modeling techniques are very useful for the fast and accurate analysis of MIS coplanar slow-wave structures.

2) Broadband measurement of permittivity and conductivity of VO_2 thin-film

To better utilize VO_2 in RF-microwave tunable circuit design, complex dielectric constants of the VO_2 thin film are measured versus temperature. This is the first time that a broadband characterization of the VO_2 thin-film has been carried out.

For the measurement of relative dielectric constant of VO_2 at semiconductor phase, the multi-line method is used for the accurate extraction of the effective dielectric constant of VO_2-loaded CPW. The combination of a conformal mapping technique and a partial capacitance method are used to calculate the relative dielectric constant of the VO_2 thin film versus temperature before

phase transition. The measurement results from 2GHz to 30GHz agree very well with the full-wave simulation results and are consistent with the reported results, which indicate that this measurement method is very useful for the characterization of VO_2 thin-film before phase transition.

As for the measurement of the metal phase, an insulation layer of silicon dioxide is deposited between the CPW electrode and the VO_2 thin-film in order to avoid short circuit. The frequency range covers from 1GHz up to 5.5GHz for the metal phase. The multi-line method is used for the extraction of the effective relative dielectric constant of VO_2-loaded CPW. An optimization process combined with the full-wave Sonnet® Simulator is performed to extract the relative dielectric constant of the VO_2 thin film at metal phase.

3) Analysis and design of the thermo-tunable MIS coplanar slow-wave structure based on vanadium dioxide phase transition

A thermo-tunable MIS-CSWS based on vanadium dioxide phase transition is presented for the first time. It is also the first time that the vanadium dioxide thin film is used in the MIS structure substituting the semiconductor layer. The mechanism of tunability is totally different from that of schottky contact coplanar stripline described in [4].

Thermo-tunable MISCPW based on the MIS coplanar structure and the vanadium dioxide phase transition opens the way to the development of low-cost tunable microwave passive devices with a greatly reduced size. Future work on the applications of VO_2 thin-film is summarized below:

1) The thermo-tunable MISCPW introduced here is a preliminary research. As the SMT of the VO_2 thin-film can be induced by applied electric field, an electrically-tunable VO_2-loaded MISCPW could be realized. This should be much more interesting in the design of electrically-tunable microwave circuit.

2) As the conductivity change is very large before and after the VO_2 phase transition, the VO_2 thin-film can be used to realize the RF switch. This is very useful for the design of reconfigurable filters and frequency-selective surface with reconfigurable polarization.

3) An optimum MISCPW design is possible when the minimum slow-wave factor is achieved while at the same time improving the Q factor.

REFERENCE

[1] K. Wu, “Slow wave structures,” in Wiley Encyclopedia of Electrical and Electronics Engineering. New York: Wiley, pp.366-381, 1999.

[2] H. Guckel, P. A. Brennan, and I. Palocz, “A parallel-plate waveguide approach to microminiaturized, planar transmission lines for integrated circuits,” IEEE Trans. Microw. Theory Techn., vol. 15, no. 8, pp. 468-476, Aug.1967.

[3] H. Hasegawa, M. Fumkawa, and H. Yanai, “Properties of microstrip line on Si-SiO2 system,” IEEE Trans. Microw. Theory Techn., vol. 19, pp. 869-881, Nov. 1971.

[4] H. Hasegawa and H. Okizaki, “M.I.S. and Schottky slow-wave coplanar stripline on GaAs substrates,” Electron. Lett., vol. 13, no. 22, pp. 663-664, 1977.

[5] S. Seki and H. Hasegawa, “Cross-tie-slow-wave coplanar-waveguide on semi-insulating GaAs substrate,” Electron. Lett., vol. 17, pp.940 -941, 1981

[6] T. S. D. Cheung and J. R. Long, “Shielded passive devices for silicon-based monolithic microwave and millimeter-wave integrated circuits,” IEEE J. Solid-State Circuits, vol. 41, no. 5, pp.1183 -1200 2006

[7] F. J. Morin, “Oxides Which Show a Metal-to-Insulator Transition at the Neel Temperature,” Physical Review Letters 3(1): 34-36, 1959.

[8] Cavalleri, A., et al., “Evidence for a structurally-driven insulator-to-metal transition in VO2: A view from the ultrafast timescale”, Physical Review B 70(16), 2004.

[9] Ruzmetov, D., G. Gopalakrishnan, “Electrical triggering of metal-insulator transition in nanoscale vanadium oxide junctions,” Journal of Applied Physics 106(8), 2009.

[10] Sieu D. Ha et al., “Electrical switching dynamics and broadband microwave characteristics of VO2 radio frequency devices,” Journal of Applied Physics 113(2), 2013.

[11] Ruzmetov, D., K. T. Zawilski, et al., “Infrared reflectance and photoemission spectroscopy studies across the phase transition boundary in thin film vanadium dioxide,” Journal of Physics-Condensed Matter 20(46), 2008.

[12] Seo, M., J. Kyoung, et al., “Active Terahertz Nanoantennas Based on VO_2 Phase Transition,” Nano Letters 10(6): 2064-2068, 2010.

[13] Givernaud, J., C. Champeaux, et al., “Tunable band stop filters based on metal-insulator transition in vanadium dioxide thin films,” 2008 IEEE MTT-S International Microwave Symposium Digest, Vols 1-4: 645-648, 2008.

[14] Bouyge, D., A. Crunteanu, et al., “Reconfigurable 4 Pole Bandstop Filter based on RF-MEMS-Ioaded Split Ring Resonators,” 2010 Ieee Mtt-S International Microwave Symposium Digest (Mtt): 588-591, 2010.

[15] Givernaud, J., A. Crunteanu, et al., “Microwave Power Limiting Devices Based on the Semiconductor-Metal Transition in Vanadium-Dioxide Thin Films,” Ieee Transactions on Microwave Theory and Techniques 58(9): 2352-2361, 2010.

[16] S. Vegesna, Y. Zhu, Y. Zhao, Z. Fan, A. Bernussi and M. Saed, “Reconfigurable terahertz frequency selective structures using vanadium oxide,” Microwave Symposium Digest (IMS), 2013 IEEE MTT–S Intl., pp. 1-3, 2013.

[17] K. Arash, “Metal-insulator-semiconductor (MIS) slow-wave structures,” Master Thesis, Mcgill University, pp. 47, 2006.

[18] C. P. Wen, “Coplanar waveguide: a surface strip transmission line suitable for nonreciprocal gyromagnetic device applications,” IEEE Trans. Microwave Theory Tech., vol. 17, pp. 1087-1088, 1969.

[19] Y. R. Kwon, V. M. Hietala, and K. S. Champlin, “Quasi-TEM analysis of ‘‘slow-wave’’ mode propagation on coplanar microstructure MIS transmission lines”, IEEE Trans. Microw. Theory Tech., MTT-35: 545–551, 1987.

[20] R. Sorrentino, G. Leuzzi and A. Silbermann, “Characteristics of metal-insulator-semiconductor coplanar waveguides for monolithic microwave circuits,” IEEE Trans. Microw. Theory Tech., vol. MTT-32, no. 4, pp.410-415, 1984.

[21] K. Wu and R. Vahldieck, “Hybrid-mode analysis of homogeneously and inhomogeneously doped low-loss slow-wave coplanar transmission lines,” IEEE Trans. Microw. Theory Tech., MTT-39: 1348–1360, 1991.

[22] Y. Fukuoka, Y. C. Shih and T. Itoh, “Analysis of slow-wave co-planar waveguide for monolithic integrated-circuits,” IEEE Trans. Microw. Theory Techn., vol. MTT-31, no. 7, pp.567 -573 1983.

[23] David M. Pozar, “Microwave Engineering”, Wiley, 1998, chapter 3.

[24] David M. Pozar, “Microwave Engineering”, Wiley, 1998, chapter 4.

[25] W. Heinrich, “Quasi-TEM description of MMIC coplanar lines including conductor-loss effects”, IEEE Trans. Microwave Theory Tech., vol. 41, pp.45-52, 1993.

[26] K. C. Gupta, R. Garg, and I J. Bahl, “Microstrip Lines and Slotlines”. Dedham, MA: Artech House, pp.261-275, 1979.

[27] C. P. Yuan and T. N. Trick, “A simple formula for the estimate of the capacitance of two-dimensional interconnects in VLSI circuits,” IEEE Electron Device Lett., vol. 3, pp. 391–393, Dec. 1982.

[28] V. Milanovic, M. Ozgur et al, “Characterization of broadband transmission for coplanar waveguides on CMOS silicon substrates,” IEEE Trans. Microw. Theory Tech., vol. 46, no. 5, pp.632 -640 1998.

[29] W. Hilberg, “From approximations to exact relations for characteristic impedances,” IEEE Trans. Microwave Theory Tech., vol. MTT-17, pp.259–265, May 1969.

[30] H. Y. Lee and T. Itoh, “Phenomenological loss equivalence method for planar quasi-TEM transmission lines with a thin normal conductor or superconductor,” IEEE Trans. Microw. Theory Tech., MTT-37: 1904–1909, 1989.

[31] J. S. Ko, B. K. Kim, K. Lee, “Simple modeling of coplanar waveguide on thick dielectric over lossy substrate,” IEEE Trans. Electron Devices, vol. 44, No. 5, pp. 856-861, May 1997.

[32] J. Lescot, et al, “Coplanar transmission lines on SOI technologies for RF applications: modeling and experiments,” in Proc. ESSDERC'98, 1998.

[33] L. Liu, F. Lin, P. S. Kooi, and M. S. Leong, “Characterization of Coplanar Waveguides on MCM-D Silicon Substrate,” Asia Pacific Microwave Conference (APMC 1999), December 1999.

[34] P. Wang and E. C. C. Kan, “High-speed interconnects with underlayer orthogonal metal grids,” IEEE Trans. Adv. Packag., vol. 27, no. 3, pp.497 -507, 2004.

[35] C. Seguinot, P. Kennis, P. Pribetich, J. F. Legier, “Analytical Model of the Schottky Contact Coplanar Line,” in Proc. 14th European Microwave Conf., pp. 160-165, 1984.

[36] Kim H T, et al, "Monoclinic and correlated metal phase in VO2 as evidence of the Mott transition: coherent phonon analysis," Physical Review Letters 97(26), 2006.

[37]. Kim, H. T., B. J. Kim, et al, "Switching of the Mott transition based on hole-driven MIT theory," Physica B-Condensed Matter 403(5-9): 1434-1436, 2008.

[38]. Dumas-Bouchiat, F., C. Champeaux, et al, "rf-microwave switches based on reversible semiconductor-metal transition of VO2 thin films synthesized by pulsed-laser deposition," Applied Physics Letters 91(22), 2007.

[39] Seo, M., J. Kyoung, et al, "Active Terahertz Nanoantennas Based on VO(2) Phase Transition," Nano Letters 10(6): 2064-2068, 2010.

[40] Givernaud, J., A. Crunteanu, et al, "Microwave Power Limiting Devices Based on the Semiconductor-Metal Transition in Vanadium-Dioxide Thin Films," IEEE Trans. Microw. Theory Tech. MTT-58: 2352-2361, 2010.

[41] Lee, M. J., Y. Park, et al, "Two series oxide resistors applicable to high speed and high density nonvolatile memory," Advanced Materials 19(22): 3919, 2007.

[42] Dmitry Ruzmetov, Shriram Ramanathan, "Thin Film Metal-Oxides: Fundamentals and Applications in Electronics and Energy," Springer, 2010, chapter 2.

[43] Muraoka, Y. and Z. Hiroi, "Metal-insulator transition of VO2 thin films grown on TiO2 (001) and (110) substrates,"Applied Physics Letters 80(4): 583-585, 2002.

[44] Ruzmetov, D., K. T. Zawilski, et al., "Structure-functional property relationships in rf-sputtered vanadium dioxide thin films," Journal of Applied Physics 102(11), 2007.

[45] Ramanathan, S., G. D. Wilk, et al., "Growth and characterization of ultrathin zirconia dielectrics grown by ultraviolet ozone oxidation," Applied Physics Letters 79(16): 2621-2623, 2001

[46] Burkhardt, W., T. Christmann, et al., "Tungsten and fluorine co-doping of VO2 films," Thin Solid Films 402(1-2): 226-231, 2002.

[47] J. Nag, R. F. Haglund Jr., "Synthesis of vanadium dioxide thin films and nanoparticles," Jounal of Physics: Condensed Matter 20, 264016, 2008.

[48] Becker, M. F., A. B. Buckman, et al., "Femtosecond laser excitation dynamics of the semiconductor-metal phase transition in VO2," Journal of Applied Physics 79(5): 2404-2408., 1996.

[49] Kim, H. T., B. G. Chae, et al., "Mechanism and observation of Mott transition in VO2-based two- and three-terminal devices," New Journal of Physics 6, 2004

[50] Cavalleri, A., T. Dekorsy, et al., "Evidence for a structurally-driven insulator-to-metal transition in VO2: A view from the ultrafast timescale," Physical Review B 70(16), 2004

[51] W. R. Roach and I. Balberg, "Optical induction and detection of fast phase transition in VO_2," Solid State Comm 9, 551, 1971.

[52] Rice, T. M., H. Launois, et al., "Comment on Vo2-Peierls or Mott-Hubbard-a View from Band Theory," Physical Review Letters 73(22): 3042-3042, 1994.

[53] Wentzcovitch, R. M., W. W. Schulz, et al., "VO2-Peierls or Mott-Hubbard -a View from Band Theory." Physical Review Letters 72(21): 3389-3392, 1994.

[54] Hood, P. J. and J. F. Denatale, "Millimeter-Wave Dielectric-Properties of Epitaxial Vanadium Dioxide Thin-Films," Journal of Applied Physics 70(1): 376-381, 1991.

[55] Yang, Z., C. H. Ko, et al., "Dielectric and carrier transport properties of vanadium dioxide thin films across the phase transition utilizing gated capacitor devices," Physical Review B 82(20), 2010.

[56] R. B. Marks, "A multiline method of network analyzer calibration," IEEE Trans. Microwave Theory Tech., vol. 39, pp.1205-1215, 1991.

[57] M. D. Janezic and J. A. Jargon, "Complex dielectric constant determination from propagation constant measurements," IEEE Microw. Guided Wave Lett., vol. 9, no. 2, pp. 76–78, Feb. 1999.

[58] Ouaddari, M., S. Delprat, et al., "Microwave characterization of ferroelectric thin-film materials," IEEE Trans. Microw. Theory Tech., vol. 53, no. 4, pp. 1390-1397, 2005.

[59] E. Carlsson and S. Gevorgian, "Conformal mapping of the field and charge distributions in multilayered substrate CPWs," IEEE Trans. Microw. Theory Tech., vol. 47, no. 8, pp. 1544-1553, Aug. 1999.

[60] Z. Wang, J. Liu and L, Liu, “Permittivity measurement of $Ba_{0.5}Sr_{0.5}TiO_3$ ferroelectric thin films on multilayered silicon substrates,” IEEE Trans. Instrum. Meas., vol. 55, no. 1, pp. 350-356, 2006.

[61] H. A. Wheeler, “Formulas for the skin effect,” Proc. IRE, vol. 30, pp.412–424, 1942.